Construction and characterisation of ultra-thin alkali-metal vapour cells

WHITTAKER, KATE,AVRIL

Construction and characterisation of ultra-thin alkali-metal vapour cells

Kate Avril Whittaker

A thesis submitted in partial fulfilment
of the requirements for the degree of
Doctor of Philosophy

Department of Physics
Durham University

May 10, 2017

Abstract

This thesis presents the study of thermal alkali-metal vapours confined in a layer with a sub-micron thickness. This confinement enables the study of high density media without the loss of signal present in usually thermal vapours, but also has additional effects on spectra acquired from the system. Such effects include the suppression of the Doppler broadening and the interaction of the atoms with nearby surfaces. Herein, we present a study of this atom-surface interaction in both Rubidium and Caesium atoms, demonstrating that the interaction follows a power law of $1/r^{\alpha}$, where $\alpha = 3.02 \pm 0.06$.

We also study Rabi oscillations at high densities, driving GHz Rabi oscillations in a Rb vapour at densities up to 10^{17} cm^{-3}. We find that the results do not have sufficient agreement with an optical Bloch simulation, but Maxwell Bloch simulations indicate the possible presence of simultons; simultaneously propagating solitons. Such phenomena have not yet been observed out of crystalline media.

We also present a study of causality relations in atomic media. We first discuss the equivalency of the Hilbert transform to the Kramers-Kronig relations, well known in signal processing, but rarely applied in atomic physics. We then demonstrate that the Hilbert transform can be applied to atomic transmission spectra to quickly generate refractive index spectra.

The final section of this thesis fully details the successful design and fabrication of vapour cells with a thickness of 500-1500 nm. The cells are assembled using a combination of traditional scientific glass blowing techniques and thermally annealed optically contacted plates. We fully outline the production process, and then present evidence of their successful functionality and longevity.

Declaration

I confirm that no part of the material offered has previously been submitted by myself for a degree in this or any other University. Where material has been generated through joint work, the work of others has been indicated.

Kate Avril Whittaker
Durham, May 10, 2017

Acknowledgements

There are so many people I need to thank for helping my throughout my work in Durham. First, Charles Adams- whose excitement and passion for physics makes working with him inspiring and stimulating. Secondly, Ifan Hughes, who provided valuable insight and analysis on the experiments, and who made our weekly meetings so much fun. I particularly want to thank the final member of my supervisory team, my postdoc James Keaveney. He worked tirelessly to help me and was always on hand to provide guidance and assistance, I certainly wouldn't have completed this Ph.D. without his excellent teaching (and for proofreading most of this thesis!). I also want to thank our collaborators abroad. David and Armen, who have produced the finest nanocells in the world. Also, in Germany, Vahid and Benny- Vahid provided the impetus for us to start creating our own nanocells, and Benny who taught me the skills needed to make the Durham nanocells a reality.

Next, there is Teodora 'Dorky' Ilieva- my closest friend in Durham, and a temporary member of the nanocell team, I'm going to miss our smoking breaks where we sit and talk about all the stupid stuff under the sun. Paul Huilliery, thank you so much for being a wonderful housemate and colleague, and for all the late night hardcore physics chats. Also Hannes Busche, who provided so much advice for my technical problems. I also want to thank John Helm, who introduced me to the fabulous Boulevard. There is also Will, my replacement on the nanocell team who also helped proofread this thesis- good luck forging the future of nanocells in Durham and beyond. AtMol has generally been a lovely group to work in, with all members happy to help and share their expertise, and I am proud to have worked with such a wonderful bunch.

Finally, my family, my mum and dad, Nick and Alicia- thanks for always encouraging me to be the best I can, and prividing me with the tool I need to succeed in life. Also, my sister Rose, my favourite person in the world who is always looking out for me. Thanks for being a cool guy. Also, Rachel, whose advice of "It doesn't have to be perfect, it just has to be DONE", will be forever ringing in my ears. Finally, I want to thank Spenco- my constant partner throughout all of this, thank you for suffering through tech support so you could move with me, and for all your love throughout the years.

List of Figures

Contents

Chapter 1

Introduction

1.1 Thermal vapours: uses and applications

There are many ways to study atomic media and find applications for them. Atomic and molecular physics is split into two thermal regimes- ultracold; studying atoms at temperatures close to absolute zero, and thermal; studying atoms at room temperature and above. Figure 1.1 demonstrates an overview of some of the fields studied in atomic media. Across the horizontal axis, the fields are sorted from purely theoretical study to applications. Vertically, the scale is sorted from ultra-cold atoms to thermal vapours. Each field specified on the diagram in black text is a hyper-link to relevant papers and studies. This thesis focuses on the study of thermal vapours, specifically confined in ultra-thin cells where the physical studies and applications start to intersect with those often studied in ultra-cold atoms. We first focus on the study of thermal vapours.

Thermal vapour research centers around the study of a gaseous atomic sample of an alkali-metal confined inside a glass container. Valuable insight into atomic properties can be gained from laser interrogation. A particular point of interest that we study in this thesis is high temperature vapours, where the atoms are so dense that the inter-atomic separation is shorter than the near field of the atoms in the ensemble. This effects alters the response of the vapour, often resulting in cooperative interactions. However, studies at high temperatures, exceeding 150°C are hampered in vapour cells with mm lengths in the direction of beam propagation. This is because the high temperatures result in an increased density and therefore a larger optical depth. When the cell is 'long', an

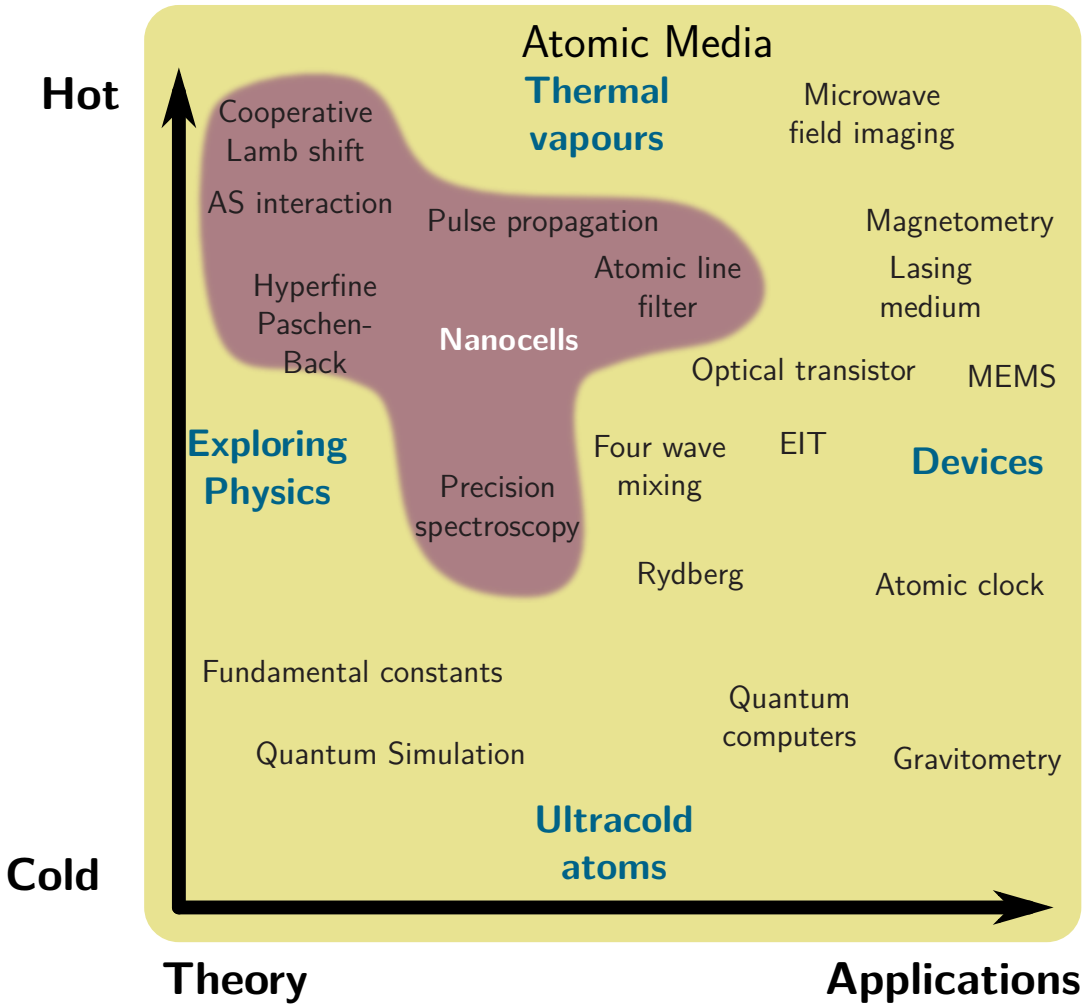

Figure 1.1: An overview of areas of research in atomic media. The x-axis sorts topics from purely theoretical to devices, and the y-axis sorts the topics from low to high temperature regimes, from ultracold (mK and below) to high temperature (above 300 K). Each topic is a hyperlink that leads to a relevant paper on the subject.

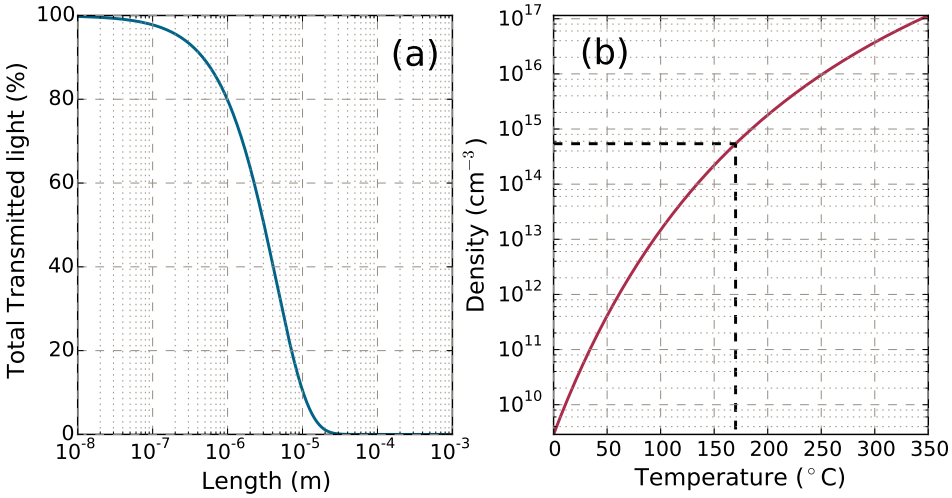

Figure 1.2: (a) Temperature dependence of percentage of light transmitted through a Cs vapour at 170°C interrogated with light tuned to the Cs $6S_{1/2}F_g = 4$ to $6P_{1/2}F_e = 4$ transition (b) Temperature dependent density of vapour inside the cell. Marked as a black line is the vapour temperature for panel (a).

interrogation beam is fully absorbed on atomic resonance meaning that studies must be done in the far detuned wings of the resonance. This is demonstrated on Fig. 1.2a- plotted is the percent of total light transmitted through a Cs vapour at 170°C interrogated with light tuned to the Cs $6S_{1/2}F_g = 4$ to $6P_{1/2}F_e = 4$ transition. It is clear that no light can be transmitted at length above 0.1 mm, demonstrating the use of shorter cells.

Optical density depends both on atomic density and path length in the direction of beam propagation. Hence, if the path length can be decreased, even larger ranges of density can be studied, the full range of densities available for study in this thesis are shown in Fig. 1.2b. The temperature used for the plot in panel (a) is plotted as a black dashed line.

Many alkali-vapour experiments require only a cell, a laser and some calibration optics, with such experiments yielding large amounts of data for analysis. Hence, much of vapour cell spectroscopy hinges on accurate modelling and fitting of atomic spectra. Thermal vapour physics has been an active field of study for the past 50 years, and so the theoretical basis for such systems is well established.

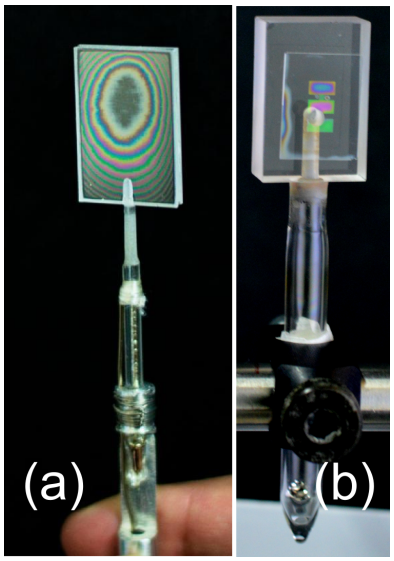

Figure 1.3: (a) Sapphire nanocell containing Cs produced in Armenia. Length ranges from 30-2000 nm. Photo courtesy of James Keaveney. (b) Three chambered quartz Rb nanocell produced in Durham, with chambers of length 1.5, 0.75 and 0.5 μm.

1.2 Nanometre scale cells

This thesis focusses on cells with a sub-micron length. All experimental work herein is performed in a cell with a length ranging from 30-2000 nm. The experimental results presented in this thesis are taken in cells produced by a group we are in collaboration with in Armenia pictured in Fig. 1.3a. The cells themselves are made of 2 Aluminium Oxide (sapphire) plates, with one plate ground to an extremely high radius of curvature that results in the aforementioned length range. The sapphire walls have an extremely high temperature resistance. The cell can be heated up to temperatures of 350°C, meaning that over seven orders of magnitude in atomic density can be studied, demonstrated on Fig. 1.2b.

Nanocells have an extremely short length in the direction of beam propagation, shorter than the mean free path of the atoms. This results in a suppression of the Doppler broadening usually observed in atomic spectra. The suppression can be so extreme that it is possible to resolve all hyperfine states even when the medium is excited with only a single beam. This means that high precision spectroscopy can be performed in the nanocell.

The study of vapours confined in such cells covers many areas, as illustrated as a pur-

ple area on Fig. 1.1. These areas exploiting the high density and therefore high group refractive index to produce superluminal pulse propagation inside the cell [1], and the experimental confirmation of the cooperative Lamb shift- and inter-atomic interaction that only occurs when atoms are in such close proximity that virtual photons mediating the electronic interactions between atoms are exchanged between two atoms in close proximity to each other, shifting the atomic transition [2].

Other studies in nanocells have focused on the study of the narrowing of spectral lines [3], including the 'collapse and revival' of the Dicke narrowing effect [4]; investigations of the hyperfine Paschen-Back regime in various alkali metals [5–7], extensive studies on the atom-surface interaction [8–11], EIT [12], and their use as atomic filters [13].

The atom-surface (AS) interaction is a particular focus in this thesis. It is the attractive interaction between laser induced dipoles in an atomic medium and their reflected image in a nearby surface. The interaction is observed as a red shift of spectral lines. The range of attraction is extremely short, acting over ranges of less than a few microns, and hence nanocells are an excellent medium to study this interaction. The studies thus far on the AS interaction in nanocells have utilised frequency modulated selective reflection spectroscopy to probe the medium [14], studying the reflected interrogation beams frequency dependent intensity profile to infer shifts in the medium. This necessarily probes the effect of only a single surface of the medium. Furthermore, the studies focus attention only on the shift of atomic peaks. In this thesis we intend to utilise fitting and scattered light from the medium to make an in depth study of the effect of the AS interaction and build an effective model that can fully describe its effect on atomic spectra.

This thesis also seeks to expand upon previous studies of high density pulse propagation. We drive GHz Rabi oscillations inside the cell in order to observe the effects of cooperative interactions upon pulse propagation. The results show a strong indication of the formation of simultons, simultaneously propagating solitons, which have never been previously observed outside of crystalline media.

1.3 Fabrication of alkali vapour cells

Although the cells produced at NAS in Yerevan, Armenia are of the highest quality available in the world, the ability to fabricate our own cells is also an extremely interesting

prospect. Fabrication of our own cells means full control over the production process and the ability to customise the cell interior for our own preferences. An example of one of the cells produced in Durham is shown in Fig. 1.3b. This will lead to the eventual ability to design and build cells for specific physical experiments such as including high numerical aperture lenses or other optical elements into cell windows.

By investing time into building specific cells with customised windows and interiors they can be inserted into a very simple set-up we are able to take advantage of the simplicity of vapour cell spectroscopy, gaining large amount of data for an in depth analysis.

Furthermore, all properties of the cell including materials, fabrication methods, surface quality, interior atmosphere and the atomic sample the cell is filled with. Most importantly, we can utilise new manufacturing methods to create cells with specific length ranges. The fabrication methods utilised in this thesis can also be further expanded to create custom interior geometries, such as capillary tubes or structures mimicking hollow-core fibres [15].

1.4 Structure of this thesis

This thesis will first discuss basic interactions occurring in thermal and ultra thin cells, before discussing specific experiments carried out before finally discussing the fabrication of nanocells.

- Chapter 2 discusses the theory of atomic spectra for mm and above length nanocells forming the basis of theory used in this work.
- Chapter 3 builds on the theories of chapter 2 and introduces new theories of interactions occurring in nanocells.
- Chapter 4 discusses causality, its use in spectroscopy and how to utilise the Hilbert transform to measure the full complex susceptibility of an atomic vapour.
- Chapter 5 presents experiments performed to probe the Atom-Surface (AS) interaction and the new experimental techniques used to probe it.
- Chapter 6 describes sub nanosecond length pulse propagation experiments inside the cell, probing the driving of population oscillations for a ‘Vee’ system.

- Chapter 7 covers the full cell fabrication process, outlining processes used and testing of the final product produced.
- Chapter 8 is an outlook of the work in this thesis, discussing possible directions the experiments could take and areas of future expansion in the area of cell fabrication.

1.5 Publications arising from this work

- K. A. Whittaker, J. Keaveney, I. G. Hughes, A. Sargsyan, D. Sarkisyan, and C. S. Adams, "Optical Response of Gas-Phase Atoms at Less than $\lambda/80$ from a Dielectric Surface", Phys. Rev. Lett. **112**, 253201, Published 26 June 2014
- K. A. Whittaker, J. Keaveney, I. G. Hughes, and C. S. Adams, "Hilbert transform: Applications to atomic spectra", Phys. Rev. A **91**, 032513, Published 25 March 2015
- K. A. Whittaker, J. Keaveney, I. G. Hughes, A. Sargsyan, D. Sarkisyan, and C. S. Adams, "Spectroscopic detection of atom-surface interactions in an atomic-vapor layer with nanoscale thickness", Phys. Rev. A **92**, 052706, Published 9 November 2015

Bibliography

[1] J. Keaveney, I. G. Hughes, A. Sargsyan, D. Sarkisyan, and C. S. Adams, Phys. Rev. Lett. **109**, 233001 (2012).

[2] J. Keaveney, A. Sargsyan, U. Krohn, I. G. Hughes, D. Sarkisyan, and C. S. Adams, Phys. Rev. Lett. **108**, 173601 (2012).

[3] S. Briaudeau, S. Saltiel, G. Nienhuis, D. Bloch, and M. Ducloy, Phys. Rev. A **57**, R3169 (1998).

[4] G. Dutier, A. Yarovitski, S. Saltiel, A. Papoyan, D. Sarkisyan, D. Bloch, and M. Ducloy, EPL **63**, 35 (2003).

[5] A. Sargsyan, R. Mirzoyan, and D. Sarkisyan, JETP Letters **96**, 303 (2012).

[6] A. Sargsyan, A. Tonoyan, G. Hakhumyan, C. Leroy, Y. Pashayan-Leroy, and D. Sarkisyan, Opt. Comm. **334**, 208 (2015).

[7] A. Sargsyan, B. Glushko, and D. Sarkisyan, J. Exp. Theor. Phys. **120**, 579 (2015).

[8] M. Chevrollier, D. Bloch, G. Rahmat, and M. Ducloy, Opt. Lett. **16**, 1879 (1991).

[9] M. Fichet, F. Schuller, D. Bloch, and M. Ducloy, Phys. Rev. A **51**, 1553 (1995).

[10] M. Fichet, G. Dutier, A. Yarovitsky, P. Todorov, I. Hamdi, I. Maurin, S. Saltiel, D. Sarkisyan, M.-P. Gorza, D. Bloch, et al., EPL **77**, 54001 (2007).

[11] H. Failache, S. Saltiel, M. Fichet, D. Bloch, and M. Ducloy, Phys. Rev. Lett. **83**, 5467 (1999).

[12] A. Sargsyan and D. Sarkisyan, Opt. Spec. **111**, 334 (2011).

[13] J. Keaveney, A. Sargsyan, D. Sarkisyan, A. Papoyan, and C. S. Adams, J. Phys. B **47**, 075002 (2014).

[14] M. Chevrollier, M. Fichet, M. Oria, G. Rahmat, D. Bloch, and M. Ducloy, J. Phys. II **2**, 631 (1992).

[15] R. Ritter, N. Gruhler, W. Pernice, H. Kübler, T. Pfau, and R. Löw, Appl. Phys. Lett. **107**, 041101 (2015).

Part I

Theory of thermal vapours

Chapter 2

Describing a 2 level atomic system

The majority of systems studied in this thesis are based on a two level alkali-metal vapour. The vapour is probed by an incident laser beam scanning in frequency close to the resonant frequency of a ground state transition. In this chapter we seek to form a description of the absorbative response of the vapour so that it can be used for computer fitting of experimental results.

This chapter starts from a description of a two level system with a ground and excited state using the time dependent Schrödinger equation, before using the results to calculate elements of the density matrix, used to describe time evolution of an atomic system. The matrix elements are then used to derive an expression for the atomic susceptibility, which can be used to calculate the absorption and transmission line-shapes for a laser beam incident through an atomic vapour. It then accounts for extra effects due to thermal motion and inter-atomic collisions, building a comprehensive model of line-shapes from a dilute atomic vapour.

2.1 System description

We consider our system to be a set of dipoles induced by an incident electric field. We model this as a simple 2-level system comprised of an atom with ground state $|g\rangle$ and an excited state $|e\rangle$, pictured in Fig. 2.1. We first describe pure states, where system observables have associated operators, that can ultimately be described by a set of eigenstates.

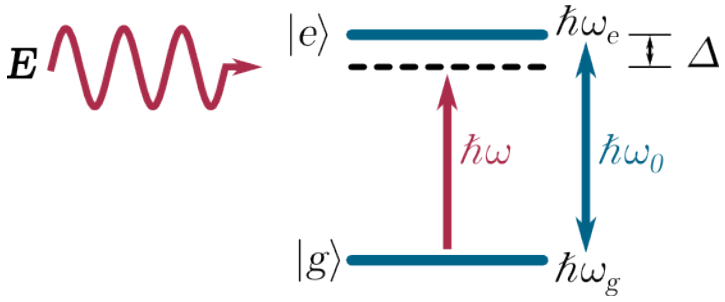

Figure 2.1: Energy level scheme of system described in this chapter. An incident electric field **E** of angular frequency ω and detuning $\Delta = \omega - \omega_0$ excites an atom from ground state $|g\rangle$ to excited state $|e\rangle$. The ground and excited states have energies $\hbar\omega_\mathrm{g}$ and $\hbar\omega_\mathrm{e}$ respectively

We can find these eigenstates using the time dependent Schrödinger equation, where the system evolution is described as:

$$i\hbar\frac{\partial\psi(\mathbf{r},t)}{\partial t} = \hat{\mathcal{H}}\psi(\mathbf{r},t), \tag{2.1}$$

where $\psi(\mathbf{r},t)$ is the atomic wavefunction, $\mathbf{r}$ is a position vector and $\hat{\mathcal{H}}$ is the Hamiltonian. The system we describe is a linear combination of multiple states. We define the atomic wavefunction $\psi(\mathbf{r},t)$, as:

$$\psi(\mathbf{r},t) = c_\mathrm{g}\langle\mathbf{r}|g\rangle\mathrm{e}^{-i\omega_\mathrm{g}t} + c_\mathrm{e}\langle\mathbf{r}|e\rangle\mathrm{e}^{-i\omega_\mathrm{e}t}, \tag{2.2}$$

where c_g and c_e are coupling coefficients for the ground and excited states respectively and the ground and excited states have energies $\hbar\omega_\mathrm{g}$ and $\hbar\omega_\mathrm{e}$ respectively. The resulting transition has resonant energy $\hbar(\omega_\mathrm{e} - \omega_\mathrm{g}) = \hbar\omega_0$

2.1.1 Building the Hamiltonian

We now seek an appropriate Hamiltonian $\hat{\mathcal{H}}$ for an atom with a ground and excited state driven by a time dependent laser field that induces dipoles in the medium, described as:

$$\hat{\mathcal{H}} = \hat{\mathcal{H}}_\mathrm{A} + \hat{\mathcal{H}}_\mathrm{I}, \tag{2.3}$$

where $\hat{\mathcal{H}}_\mathrm{A}$ is the atomic contribution and $\hat{\mathcal{H}}_\mathrm{I}$ describes the atom-light interaction. We set the energy of state $|g\rangle$ to zero, so $\hat{\mathcal{H}}_\mathrm{A}$ is simply:

$$\hat{\mathcal{H}}_\mathrm{A} = c_\mathrm{g}|g\rangle\langle g| + c_\mathrm{e}e^{-i\omega_0 t}|e\rangle\langle e|. \tag{2.4}$$

For the atom-light interaction, we must consider the atomic response to an oscillating field. The electric field of the laser induces dipoles aligned to the field polarization. Hence, we express it as:

$$\hat{\mathcal{H}}_{\mathrm{I}} = -\hat{\mu}.\mathbf{E}, \tag{2.5}$$

where $\hat{\mu}$ is the transition dipole operator, defined as $\hat{\mu} = e\hat{x}$, where $\hat{x}$ is the position operator. The dipole operator contains only off-diagonal elements, as the dipole operator is non-zero only for states of opposite parity [1].

We take a time dependent electric field of the form $\mathbf{E} = E_0\hat{e}\cos(\omega t) = E_0\hat{e}(e^{i\omega t}+e^{-i\omega t})/2$, where $\hat{e}$ describes the polarization of the field and E_0 is the electric field amplitude and ω is the laser angular frequency. We assume that the induced dipole is aligned to the field polarization, and hence we can express the off-diagonal matrix elements as:

$$\mathcal{H}_{\mathcal{I}} = -\mathbf{E}|g\rangle\langle e| - \mathbf{E}|e\rangle\langle g|. \tag{2.6}$$

We now collect pre-factors into a key parameter describing atom-light interactions, the Rabi frequency Ω, defined as

$$\Omega = -\frac{E_0 d_{\mathrm{ge}}}{\hbar}, \tag{2.7}$$

where $d_{\mathrm{ge}} = \hat{\mu}\cdot\hat{e}$. The Rabi frequency describes the strength of the coupling between the induced dipole and incident field, and clearly has a strong dependence on the incident laser intensity. For systems where the population is being transferred between states, the Rabi frequency describes the rate at which this population transfer takes place. This will be expanded on and further explored in chapter 6.

Hence we can now describe the full atomic Hamiltonian $\mathcal{H} = \mathcal{H}_{\mathrm{A}} + \mathcal{H}_{\mathrm{I}}$:

$$\mathcal{H} = c_{\mathrm{g}}e^{-i\omega_0 t}|g\rangle\langle g| + c_{\mathrm{e}}e^{-i\omega_e t}|e\rangle\langle e| - \frac{\Omega}{2}(e^{i\omega t}+e^{-i\omega t})|g\rangle\langle e| - \frac{\Omega}{2}(e^{i\omega t}+e^{-i\omega t})|e\rangle\langle g|. \tag{2.8}$$

2.1.2 Calculating coefficients

We can now substitute this back into the Schrödinger equation, and take the time derivative to seek solutions. We then study the resulting expression examining only the ground state, noting that dots above symbols denote a time derivative:

$$i\hbar\dot{c}_{\mathrm{g}}e^{-i\omega_{\mathrm{g}}t} = \frac{\hbar\Omega}{2}(e^{i\omega t}+e^{-i\omega t})c_{\mathrm{e}}e^{-i\omega_{\mathrm{e}}t}. \tag{2.9}$$

Gathering exponential terms, we find there are two terms that arise, $e^{-i(\omega+\omega_e)t}$ and $e^{-i(\omega-\omega_e)t}$. We discard the rapidly oscillating $e^{-i(\omega+\omega_e)}$ terms, as they will average away to zero over the time scales investigated. This exclusion is called the rotating wave approximation (RWA) [2] and is sufficient for most models of atomic systems. We then introduce the detuning $\Delta = \omega - \omega_0$.

Hence we can rearrange to find an expression for the time evolution of the ground state coefficient $\dot{c}_g$:

$$\dot{c}_g = -i\frac{\Omega}{2}c_e e^{i\Delta t}. \tag{2.10}$$

Similarly, we can gain an expression for the excited state coefficient:

$$\dot{c}_e = -i\frac{\Omega}{2}c_g e^{-i\Delta t}. \tag{2.11}$$

Using these two equations, we can build a description of the time evolution of the pure states in our system. However, we now move to a more convenient notation that simplifies calculations and can describe non pure states.

2.2 The density matrix

The Schrödinger formalism is excellent for describing the response of a medium that can be described by a set of pure eigenstates. However, it cannot describe mixed states or effects that are only described statistically, *e.g.* spontaneous emission. Hence we move to a new notation, the density matrix operator $\hat{\rho}$, defined as

$$\hat{\rho} = |\psi\rangle\langle\psi|, \tag{2.12}$$

which can be expanded to

$$\rho = \begin{pmatrix} c_g c_g^* & c_g c_e^* \\ c_e c_g^* & c_e c_e^* \end{pmatrix} = \begin{pmatrix} \rho_{gg} & \rho_{ge} \\ \rho_{eg} & \rho_{ee} \end{pmatrix}. \tag{2.13}$$

The diagonal terms of the density matrix ρ_{gg} and ρ_{ee} describe the probability of finding an atom in the ground and excited states respectively and are interpreted as level populations. The off-diagonal terms describe the interference between the states, or more explicitly, the coherences between the two states.

Random events such as spontaneous emission cannot be described as a pure state. They are instead a statistical mixture, requiring a sum over all states $|\psi_\mathrm{i}\rangle$ with probability of each state w_i. Hence we can generate an expression for a decay matrix $\hat{\Gamma}$:

$$\hat{\Gamma} = \sum_i w_\mathrm{i} |\psi_\mathrm{i}\rangle\langle\psi_\mathrm{i}|. \tag{2.14}$$

These cannot be represented in the Schrödinger equation, but can be easily included in the density matrix using basic matrix algebra, as will be discussed in the next subsection.

It is simple and intuitive to generate an expression for probability w_i for the state populations, density matrix elements ρ_{gg} and ρ_{ee}. If state $|e\rangle$ decays at a rate Γ, the population will reduce accordingly as the system evolves in time:

$$\dot{\rho}_{\mathrm{ee}} = -\Gamma\rho_{\mathrm{ee}}. \tag{2.15}$$

Conversely, state $|g\rangle$ will gain the population lost from $|e\rangle$:

$$\dot{\rho}_{\mathrm{gg}} = \Gamma\rho_{\mathrm{ee}}. \tag{2.16}$$

The effect on the coherences is more complex, a full derivation can be found in [3], and we simply quote the results here and include them in the final decay matrix:

$$\hat{\Gamma} = \begin{pmatrix} \Gamma\rho_{gg} & -\frac{\Gamma}{2}\rho_{ge} \\ -\frac{\Gamma}{2}\rho_{eg} & \Gamma\rho_{ee} \end{pmatrix}. \tag{2.17}$$

2.2.1 Time evolution

We can study the time evolution of the system by differentiating the density matrix with respect to time. If the interactions of the system are described with a Hamiltonian $\hat{\mathcal{H}}$, then the time dependence of the system is:

$$\dot{\rho} = \frac{i}{\hbar}[\hat{\rho}, \hat{\mathcal{H}}], \tag{2.18}$$

where the square brackets denote a commutative relation. This relation is known as the Liouville von Neumann relation and is commonly used to describe atomic systems.

The decay matrix can then be added to the Liouville equation to create a master equation describing the evolution of the atomic system with time [3]:

$$\dot{\rho} = \frac{i}{\hbar}[\hat{\rho}, \hat{\mathcal{H}}] - \hat{\Gamma}. \tag{2.19}$$

Using the master equation, we can now create a set of coupled rate equations describing the dynamics in the system. These equations are called the optical Bloch equations (OBEs), and are a powerful tool for atomic physicists. Using an appropriate Hamiltonian, they can readily be calculated for many systems for any number of atomic states. However, analytical solutions are only available for the simplest systems. The OBEs provide information about the time evolution of state populations and coherences, and can be used to describe the response of a medium to any excitation by altering the input Hamiltonian or decay matrices. However, here we will not derive the full set of OBEs, but merely solve for one element, ρ_{eg}.

The OBEs have two constraints. Firstly to conserve energy, the sum of populations must always be 1, *i.e.* $\rho_{\mathrm{gg}} + \rho_{\mathrm{ee}} = 1$. Secondly, the off-diagonal coherence terms are complex conjugates, $\rho_{\mathrm{eg}} = \rho^*_{\mathrm{ge}}$ [4].

Of particular interest is the solution for ρ_{eg}. This can be found by taking the time derivative of $\rho_{\mathrm{eg}} = c_{\mathrm{e}}c^*_{\mathrm{g}}$:

$$\dot{\rho}_{\mathrm{eg}} = c_{\mathrm{e}}\dot{c}^*_{\mathrm{g}} + \dot{c}_{\mathrm{e}}c^*_{\mathrm{g}}. \tag{2.20}$$

We can now substitute in equations 2.10 and 2.11, then express the result purely in terms of density matrix elements:

$$\dot{\rho}_{\mathrm{eg}} = i\frac{\Omega}{2}e^{-i\Delta t}(\rho_{\mathrm{ee}} - \rho_{\mathrm{gg}}). \tag{2.21}$$

Next, we make a further substitution of $\rho_{\mathrm{ij}} \rightarrow \tilde{\rho}_{\mathrm{ij}} = \rho_{\mathrm{ij}}e^{-i\Delta t}$, where i and j are atomic states. Examining the master equation, we see that dephasing due to spontaneous emission can simply be subtracted from the result, and so we get the following expression for $\dot{\tilde{\rho}}_{\mathrm{eg}}$:

$$\dot{\tilde{\rho}}_{\mathrm{eg}} = \frac{i\Omega}{2}(\rho_{\mathrm{ee}} - \rho_{\mathrm{gg}}) + \tilde{\rho}_{\mathrm{eg}}(i\Delta - \Gamma/2). \tag{2.22}$$

Expressions for all density matrix elements in the steady state can be found in a similar way. However, only $\dot{\tilde{\rho}}_{\mathrm{eg}}$ is discussed here as it can be used to derive an expression for the atomic electric susceptibility.

2.2.2 Steady state solution

Most systems studied in this thesis will be in a steady state, having no change with respect to time. The systems will also generally be within the weak probe limit [5], where the system is probed with an electric field that is sufficiently weak such that the medium is not significantly altered and negligible population transfer takes place. Steady state solutions for each density matrix element can be found by setting $\dot{\rho} = 0$. We also apply the weak probe limit, making $\rho_{gg} = 1$ and $\rho_{ee} = 0$. Hence, we can use Equation 2.22 to extract an expression for $\tilde{\rho}_{eg}$:

$$\tilde{\rho}_{eg} = -\frac{i\Omega}{2}\frac{1}{\Gamma_0/2 - i\Delta}, \tag{2.23}$$

where we have substituted Γ for Γ_0, the natural line-width of the transition being probed. Typical values for the natural line-width of alkali-metals are tens of MHz. Again, steady state results can be found for each element of the density matrix.

2.3 Relating the microscopic to the macroscopic

We now want to relate the OBEs to a measurable quantity. The microscopic interactions occurring in single atoms can be related to the macroscopic response of the entire medium using the complex electric susceptibility χ, which describes the magnitude of induced dipoles per unit field [6]. The complex susceptibility in the linear regime is defined as [7]:

$$\chi = \frac{\mathbf{P}}{\epsilon_0 \mathbf{E}}, \tag{2.24}$$

where ϵ_0 is the permittivity of free space, and $\mathbf{P}$ is the polarisation of the medium, calculated by summing the average dipole moment $\langle d \rangle$ per unit volume:

$$\mathbf{P} = \mathcal{N}\langle d \rangle, \tag{2.25}$$

where $\mathcal{N}$ is the number density of the vapour. The average dipole moment can be found the same way as any other expectation value of an operator, using $\langle d \rangle = \mathrm{Tr}(\hat{\rho}\hat{d})$.

It is worth noting that this definition of the polarization is limited to describing to a dilute gas where only linear interactions are taking place. For more complex systems where non-linear interactions are occurring, the result is modified slightly, adding higher

order terms of the electric field. For the case of atomic gases, this correction is of third order in the electric field [8].

Calculating the average dipole moment, and applying the RWA to the electric field, we find:

$$\chi = \frac{\mathcal{N} d_{\mathrm{ab}} \tilde{\rho}_{\mathrm{ba}} e^{-i\omega t}}{\frac{1}{2}\epsilon_0 E_0 e^{-i\omega t}}. \tag{2.26}$$

Substituting in equation 2.23, and expanding the Rabi frequency to its full form $\Omega = -d_{\mathrm{ab}} E_0/\hbar$, we find:

$$\chi = i\frac{\mathcal{N} d_{\mathrm{ab}}^2}{\epsilon_0 \hbar} \frac{1}{\Gamma_0/2 - i\Delta}. \tag{2.27}$$

For clarity, the complex electric susceptibility is sometimes expressed as:

$$\chi(\omega) = \chi_{\mathrm{R}} + i\chi_{\mathrm{I}}. \tag{2.28}$$

The real and imaginary components of the frequency dependent complex susceptibility are plotted in Fig. 2.2.

The imaginary component, χ_{I}, is plotted in blue and describes the absorbative response of the vapour near resonance. For a vapour of stationary atoms, where only the natural line-width describes the vapour response, the line-shape is a Lorentzian.

The real part of the complex susceptibility, χ_{R}, plotted in purple, describes the dispersive response of the vapour, from which the refractive index n and its associated properties can be derived. Both the real and imaginary components of $\chi(\Delta)$ will be discussed in the next subsections.

2.3.1 Frequency dependent refractive index

The real component of the complex susceptibility is related to the relative dielectric constant ϵ_{r}, calculated using $n = \sqrt{\epsilon_{\mathrm{r}}} = \sqrt{1+\chi}$.

The refractive index can be used to infer further vapour properties. Of particular interest is the group refractive index:

$$n_{\mathrm{g}}(\omega) = n_0 + \omega\frac{dn}{d\omega}. \tag{2.29}$$

This is related to the group velocity, governing the speed that a light pulse propagates through the vapour via $v_{\mathrm{g}} = c/n_{\mathrm{g}}$. Large positive n_{g} correspond to slowing, or even

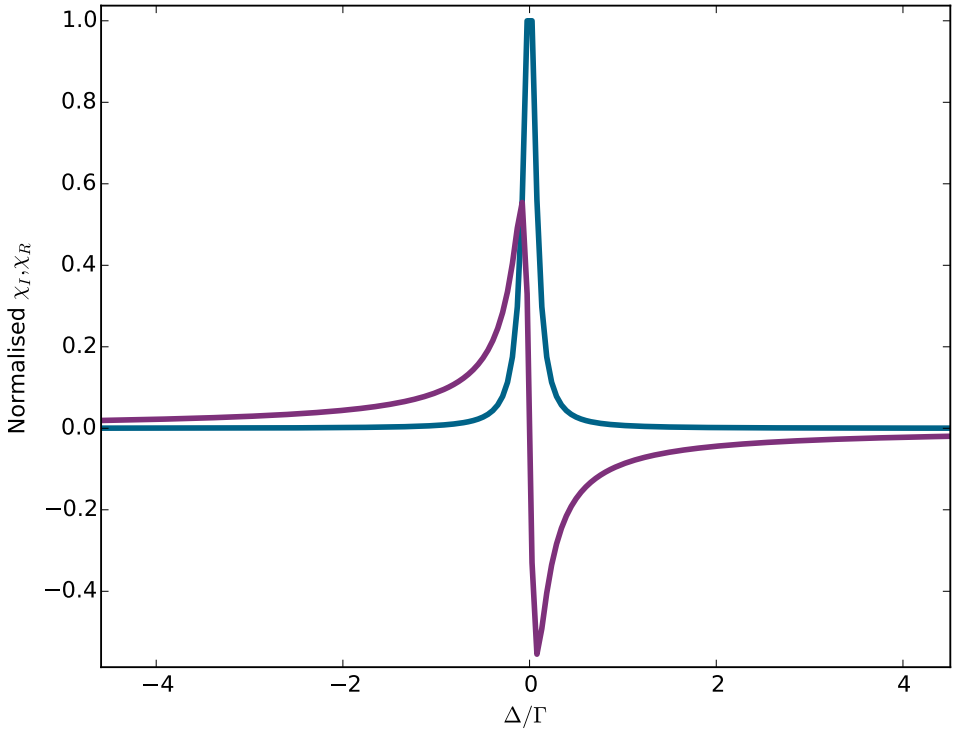

Figure 2.2: Real (purple line) and imaginary (blue line) components of the atomic susceptibility.

stopping, of a light pulse travelling through the medium [9]. Large negative values result in backwards propagation, also interpreted as superluminal propagation, where light pulses travelling through the medium arrive earlier than an off resonant pulse is expected to [10]. However, the final propagation speed does not exceed c, and it can be shown that causality remains intact [11].

2.3.2 Absorption and transmission line-shapes

A vapour excited by a laser with power P below the weak probe limit will absorb a proportional amount of the beam power dP per length dz propagated through:

$$dP = -P\alpha(\omega)dz, \tag{2.30}$$

where $\alpha(\omega)$ is the frequency dependent absorption, defined as $\alpha(\omega) = \chi_{\mathrm{I}}(\omega)k$. The relative absorbed beam power, dP/P can then be integrated over the limits of $z = 0$ to $z = L$,

where L is the cell length in the direction of beam propagation. To find an expression for relative absorbed beam power, the line-shape is normalised by dividing through by the incident power P_0, defined here as the change in transmission $\Delta\mathcal{T}$- a dimensionless quantity commonly measured when studying atomic spectra, given by:

$$\Delta\mathcal{T} = \frac{P}{P_0} = e^{-\alpha(\omega)L}. \tag{2.31}$$

Hence, the transmission line-shape can be calculated for the system. However, thermal motion and inter-atomic collisions broaden the line-shape and must be accounted for.

2.3.3 Doppler broadening

For a real atomic system, the atoms are in constant thermal motion with velocity $\mathbf{v}$. Motion will be in all directions, with velocities following a 1D Maxwellian velocity distribution:

$$W(v) = \frac{1}{u\sqrt{\pi}} e^{-\frac{|v|^2}{u^2}}, \tag{2.32}$$

where u is the most probably velocity of the atoms, with mass M, calculated using $u = \sqrt{2k_{\mathrm{B}}T/M}$, where k_{B} is the Boltzmann constant. Hence, the atoms are in constant motion relative to the incident laser wave vector $\mathbf{k}$. This results in a Doppler shift of the frequency observed by each atom, with atoms moving in the opposite direction to $\mathbf{k}$ observing lowerr frequencies, and atoms moving with the direction of $\mathbf{k}$ observing higher frequencies, with the shift described as $\Delta\omega = -\mathbf{k} \cdot \mathbf{v}$. However, we use beams with a $\mathbf{k}$ vector only in the z direction, and hence frequency shifts will only depend on the z component of the velocity vector, v_{z}. Hence, the Doppler shift can simply be expressed as $\Delta\omega = -k_0 v_{\mathrm{z}}$, where k_0 is the magnitude of the incident wave vector

The shift seen by each atom is not the same for all velocity classes, resulting in an inhomogeneous broadening with a Gaussian profile. The absorption from a Doppler profile is described as:

$$\alpha_{\mathrm{D}}(\Delta) = \exp\left[-\left(\frac{c\Delta}{\omega_0 u}\right)^2\right], \tag{2.33}$$

with a full width half maximum (FWHM) of

$$\delta_{\mathrm{D}} = \frac{\omega_0}{c}\sqrt{8k_{\mathrm{B}}T\ln(2)/M}. \tag{2.34}$$

This width is known as the Doppler width, typically on the order of a few hundred MHz for a room temperature alkali-metal vapour, which typically dominates over the much narrower natural line-width.

2.3.4 Self Broadening

The spectral line-shape is also changed by inter-atomic collisions. When an atom in the excited state undergoes a collision with another atom, there is a probability of the excited atom returning to the ground state. This results a reduction of the lifetime leading to a homogeneous broadening of the spectral lines that is linearly dependent on density $\mathcal{N}$ [12]. We model the collisional broadening Γ_{col} as

$$\Gamma_{\text{col}} = \beta\mathcal{N}, \tag{2.35}$$

where β is a proportionality constant, using values from [13]. The density is calculated from the measured temperature using the vapour pressure formulas in [14]. We assume we are within the collision regime where the binary approximation [2] is valid, meaning that the time of each collision event is shorter than the time between collision *i.e.* each atom undergoes only a single collision event before decaying. This is included in our line-shape model, replacing Γ_0 in Eq. 2.27 with Γ_{tot}, where $\Gamma_{\text{tot}} = \Gamma_0 + \Gamma_{\text{col}}$.

2.3.5 Voigt profile

Although absorption spectra are dominated by the Doppler profile, the Doppler profile alone does not fully describe absorption line-shapes. This is because each atom Doppler shifted to detuning kv_z still has an associated natural line-width that contributes to the line-shape at that point, demonstrated in Fig. 2.3. The figure shows a Doppler absorption profile as a grey area, with Lorentzian line-shapes at select detunings plotted as purple areas. The natural line-widths have been scaled to the Doppler profile for better visibility. The final line-shape is plotted as a solid red line. Fig. 2.3 demonstrates the need for a combination of the two line-shapes, as the contribution from the natural line-width must be summed over all Doppler detunings, resulting in a final line-shape that is neither fully Lorentzian or Gaussian.

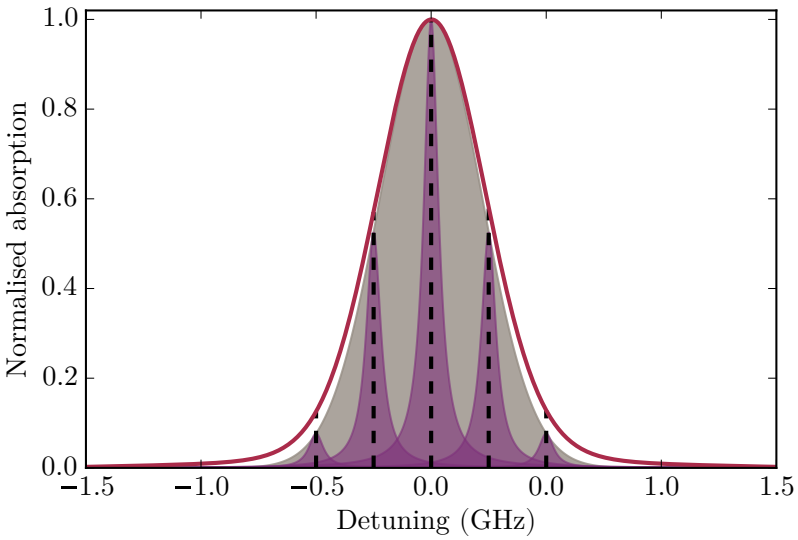

Figure 2.3: Demonstration of line-shape contributions from the Doppler effect (grey area) and the natural line-width. Atoms at each detuning, highlighted with a dotted black line have their own associated Lorentzian distributions (purple areas) arising from the natural line-width of the absorbing atom. The final resulting Voigt profile is plotted in red.

Mathematically, this final line-shape can be described using a convolution of the natural line-shape and the Doppler line-shape [15]:

$$I(\omega) = \int_{-\infty}^{\infty} \alpha(\omega)\alpha_D(\omega)\mathrm{d}\omega. \tag{2.36}$$

This is known as the Voigt profile, and is very commonly used to describe atomic line-shapes.

2.3.6 Generating theoretical line-shapes

The process of preparing a theoretical line-shape is shown in Fig. 2.4. To calculate multiple transitions, the model treats each transition as a closed 2 level system and calculates the line-shape for each individual transition. The resulting line-shapes are then summed all of them over the detuning range probed.

To fully describe and fit a standard single beam transmission line-shape in a standard vapour cell, with a length on the order of mm to cm, we sum over all hyperfine states on

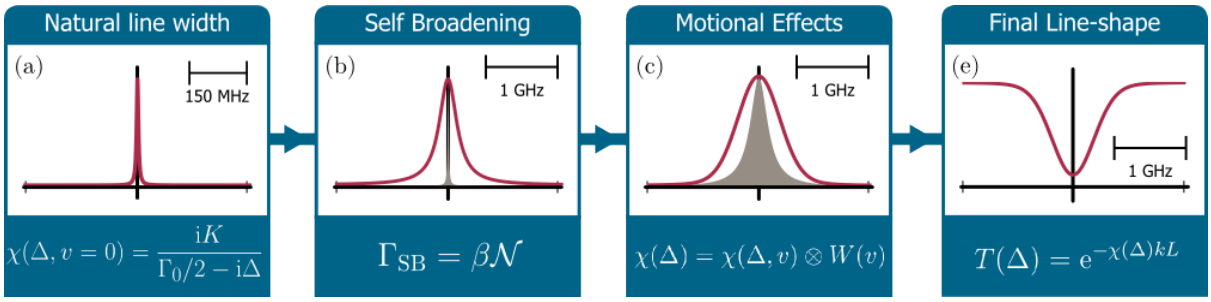

Figure 2.4: Construction of the theoretical line-shape used for fitting, accompanied by the most relevant equation describing each step. The previous step is plotted as a grey area to highlight changes to the spectrum.

transitions $|g\rangle \rightarrow |e\rangle$:

$$\chi(\Delta) = \sum_{e,g} i\frac{\mathcal{N}d_{ge}^2}{\epsilon_0\hbar}\frac{1}{\Gamma_{eff}/2 - i\Delta}. \tag{2.37}$$

Note that we include self broadening effects via the use of Γ_{eff}, effectively combining panels (a) and (b) on Fig. 2.4.

Note that for brevity, the pre-factor $\mathcal{N}d_{ge}^2/\epsilon_0\hbar$ is gathered into constant K on panel (a). The resultant line-shape is then convolved with a Doppler broadened line-shape $W(v)$ to produce a final self-broadened Voigt profile, as demonstrated in panel (c). Panel (d) shows that using Eq. 2.37, the absorption signal can be converted to a transmission signal for use in fitting of spectral lines.

Now there is a sufficient model, it can be applied to fitting spectra to determine more atomic properties. Fitting of spectra is a powerful tool employed throughout this thesis, used to determine the form of the atom-surface interaction, discussed in chapter 5, or to confirm functionality of newly fabricated cells, discussed in chapter 7. It is also routinely used to measure cell density when external temperature measurements are insufficient. Fitting has also been applied to determine fundamental constants such as k_B [16], to determine self broadening coefficients for alkali vapours [13], or to calculate dipole matrix element values for particular transitions [17].

ElecSus [14] is an excellent program for rapid and highly accurate fitting of alkali-metal spectra, developed in Durham. It is capable of fitting spectra from standard length vapour cells (from mm to cm length) and includes effects discussed herein, but furthermore calculates the impact of static external electric and magnetic fields that shift the transition frequencies via the Stark and Zeeman effects respectively [18].

This chapter has started from the time dependent Schrödinger equation, using it to describe the behaviour of atoms excited by an incident electric field. These results were then used to calculate elements of the density matrix, which can then be applied to gain an expression for the frequency dependent complex susceptibility. The imaginary component of the complex susceptibility can be used to calculate the absorption of a laser beam transmitted through an atomic medium, and so hence we have built a model of atomic absorption and transmission spectra.

However, this model is subject to limitations- it applies only to dilute vapours where only linear interactions are taking place. Furthermore, the cell length must be much longer than the excitation wavelength, typically covering cell lengths greater than 100 μm. This thesis is predominantly centred around the study of cells with lengths between 30-2000 nm, where this basic model is no longer sufficient. The next chapter will build on the model developed here, extending it to include extra effects such as atom-surface interactions that occur only when atoms are in such tight confinement.

Bibliography

[1] R. Loudon, *The Quantum Theory of Light* (OUP, Oxford, 2000), 3rd ed.

[2] C. Cohen-Tannoudji, J. Dupont-Roc, and G. Grynberg, *Atom-Photon Interactions: Basic Processes and Applications* (Wiley, Weinheim, 1998).

[3] H. Breuer and F. Petruccione, *The Theory of Open Quantum Systems* (OUP, Oxford, 2002).

[4] S. M. Barnett and P. M. Radmore, *Methods in Theoretical Quantum Optics* (OUP, Oxford, 1997).

[5] B. E. Sherlock and I. G. Hughes, Am. J. Phys. **77**, 111 (2009).

[6] C. S. Adams and I. G. Hughes, *Optics f2f* (OUP, to appear, Oxford, 2016).

[7] D. J. Griffiths, *Elementary Atomic Structure* (Pearson, San Francisco, 2008), 3rd ed.

[8] R. W. Boyd, *Nonlinear optics* (Academic press, Oxford, 2003), 3rd ed.

[9] M. Bajcsy, A. S. Zibrov, and M. D. Lukin, Nature **426**, 638 (2003).

[10] L. J. Wang, A. Kuzmich, and A. Dogariu, Nature **406**, 277 (2000).

[11] J. Keaveney, I. G. Hughes, A. Sargsyan, D. Sarkisyan, and C. S. Adams, Phys. Rev. Lett. **109**, 233001 (2012).

[12] B. H. Bransden and C. J. Joachain, *Physics of Atoms and Molecules* (Longman Scientific and Technical, Essex, 1990).

[13] L. Weller, R. J. Bettles, P. Siddons, C. S. Adams, and I. G. Hughes, J. Phys. B **44**, 195006 (2011).

[14] M. A. Zentile, J. Keaveney, L. Weller, D. J. Whiting, C. S. Adams, and I. G. Hughes, Comp. Phys. Comm. **189** (2015).

[15] W. Dermtröder, *Laser Spectroscopy: Basic Concepts and Instrumentation* (Springer, Heidelberg, 2003), 3rd ed.

[16] G. W. Truong, J. D. Anstie, E. F. May, T. M. Stace, and A. N. Luiten, Nat. Comm. **6** (2015).

[17] D. J. Whiting, J. Keaveney, C. S. Adams, and I. G. Hughes, Phys. Rev. A **93**, 043854 (2016).

[18] G. K. Woodgate, *Elementary Atomic Structure* (OUP, Oxford, 1980), 2nd ed.

Chapter 3

Describing atomic vapours confined in a nm scale layer

3.1 Nanometre scale vapour cells

Nanometre length vapour cells, called 'nanocells', have a nm scale length in the direction of beam propagation and can offer many interesting advantages for spectroscopy. A dominant feature of the cells is a greatly reduced optical depth, allowing very high densities to be reached. Signals at a similar density in mm-scale cells would be entirely lost to absorption in the medium. As nanocells are as compact as mm length vapour cells, they can be easily be placed in a heater to be cycled in temperature. Furthermore, the reduced optical depth means that very high temperatures can be reached without loss of signal in an very dense medium resulting in access to 7 orders of magnitude in density that spans several interaction regimes.

However, the extreme confinement also leads to other alterations to the measured absorption profile, which we will discuss in this chapter. We first discuss interactions that arise between atoms and virtual images formed in nearby surfaces. This interaction is typically extremely weak and will not have an impact on signals from larger cells. This length dependent interaction has an increasingly strong impact as cell lengths are shortened towards nanometre scales.

The atoms probed are also extremely physically confined. The length is much shorter

than the mean free path of the atoms, causing a suppression of the Doppler broadening. This effect is called Dicke narrowing, and can result in sharp well defined peaks from single beam spectroscopy, meaning higher precision experiments can be performed on much simpler experimental set-ups.

Finally, the interaction of electric fields inside the cell need to be considered. The cell walls are weakly reflecting meaning the cell acts as a low finesse etalon. Furthermore, back reflected signals are no longer negligible and should be considered in a final analysis.

All three of these effects will be discussed and incorporated into a final model of the frequency dependent absorption that is suitable to generate theoretical line-shapes for fitting of nanocell spectra. In this chapter, we seek a final model that should be sufficiently accurate that it can be used to extract information about a vapour, but simple enough to calculate such that it can be used in fitting with a Marquardt-Levenberg algorithm [1].

3.2 Additional effects on line shape

3.2.1 Atom-Surface interactions

Inside the nanocell, atoms are always in close proximity (less than one micron) to the cell walls. When a dipole is induced in the medium by an incident laser, it will have an interaction with the nearby surface, called the atom-surface (AS) interaction. The laser-induced dipole instigates a charge redistribution in the nearby surface, with each pole repelling like charges. This forms an image dipole with mirrored charges, displayed in Fig. 3.1a [2]. This virtual image can then interact with the real dipole. As the image charges are mirrored, the interaction between the real and image dipoles is attractive and hence the potential describing this interaction is negative. Over the length ranges available for our experimentation, we use the short range form of this potential to describe shifts inside the cell:

$$U_{\mathrm{vdW}} = -\left(\frac{C_3}{r^3} + \frac{C_3}{(L-r)^3}\right), \tag{3.1}$$

where C_3 is a coefficient describing the strength of the atom-surface coupling, L is the cell length and r is the atom-surface separation. This shift is negligible until AS separa-

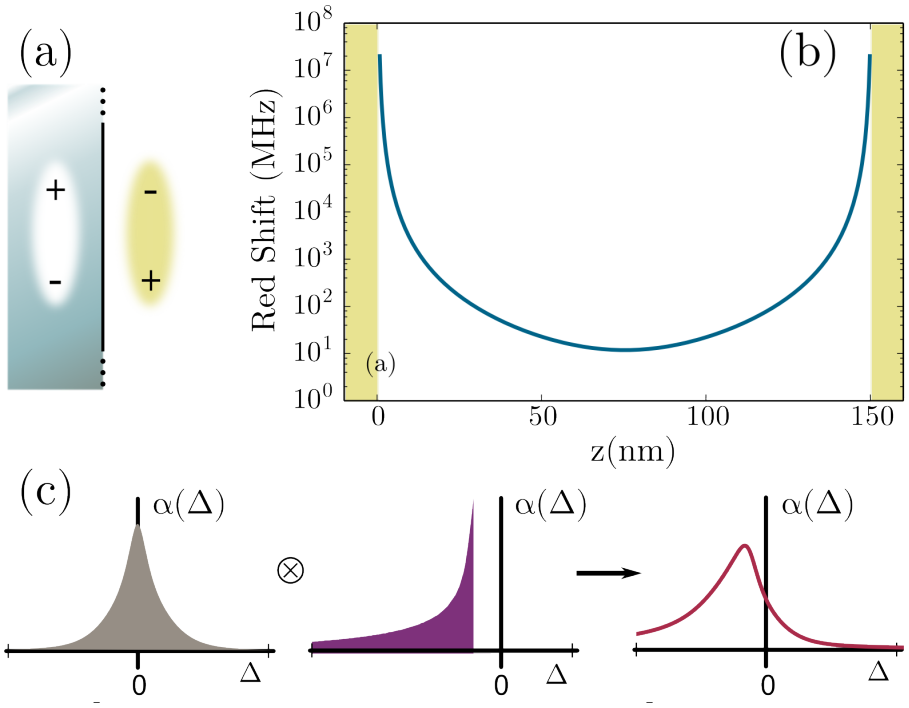

Figure 3.1: (a) Laser-induced dipole (yellow) forming an image dipole (white area) inside the cell surface. Note that the image dipole has mirrored charges. (b) Red shift experienced by atom at position x, where x is the distance from the first interior surface. Plotted for an $L = 150$ nm cell. (c) Convolution used to generate an AS shifted detuning dependent absorption line-shape ($\alpha(\Delta)$). Origin represents zero detuning (Δ) from the atomic transition frequency. The initial Dicke narrowed line-shape is plotted as a grey area. The effect of the AS shift is plotted as a purple area. The two functions are convolved to generate the final AS shifted absorption, plotted as a red line.

tions are less than 100 nm, where shifts are on the order of kHz, below the limit of our experimental resolution. The resultant shift from the potential is plotted in Fig. 3.1b for a cell of length 150 nm.

Chapter 5 will have a more in depth study of the AS interaction, and a more involved discussion of the theory and experiments performed can be found there. Here, we will simply discuss the impact of the line-shape and how it is included in fitting.

Because the AS potential is negative, atoms experiencing it will lose energy and therefore a red shift of the transition frequencies will be observed. However, atoms are distributed at random positions across the entire cell with each individual atom experiencing a different shift. Hence, the resultant spectral line is not a simple shift, but has a large asymmetric

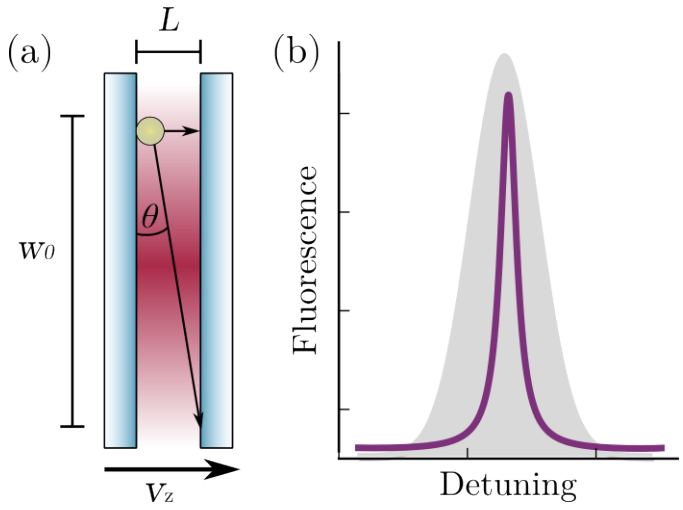

Figure 3.2: (a) Atomic trajectories inside the nanocell. Atoms with a small velocity in the direction of beam propagation v_z travelling nearly perpendicular to the cell windows have a much longer interaction time than atoms with a high v_z. (b) Comparison of a Dicke narrowed absorption signal (purple line) to a Doppler broadened absorption (grey area)

red tail, demonstrated as a red line in Fig. 3.1c.

To model this effect for fitting, position dependent shifts are calculated across the entire cell, according to a modelled atomic positional distribution. The distribution is quadratic across the cell length and is calculated from a fit of results from a Monte-Carlo simulation of expected atomic positions inside the cell [3]. This is discussed further in section 3.4. The shift of atoms across the cell is collected into a function that represents the proportion of atoms shifted to a particular detuning. This is plotted as a purple area on Fig. 3.1c. Each point on the distribution represents the strength of the response of an atom shifted to detuning Δ by the AS interaction. Zero detuning is set at the origin of the plot, and is the 'bare' atomic transition frequency. Note that the shift function abruptly stops at the detuning corresponding to the largest AS separation $L/2$, where L is the length of the vapour cell in the direction of beam propagation. This function is convolved with a velocity shifted line-shape, shown in panel (c) as a grey area. The two absorption line-shapes are convolved, to generate the final AS shifted spectrum, plotted as a red line on panel (c).

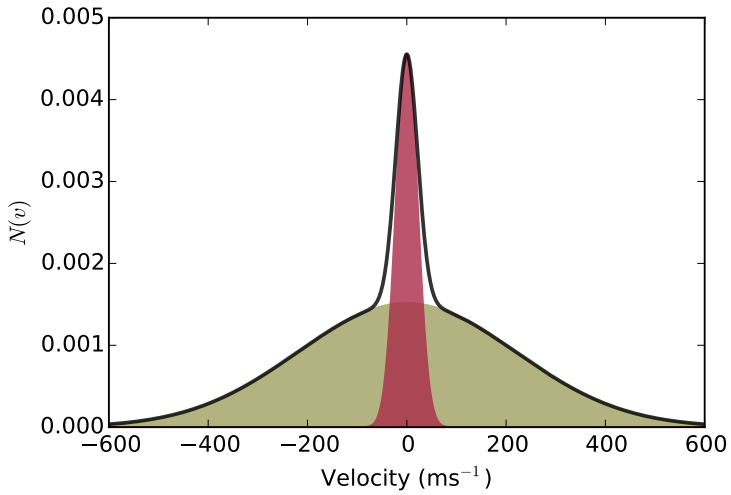

Figure 3.3: Example bimodal velocity distribution used in the line-shape model. The full distribution is plotted as a black line, with the contributions G_{fast} and G_{slow} plotted as yellow and red areas respectively.

3.2.2 Dicke narrowing

The most pronounced change to the absorption and transmission line-shape of a vapour confined in a nm scale cell is the suppression of the Doppler broadening, evidenced by a much narrower and stronger Lorentzian component of the line-shape, plotted as a purple line in Fig. 3.2b. For comparison a Doppler broadened absorption line-shape that is observed in a standard length vapour cell is plotted as a grey area. This suppression is caused by the extreme confinement of the vapour in the direction of beam propagation.

Typical cell lengths used for experiments in this thesis range between 30-2000 nm, with a beam waist of around 30 μm. Hence, the excitation region is pancake shaped. If we first consider atomic trajectories inside the interaction region, shown in Fig. 3.2a, we can build an understanding about the narrowing effect. To do this we will compare the absorbative response of atoms with high and low velocity in the direction of beam propagation.

Atoms travelling with a high v_z have a very short interaction time before a collision event with the cell walls, where they de-excite and no longer contribute to the atomic signal. If the vapour is sufficiently dilute, wall collisions are the dominant source of these de-excitation events. This is because the cell length is much shorter then the mean free path of the atoms. Hence when the vapour is dilute there will be no inter-atomic collisions

that alter the atomic trajectories or cause de-excitation events. Furthermore, the time taken for the atom to traverse the cell is shorter than the lifetime of the excited state, 27 ns, so it is unlikely that the atom will naturally decay by itself.

Atoms with a low v_z, travelling at a low angle θ relative to the walls have a very low Doppler shift and a much longer interaction time. They therefore have a dominant contribution to the transmitted signal. This suppression of the Doppler shifts results in a spectrum that is dominated by a Lorentzian line-shape on a weak Doppler broadened background. This phenomenon is known as Dicke narrowing [4], first observed in atoms confined with buffer gases, with the buffer gas atoms providing the collisions required to suppress the Doppler broadening [5].

For a full description of this effect, we must also consider the phase of the atoms. A beam travelling through the atomic medium will be collected further downstream, and so the signal is a sum of the incident laser light and the light emitted by the resonant medium.

We assume that the excited atoms start from one wall of the cell, in phase with the laser, picking up a phase e^{ikz} as it moves across the cell before reaching the opposite wall. The atom has picked up an overall phase shift of kL after travelling across a cell of length L. The atom then collides with the opposite wall, de-exciting and emitting a photon shifted by kL. We assume the atomic trajectories have a uniform distribution, meaning that atoms are equally likely to depart from either wall, emitting with a phase of $\phi = \pm kL$. Hence, at cell lengths of $(2n+1)\lambda/2$, signals from wall collisions are maximally cancelled, suppressing the Doppler contribution. At integer multiples of λ, there is no such cancellation and the full Doppler profile is recovered.

This is known as the 'collapse and revival' of a Dicke narrowed line-shape, and is well documented, first observed by Dutier *et al.* in 2005 [6]. As the cell length increases the signal will oscillate between Dicke narrowed and Doppler broadened peaks. When the cell length approaches the mean free path, the Dicke narrowing effect is washed out, although has been observed up to lengths of $9\lambda/4$ [7].

We model this using a bimodal velocity distribution, fully described in [3]. In short, the velocity distribution is split into two Gaussian components, one representing atoms with a high v_z that is broad with a small amplitude, G_{fast}, and a second describing atoms with

low v_z that is narrow with a large amplitude G_{slow}:

$$g(v) = C(AG_{\text{fast}} + (1 - A)G_{\text{slow}}), \tag{3.2}$$

where

$$G_{\text{fast}} = \exp\left(-\frac{v^2}{u^2}\right), G_{\text{slow}} = \exp(-\frac{v^2}{(su)^2}), \tag{3.3}$$

with C as a normalisation constant. A represents the ratio of slow to fast atoms, typically taking values on the order of 10^{-1} to 10^{-4}. The parameter s is a narrowing factor for the slow atoms, and when used in fitting is set to be $s = 10^{-5}$. The resulting velocity distribution is plotted in Fig. 3.3 as a black line, with G_{fast} plotted as a yellow area and G_{slow} as a red area. This was plotted using an $A = 0.1$ and $s = 1 \times 10^{-3}$, values much larger than typical fitting parameters used for illustrative purposes to demonstrate the basic form of the distribution. When calculating nanocell line-shapes, the bimodal velocity distribution $g(v)$ is substituted for the Doppler distribution when performing the convolution to generate a Voigt line-shape.

To verify the accuracy of the bimodal velocity distribution, a Monte-Carlo (MC) simulation of atomic trajectories was performed and the modified position and velocity distributions were included in the line shape model, as well as a $1/r^3$ atom surface potential that induces a force $F = -\mathrm{d}U_{\text{vdW}}/\mathrm{d}z$ across the cell. In this simulation we assume that the atom-light interaction region is a box with dimensions $w \times w \times L$, where $w = 40$ μm is the $1/\mathrm{e}^2$ diameter of the excitation laser beam used in the experiment and L is the length of the nanocell. The atoms are randomly placed uniformly across a region which is 4 times larger than the interaction region ($4w \times 4w \times L$), to account for atoms transiting into the interaction region during the simulation. The atoms are given random velocities according to Maxwell-Boltzmann statistics, and their motion is simulated over a time (1 μs) which is large compared to the lifetime of the excited state. No other decay mechanisms are included. Desorption effects are neglected, so atoms that hit the walls or move out of the interaction region are lost. This is justified since desorption processes are expected to happen on time scales much longer than the interaction time [8]. Additionally, the walls have an attractive atom-surface (AS) force present, a short range effect present in nanocells that will be discussed later in this chapter.

The results of the simulation are shown in Fig. 3.4, where dashed red (blue) lines show the results of the model without (with) AS forces present. Panel (a) shows the position-dependent interaction times of atoms inside the cell. When there is no AS force present

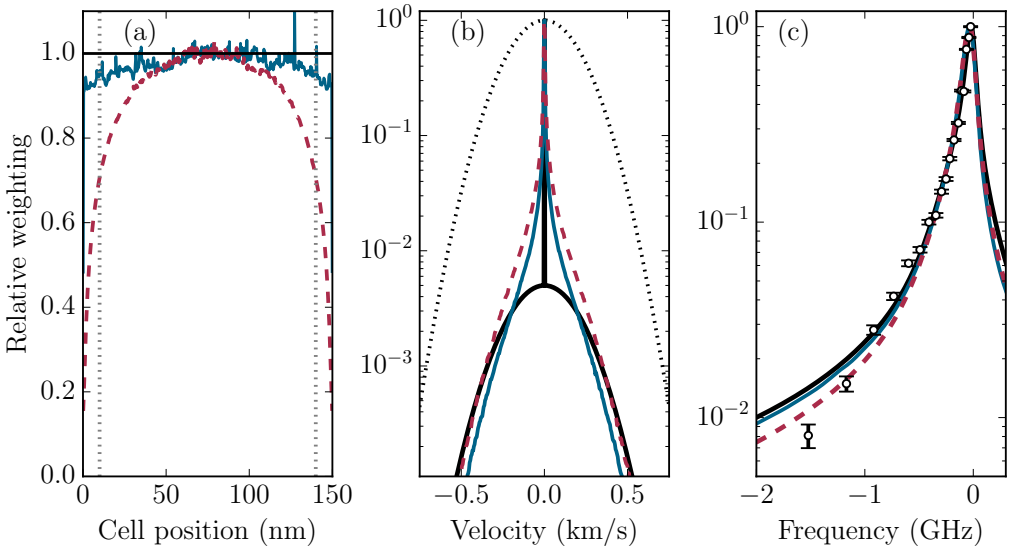

Figure 3.4: Monte-Carlo simulations of atomic trajectories to test the appropriateness of the Dicke narrowing model used in our fitting. Simulations are performed with no AS force present (blue lines) and including the effect of the AS force (dashed red lines). These are compared to the bimodal distribution used in our fitting procedure (thick black lines). In panel (a) the weighting of contributions to the line shape for atomic positions inside the cell is shown. The grey dashed lines mark 10 nm from the cell walls, where the AS force starts to have a considerable effect on the atoms. Panel (b) shows the velocity distribution of atoms. The distribution used in our model (black line) is in reasonable agreement with the simulations for atoms unaffected by the AS force (blue line) and atoms which have been accelerated towards the walls (dashed red line). For comparison, the Maxwell Boltzmann distribution expected in cm scale vapour cells is shown (dashed black line). (c) A comparison of the resulting line-shapes from each velocity distribution with experimental data points and their associated errors are shown as white points. Simulation results courtesy of James Keaveney

(dashed red line), atoms are more likely to be found near the centre of the cell. With the AS force present (red dashed lines), atoms are pulled towards the edge of the cell and the distribution becomes significantly flatter.

Panel (b) compares the MC simulated (blue line) velocity distribution of the atoms to the bimodal distribution used in the model (solid black line) and the Gaussian distribution expected for a Doppler-broadened medium (dotted black line). The bimodal distribution is a reasonable approximation to the continuous distribution predicted by the MC simulation. After the convolution with the homogeneous contribution to the line-width (from collisional broadening, etc.), the difference in the full absorption line shape between the bimodal and MC velocity distributions is very small, as evidenced in Fig. 3.4(c), where the change between the line shapes from the phenomenological bimodal distribution (solid black line) and the continuous distribution (solid blue line) is well within the error margins of experimental data (white points), validating the use of the bimodal model.

The Dicke narrowing effect means that nanocells are an excellent tool for sub-Doppler spectroscopy. The width of lines can approach the natural line-width; at low enough temperatures all hyperfine transitions on the Rb D2 line can be resolved. Additionally only a single beam is required to achieve sub-Doppler line-widths, simplifying experimental set-ups and resulting in no crossover resonances.

3.2.3 Etalon Effects

Due to the extremely thin length of the cells, interior windows must be highly polished (mean arithmetic surface roughness, $R_A < 3$ nm) to avoid large length variations inside the cell. Such high quality surfaces result in weakly reflecting interior surfaces, meaning that a weak Fabry-Perot (FP) etalon is formed inside the cell when a laser beam is incident on the cell. The finesse $\mathcal{F}$ is extremely low, typically around $\mathcal{F} = 3$, but this still has an observable impact on the transmitted line-shape.

The response can be thought of as the summation of electric fields inside the medium. We consider a dilute atomic gas of thickness L confined between two dielectric slabs with refractive index n excited by an incident laser within the weak probe limit. In this context, the requirement of a dilute gas means that atoms follow straight trajectories when travelling from wall to wall, with no inter-atomic collisions altering their path or

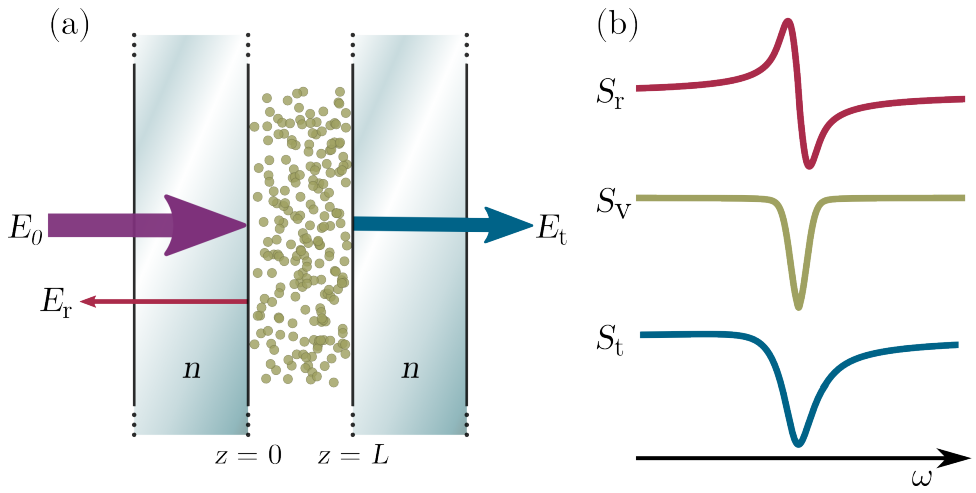

Figure 3.5: Breakdown of mixing of reflection and transmission line-shapes in a nanocell. Panel (a) shows the electric fields interacting inside the cell that result in a mixed line-shape. Incident field E_0 enters the cell and splits into a reflected field E_r and transmitted field E_t. The transmitted field first propagates through the cell from location $z = 0$ to $z = L$, interacting with the vapour as it propagates. The resultant signals of each stage are shown in panel (b). The reflected signal S_r, plotted in red, is a dispersive selective reflection line-shape that has a heavy dependence on the frequency dependent refractive index of the line-shape. The vapour response S_v, plotted in beige is the standard absorbative response of the atomic vapour. Usually the reflected signal S_r is negligible compared to the amplitude of the vapour response, but when propagation lengths are extremely short, it must be factored into the final transmitted signal S_t, plotted as a blue line. The resulting signal is a mix of the usual reflected and transmitted line-shapes that is slightly asymmetric; one shoulder is steepened in gradient and the other is shallower.

causing de-excitation events. To find the final transmission signal, we can again consider the signal detected as a sum of fields downstream from the cell. This is illustrated in Fig. 3.5a. The figure shows a resonant incident field E_0 reaching the interior surface of the cell at length boundary $z = 0$. At this boundary, part of the beam is weakly reflected, represented as field E_r. The beam then interacts with the vapour, experiencing the absorbative response that has been described in earlier sections, the resulting signal S_v is plotted as a beige line in panel (b). It is then transmitted as beam E_t, modified by FP effects inside the cell. Hence, E_t is the usual absorbative response of the vapour, modified by the FP signal of an empty cell, with reflected field E_r subtracted from it.

Field E_r is a selective reflection (SR) signal. SR signals probe the medium via an evanescent wave, with a variation in intensity that is dependent on the reflectivity of the dielectric/vapour interface. The reflectivity is therefore dependent on the refractive index of the vapour [9], resulting in a dispersive signal S_r, plotted in red on panel (b) of Fig. 3.5. Signal S_r is very weak, and so for longer cell lengths exceeding tens of microns, its contribution to the signal can safely be neglected. However, for cells with lengths comparable to the excitation wavelength, its contribution is relatively much larger and should be accounted for in a full theoretical model.

The final transmitted signal is plotted in blue on Fig. 3.5b. The response, usually symmetrical about the resonant frequency, is distorted; one wing is sharper and has a larger amplitude, sometimes increasing above $\Delta\mathcal{T} = 1$ and the other is broadened and decreased in amplitude. It should be noted that the increase in amplitude is not evidence of optical pumping, but instead emanates from the subtraction of the SR signal. The size of these distortions varies with cell length and depends on the FP resonance inside the cell cavity.

The evolution of the Cs D1 line (excitation wavelength $\lambda = 895$ nm) with length is plotted for experimental data in Fig. 3.6. It clearly displays how the effect oscillates between the wings periodic with the cell length, with the increased signal moving from the red wing to the blue wing, with a transitional period in between at lengths of half integer multiples of λ where the signal reverts to an entirely symmetrical shape. This shift is caused by FP resonance of the cell cavity. Of interest on Fig. 3.6 is a false red and blue shift of the resonance, demonstrated in the right hand inset. This shift is not related to any actual shift in transition frequency and is simply an artefact of the altered line-shape.

This effect is only observed in vapours that are optically thin, *i.e.* the length probed

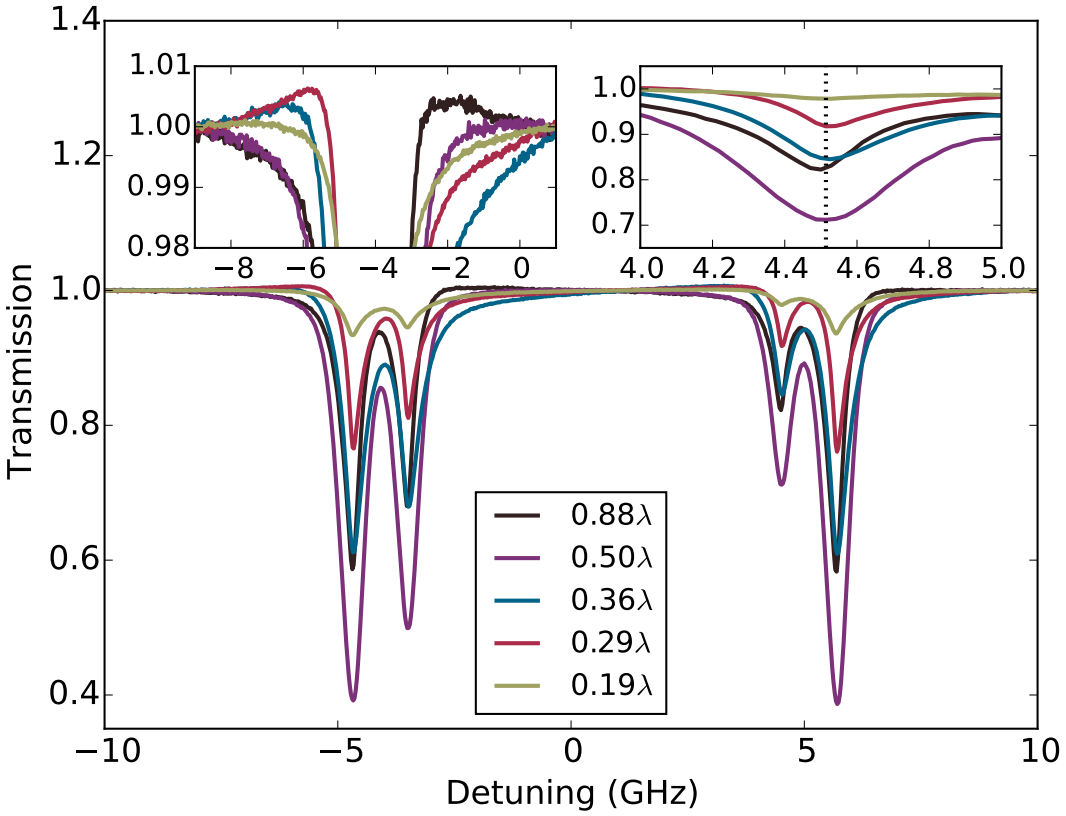

Figure 3.6: Length dependence of the Cs D1 line from 0.19-0.88 λ demonstrating the effects of mixing of reflection and transmission line-shapes. Left inset shows the oscillation of the steepened shoulders, from a steep shoulder on the red wing (maximal on the figure at $L = 0.29\lambda$, plotted in red), to a symmetrical line-shape at $L = 0.5\lambda$, plotted in purple. Finally, the steepened blue wing, maximal on the figure at $L = 0.88\lambda$ is plotted in black. The right inset demonstrates the apparent shift caused by the mixing of the two line-shapes. The actual transmission frequency is plotted as a black dashed line, and the symmetrical line-shape from $L = 0.5\lambda$ is centred around it. There are apparent red and blue shifts arising from the mixed line-shapes. These shifts to not correspond to an actual shift in atomic transition frequency and are merely a result of the mixing of reflected and transmitted electric fields.

is comparable to the excitation length. This is partially because the reflected field is so weak that its contribution can safely be neglected when studying signals from longer cells, as the transmitted absorption is significantly stronger than the reflected component. Secondly, the theory is derived on the based on the assumption that atoms departing from both the front and back surfaces experience the same excitation field strength [10], which would not be the case in longer cells.

A full description of this effect can be found in [11], which outlines how to generate theoretical line-shapes for a dilute alkali vapour confined in an extremely thin cell. To fully account for this effect the line-shape must be calculated using density matrix element ρ_{ba} derived in chapter 2. To describe the vapour response, [11] integrates the atomic susceptibility over all velocities to find the field modifications for the transmitted and reflected intensities I_{T} and I_{SR} respectively. We can express I_{T} as:

$$I_{\mathrm{T}} = \int_{-\infty}^{\infty} J_1 + J_2 + J_3 dv. \tag{3.4}$$

The integral is split into 3 components; a Doppler broadened contribution, J_1, a transient Dicke narrowed contribution, J_2, and a third term that oscillates in sign representing the length dependent 'collapse and revival' of the Dicke narrowing effect, J_3. Each component of this integral is discussed and illustrated in [12]. The vapour response is then included in a final summation of all electric fields resulting in accurate representation of atomic line-shapes skewed by reflection effects.

However, the model is unsuitable for use in fitting procedures. SR line-shapes cannot be fully described using just the refractive index and instead the surface admittance should be calculated. For a completely accurate line-shape the density matrix element ρ_{eg} must also be calculated for every step [13]. This results in extremely lengthy calculations for a single line-shape. Furthermore, all descriptions require a dilute vapour, with negligible inter-atomic collisions taking place. To gather transmission line-shapes from such a thin cell, we require high temperatures where significant numbers of collisions are taking place, requiring an adjustment to the model that is beyond the scope of this thesis. Finally, the motional effects on the line-shape cannot be included using a easily implemented convolution; SR line-shapes must be split according to positive and negative atomic velocities [11]. Hence it is not a suitable model for use in fitting.

We therefore use a simpler description of the line-shape. It does not apply the full FP effect and excludes the surface admittance, and hence cannot fully describe an SR line-

shape. Therefore it can only be applied in limited situations. It is, however, sufficient for use in transmission spectra studied herein. The model is fully outlined in [3]. The reflective response is derived using the impedance mismatch between the dielectric cell windows and atomic layer. The cell windows used in experiments herein are identical and have an impedance of $Z_{\mathrm{W}} = 1/n_{\mathrm{sapphire}}$. To calculate the impedance arriving at the first dielectric/vapour boundary, we must consider the impedance resulting from the electric field back-reflected from the back window of the cell and propagating through the atomic vapour layer. The total impedance Z_{T} can be calculated using thin film theory [14]:

$$Z_{\mathrm{T}} = \frac{Z_{\mathrm{W}} - \mathrm{i}Z_{\mathrm{A}} \tan(kL)}{1 - \mathrm{i}\frac{Z_{\mathrm{W}}}{Z_{\mathrm{A}}} \tan(kL)}, \tag{3.5}$$

where $Z_{\mathrm{A}} = 1/n(\omega)$ is the impedance of the atomic layer.

A frequency dependent reflection line-shape $\mathcal{R}(\omega)$ is then found by calculating the impedance mismatch between the first window and the total back reflected impedance Z_{T}:

$$\mathcal{R}(\omega) = \left| \frac{Z_{\mathrm{T}} - Z_W}{Z_{\mathrm{T}} - Z_W} \right|^2. \tag{3.6}$$

Hence, the final transmitted line-shape $\Delta\mathcal{T}_{\mathrm{R}}(\omega)$ can be calculated as an alteration to the unmixed transmission signal $\Delta\mathcal{T}(\omega)$:

$$\Delta\mathcal{T}_{\mathrm{R}}(\omega) = C\Delta\mathcal{T}(\omega)(1 - \mathcal{R}(\omega)), \tag{3.7}$$

where $C = 1/1{-}\mathcal{R}_0(\omega)$ is a normalisation constant, with $\mathcal{R}_0(\omega)$ as the reflection coefficient from Eq. 3.6 calculated for a layer index of $n_{\mathrm{T}} = 1$ (*i.e* $Z_{\mathrm{T}} = 1$).

This simplified model produces sufficiently accurate results that have a sharp, increased transmission signals on the red wing, oscillate with length, and include the cancellation of any mixing of reflection and transmission for cells with lengths that are half integer multiples of λ.

However, although this treatment is sufficient for line-shapes that have a sharp shoulder on the red wing, this thin layer model does not produce spectra with sharp shoulders on the blue wing. This is because although the model accounts for some mixing of reflective and transmission spectra, it does not account for the full FP response of the cell. The model also uses only the frequency dependent refractive index, instead of a full SR line-shape. However, this model is sufficiently accurate to be applied half of the lengths available inside the nanocell.

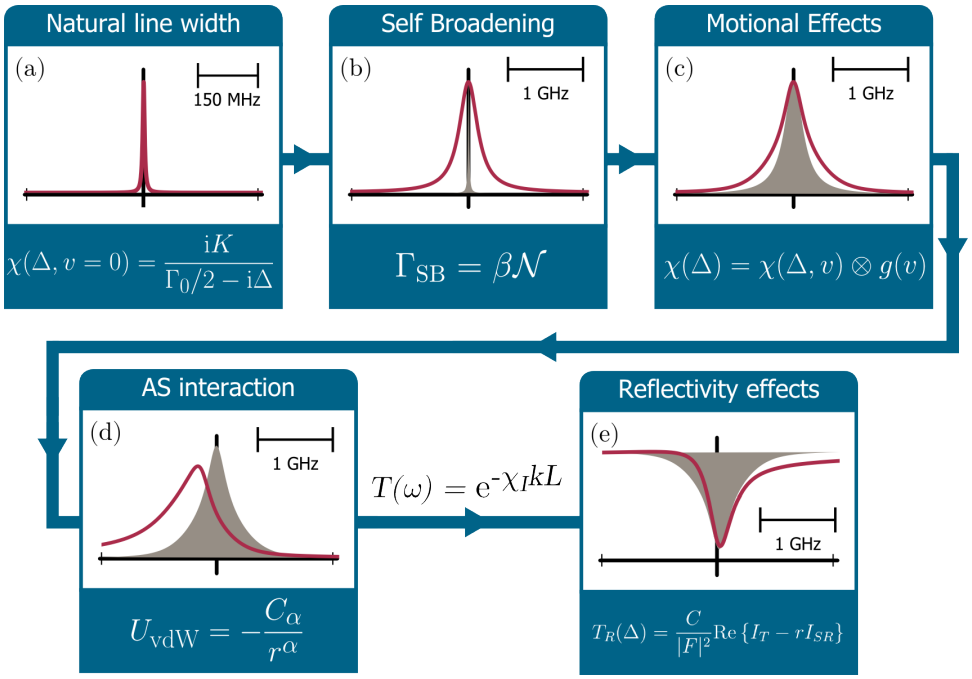

Figure 3.7: Fitting process for nanocell spectra with the most relevant equations for each step. The resultant line-shape for each step is plotted as a red line, with the previous step plotted as a grey area for comparison.

Furthermore, this effect is only noted in transmission spectra, or detection methods where summations of coherent light interactions downstream are measured. The main fitting results of this thesis, found in chapter 5, centre around spectra taken by measuring off-axis incoherent scattered light. Such spectra are unaffected by internal reflections and so these results will not be impacted by an incomplete model.

3.3 Fitting nanocell spectra

The fitting of nanocell spectra follows a similar process to that outlined in the previous chapter. However, there are three changes to include the effects discussed in this chapter. Each stage for the fitting is outlined on Fig. 3.7. The figure follows the same convention as that in the chapter 2; the step being performed is plotted as a red line, with the previous step plotted as a grey area for reference. Each step is accompanied by the most relevant equation describing the process. The first steps are identical to the non-nanocell case; the self-broadened natural line-shape is calculated using atomic constants,

transition frequencies the vapour temperature and an fitting parameter accounting for excess broadening Γ_{ex}. Often used as a fitting parameter in this step is the vapour temperature.

The excess broadening parameter Γ_{ex} accounts for a surplus Lorentzian broadening that is consistently observed in nanocell spectra, but the source is unaccounted for. We suspect the source of this broadening may be radiation trapping inside the cell, but currently have no method of modelling this. Using Γ_{ex} returns sufficient fits, but finding a source for this broadening is a future avenue of investigation.

To account for Dicke narrowing, the Doppler line-shape is replaced with a Dicke narrowed contribution, following the distribution in Eq. 3.2. The modified line-shape is then convolved with the natural line-shape to create a Dicke narrowed Voigt profile. The Dicke narrowing parameter a, describing the ratio of 'fast' to 'slow' atoms is always used as a fitting parameter in this step, affecting how narrow the final line-shape will be.

Accounting for the atom surface interaction, AS induced shifts across the entire cell length are calculated using $U_{\text{vdW}} = -C_3/r^3$, then weighted by a parabolic function representing the positional distribution of atoms inside the cell. This function is then convolved with the Voigt line-shape to generate an AS shifted spectrum. Full details on this process can be found in [3].

The change in transmission $\Delta\mathcal{T}$ is then calculated using Eq. 2.31. The transmission line-shape is then modified for the effect of multiple internal reflections inside the cell according to Eq. 3.7. The signal is normalised by dividing by the reflective response of a non-resonant vapour. The cell length has a strong impact on both the overall absorption and the reflective effects, and is occasionally used as a fitting parameter.

3.4 Conclusion

We have developed a sufficient model of the line-shape that can be included in fitting procedures. There are two main simplifications made in the theory. Firstly, the velocity distribution has been simplified to a bimodal Gaussian distribution that represents contributions from atoms with a high and low velocity in the direction of beam propagation. This simplification has been very well justified through a Monte-Carlo simulation.

The simulation confirmed that the bimodal distribution is an excellent approximation of the velocity distribution inside the nanocell, and that any departures are outside of experimental sensitivity.

The second simplification is excluding the full theory of reflective effects inside the cell. This theory requires repeated solutions of the optical Bloch equations for every fit attempt, an inefficient method for computational fitting. We opt instead for a simple thin film analysis, that unfortunately only covers half of the available lengths inside the cell. This is still sufficient for a line-shape model for experiments presented in this thesis, as many investigations herein are performed by collecting off-axis scattered light, unaffected by coherent sums of light downstream like the reflectivity or coherent Dicke narrowing effects. Hence, the model is sufficient for the fitting of spectra used in this thesis.

Bibliography

[1] I. G. Hughes and T. P. A. Hase, *Measurements and their Uncertainties: A practical guide to modern error analysis* (OUP, Oxford, 2010).

[2] J. E. Lennard-Jones, Trans. Faraday Soc. **28**, 333 (1932).

[3] J. Keaveney, Ph. d. thesis, Durham University (2013).

[4] R. H. Dicke, Phys. Rev. **89**, 472 (1953).

[5] J. P. Wittke and R. H. Dicke, Phys. Rev. **103**, 620 (1956).

[6] G. Dutier, A. Yarovitski, S. Saltiel, A. Papoyan, D. Sarkisyan, D. Bloch, and M. Ducloy, EPL (Europhysics Letters) **63**, 35 (2003).

[7] D. Sarkisyan, T. Varzhapetyan, A. Sarkisyan, Y. Malakyan, A. Papoyan, A. Lezama, D. Bloch, and M. Ducloy, Phys. Rev. A **69**, 065802 (2004).

[8] H. de Freitas, M. Oria, and M. Chevrollier, Appl. Phys. B **75**, 703 (2002).

[9] J. Guo, J. Cooper, A. Gallagher, and M. Lewenstein, Opt. Comm. **110**, 197 (1994), ISSN 0030-4018.

[10] B. Zambon and G. Nienhuis, Opt. Comm. **143**, 308 (1997).

[11] G. Dutier, S. Saltiel, D. Bloch, and M. Ducloy, J. Opt. Soc. Am. B **20**, 793 (2003).

[12] S. Briaudeau, S. Saltiel, G. Nienhuis, D. Bloch, and M. Ducloy, Phys. Rev. A **57**, R3169 (1998).

[13] A. Sargsyan, P. A. Petrov, T. A. Vartanyan, and D. Sarkisyan, Opt. Spektrosk. **120**, 339 (2016).

[14] G. Brooker, *Modern Classical Optics*, Oxford Master Series in Physics (OUP, Oxford,

2003).

Chapter 4

The Kramers-Kronig relations and the Hilbert transform

Causality is an important theme in physics and when its consequences are considered from a quantum and atomic optics perspective, relations between the real and imaginary part of the optical response can be derived. For example, the Kramers-Kronig (KK) relations [1, 2] link the real and imaginary parts of the optical response, which relate to the refractive index and opacity of a medium respectively, as seen in chapter 2. The KK relations are widely used in many fields of physics and electronics [3], including plasmonics [4], and electron spectroscopy [5], superluminal propagation [6, 7] and quantum memories [8], and find utility in applications such as light propagation, including pulse stopping [9].

In this chapter we explore the KK relations, discussing when they can and cannot be applied in atomic physics and discussing possible implementation methods. However, the KK relations can be complex to implement, so we present an alternative but equivalent calculation method applied in other fields such as signal processing using the Hilbert transform (HT). The HT drastically reduces calculation times and is much simpler to implement. We then discuss its advantages as a tool for atomic physicists, looking at possible applications.

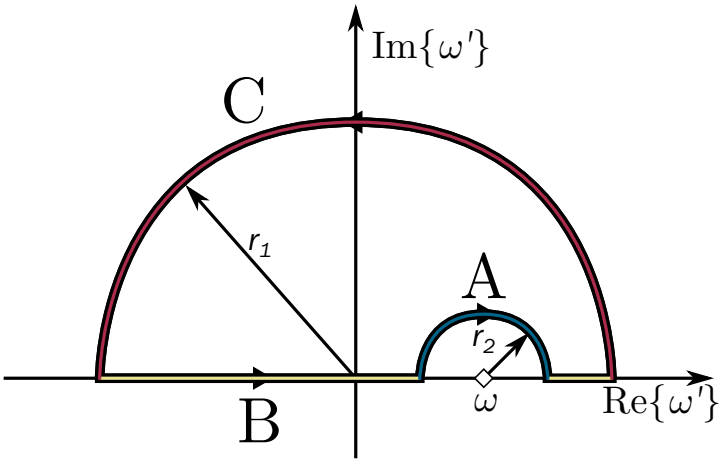

Figure 4.1: Contour on the complex plane used to solve the integral in equation 4.1, consisting of 3 sections, a large outer circle with radius r_1, highlighted in red. Next, a small inner circle with radius r_2 that surrounds the pole at $\omega' = \omega$, highlighted in blue. Across the real axis is the third section highlighted in yellow.

4.1 KK relations: derivation

In order to derive the KK relations for a frequency dependent linear (first order) susceptibility $\chi(\omega)$, there are two requirements. Firstly, $\chi(\omega)$ is complex. Secondly, $\chi(\omega)$ must be analytic in the upper half of the complex plane, i.e. it is single-valued and has no singularities at $\mathrm{Im}\,\omega \geq 0$.

Partially following the derivation in [10], the KK relations can be found by considering integral I:

$$I = \mathcal{P} \int_{-\infty}^{\infty} \frac{\chi(\omega')}{\omega' - \omega} \mathrm{d}\omega', \tag{4.1}$$

where $\mathcal{P}$ denotes the Cauchy principal value. A solution to Eq. 4.1 is found by integrating over the contour shown in Fig. 4.1. The contour is chosen such that no poles (singularities) lie inside it. Eq. 4.1 only has one pole, which lies at $\omega = \omega'$, which is avoided by line A, a semicircle of radius r_2, highlighted in blue on Fig. 4.1. Line B lies across the real axis and is highlighted in yellow, and represents $\chi(\omega)$, the solution that we are seeking. The rest of the contour is bounded by line C, a semicircle of radius r_1, highlighted in red. The contour is followed in an anti-clockwise direction, with the solution expressed as a sum of each individual section of the contour:

$$\oint \frac{\chi(\omega')}{\omega' - \omega} \mathrm{d}\omega' = \int A + \int B + \int C. \tag{4.2}$$

No poles lie within the contour, so the Cauchy integral theorem [11] states that

$$\oint \frac{\chi(\omega')}{\omega' - \omega} \mathrm{d}\omega' = 0. \tag{4.3}$$

The radius r_2 is reduced to zero. Hence, using the residue theorem [11], the solution to the integral of line section A is

$$\int A = -i\pi\chi(\omega'). \tag{4.4}$$

Radius r_1 will be pushed to infinity. $\chi(\omega')$ tends towards zero at large ω', and so the $1/|\omega'|$ component dominates, and as a result $\int C = 0$. The solution for section B is simply $\int B = \chi(\omega)$. Substituting the integral solutions into equation 4.2 and rearranging:

$$\chi(\omega) = \frac{1}{i\pi}\mathcal{P}\int_{-\infty}^{\infty} \frac{\chi(\omega')}{\omega' - \omega} d\omega'. \tag{4.5}$$

The imaginary factor on the right hand side of the equation is what results in the relation between real and imaginary parts of a complex causal function, discussed further in section 4.2.1. Recalling that $\chi(\omega)$ is complex, equation 4.5 can be split into its real and imaginary components, resulting in the well known KK relations:

$$\chi_{\mathrm{R}}(\omega) = \frac{1}{\pi}\mathcal{P}\int_{-\infty}^{\infty} \frac{\mathrm{Im}\{\chi(\omega')\}}{\omega' - \omega} d\omega'. \tag{4.6}$$

$$\chi_{\mathrm{I}}(\omega) = -\frac{1}{\pi}\mathcal{P}\int_{-\infty}^{\infty} \frac{\mathrm{Re}\{\chi(\omega')\}}{\omega' - \omega} \mathrm{d}\omega'. \tag{4.7}$$

However, these relations stretch over all frequencies, positive and negative. To eliminate the unphysical negative frequencies, we can use another mathematical property of χ, that $\chi(-\omega) = \chi(\omega)^*$, noting that a * denotes a complex conjugate. This relation is expanded on in appendix B. We now apply this relation to equations 4.6 and 4.7. The integrals are split into positive and negative components then rearranged using this relation to yield expressions for the KK relations that extend only over positive frequencies:

$$\chi_{\mathrm{R}}(\omega) = -\frac{2}{\pi}\mathcal{P}\int_{0}^{\infty} \frac{\omega'\mathrm{Re}\{\chi(\omega')\}}{\omega'^2 - \omega^2} d\omega'. \tag{4.8}$$

$$\chi_{\mathrm{I}}(\omega) = \frac{2\omega}{\pi}\mathcal{P}\int_{0}^{\infty} \frac{\mathrm{Im}\{\chi(\omega')\}}{(\omega'^2 - \omega^2} d\omega', \tag{4.9}$$

Hence, we have an expression relating the real and imaginary parts of a suitable function.

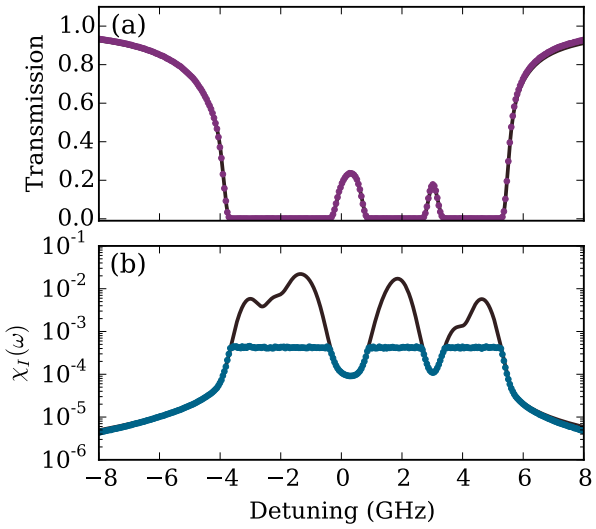

Figure 4.2: Panel (a): A comparison of measured (purple points) and theoretical transmission (black line). Panel (b) shows the imaginary susceptibility inferred from the measured transmission (blue points) and theoretically modelled from ElecSus (black line).

4.1.1 Applicability

Additionally, the KK relations are not applicable to every atomic system, although they do apply to all systems discussed in this thesis. However, the KK relations are invalidated if the function being transformed is no longer analytic in the upper half of the complex plane. This occurs when there are poles at positive imaginary values. This is the case for many media with a third order non-linear susceptibility [10]. Apparent violation of KK relations has also been observed in quasi-2d silicon crystals [12]. It should be highlighted that these cases do not mean the rules of causality are broken, but are instead cases where the KK relations are not applicable.

The KK relations cannot be applied to optically thick vapours. $\chi_{\mathrm{I}}(\omega)$ cannot be fully measured for an optically thick vapour, as detection methods would need to be sensitive to immeasurably small changes, beyond the noise limit of current detectors. This is highlighted in Fig. 4.2, which compares an experimentally measured transmission spectrum from a 2 mm cell at T = 179°C (purple points) to a theoretically generated line-shape. For transmission spectra, there is no apparent change. But, when $\chi_{\mathrm{I}}(\omega)$ is examined, there is a large disparity of over 2 orders of magnitude which will only get larger as optical density increases, cutting off many details and variations in $\chi_{\mathrm{I}}(\omega)$. Detection of

these features would require sensitivity to relative changes in signal that are on the order of $10^{-}100$. Hence an measurement of the real susceptibility via the KK relations will be highly inaccurate. These inaccuracies stem from the extremely small signal changes, resulting in the loss of signal in experimental signal-to-noise ratios and hence the KK relations cannot be applied to infer the refractive index of an optically thick vapour.

4.1.2 Computation

The KK relations offer an alternative to detection of difficult or impossible to measure quantities. In the case of atomic physics, measurement of the refractive index is experimentally time consuming, but measurement of absorption is simple. Hence, it is often preferred to infer the refractive index from calculation of the KK relations. However, this requires integration over all positive frequency space for every frequency point being calculated. Care must also be taken to avoid singularities in the calculated spectrum at $\omega = \omega'$.

Calculation times can take several seconds, although the time taken to create a working efficient KK code is extensive and requires good levels of coding skill. Accordingly, this keeps refractive index measurements somewhat inaccessible, despite the fact that refractive index spectra can shed much light on atomic interactions.

4.2 The Hilbert transform

The KK relations are excellent for inferring difficult to measure properties but implementation is challenging. A simpler solution can be found by considering causal functions from a time domain perspective. We consider a general causal function, defined as a function that has a value of 0 before time $t = 0$, where some initial input or excitation takes place. This is illustrated as function $h(t)$ on Fig. 4.3. We start by taking such a function in the time domain, then exploit the inherent mathematical properties of causal functions to find a relation between real and imaginary components in the frequency domain.

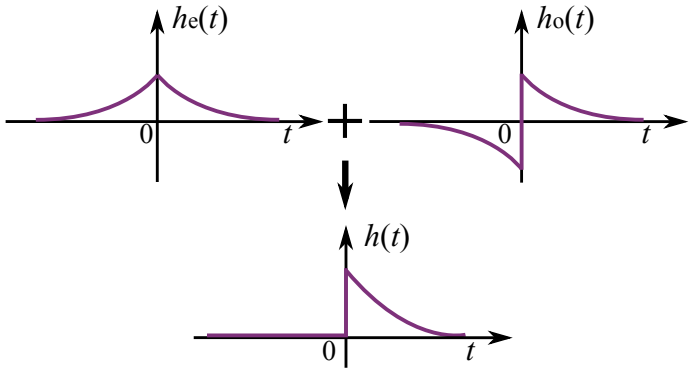

Figure 4.3: Illustration of the additive property of odd $h_o(t)$ and even $h_e(t)$ components of causal function $h(t)$ (listed as property (1) in the text).

4.2.1 Causality in the time domain

For the derivation, we need a mathematical toolbox using properties of causal functions and the signum function:

1. Any causal function $h(t)$ can be expressed as a sum of even, $h_e(t)$, and odd, $h_o(t)$, components [13], see Fig. 4.3.
2. The Fourier transform of $h_e(t)$ is purely real [13].
3. The Fourier transform of $h_o(t)$ is purely imaginary [13].
4. The signum function, defined as $\mathrm{sgn}(t) = -1$ for $t < 0$ and $+1$ for $t > 0$ converts an even function to an odd function and vice versa [13].
5. The Fourier transform of $\mathrm{sgn}(t)$ is $\frac{1}{i\pi\omega}$ [14].

Fig. 4.3 illustrates some of these properties. Panel (a) illustrates tool 1, the summation of odd and even functions creating a causal function that has no response below $t = 0$. Using these properties, we can apply them to a real and causal function $h(t)$. Using tool (1), and following the discussion in [13], we express this as a sum of its odd and even components:

$$h(t) = h_e(t) + h_o(t). \tag{4.10}$$

Using the signum function, (4), $h(t)$ can be expressed as a sum of its purely odd components:

$$h(t) = h_o(t) + \mathrm{sgn}(t)h_o(t). \tag{4.11}$$

We then take the Fourier transform to express $h(t)$ in the frequency domain, denoted as $H(\omega)$. This will eventually give a link between the real and imaginary components of $H(\omega)$. To understand this, we must examine the Fourier transform of equation 4.11:

$$\mathcal{F}[h(t)] = \mathcal{F}[h_{\mathrm{o}}(t)] + \mathcal{F}[\mathrm{sgn}(t)] * \mathcal{F}[h_{\mathrm{o}}(t)]. \tag{4.12}$$

Multiplication in the time domain becomes a convolution in the frequency domain, denoted as $*$. Expressing the Fourier transforms in the frequency domain and using tool (5) to replace $\mathcal{F}[\mathrm{sgn}(t)]$ with $1/i\pi\omega$:

$$H(\omega) = H_{\mathrm{o}}(\omega) + \frac{1}{i\pi\omega} * H_{\mathrm{o}}(\omega). \tag{4.13}$$

The final term in this equation is a convolution between the kernel $1/i\pi\omega$ and $H_{\mathrm{o}}(\omega)$, which can be expanded to:

$$\frac{1}{i\pi\omega} * H_{\mathrm{o}}(\omega) = \frac{1}{\pi}\mathcal{P}\int_{-\infty}^{\infty} \frac{H_{\mathrm{o}}(\omega')}{\omega' - \omega} d\omega'. \tag{4.14}$$

This convolution is used as the Hilbert transform (HT), which is well-known and implemented in many signal processing toolboxes for programming languages. HTs will be denoted with a hat, $\hat{H}(\omega)$. Using this, we can now substitute the HT into equation 4.13:

$$H(\omega) = H_{\mathrm{o}}(\omega) + i\hat{H}_{\mathrm{o}}(\omega). \tag{4.15}$$

Tool (3) tells us that the Fourier transform of $h_{\mathrm{o}}(t)$ is purely imaginary, and so we have an expression for $H(\omega)$ that is complex, but has a relation between two purely real components, with the imaginary component of $H(\omega)$ linking to the purely real component $\hat{H}_{\mathrm{o}}(\omega)$ via the HT. Hence, we have found a link between the real and imaginary parts of $H(\omega)$, using a well known and documented function. Expressing this in terms of susceptibility, we can now easily say:

$$\chi_{\mathrm{I}}(\omega) = \hat{\chi}_{\mathrm{R}}(\omega). \tag{4.16}$$

Hence, we have shown that the HT is mathematically equivalent to the KK relations, and in later sections we will discuss their suitability as a replacement and how it can be applied to an atomic system. However, the HT is still subject to the same limitations as the KK relations, i.e. $\chi(\omega)$ must be complex and analytic in the upper half complex plane.

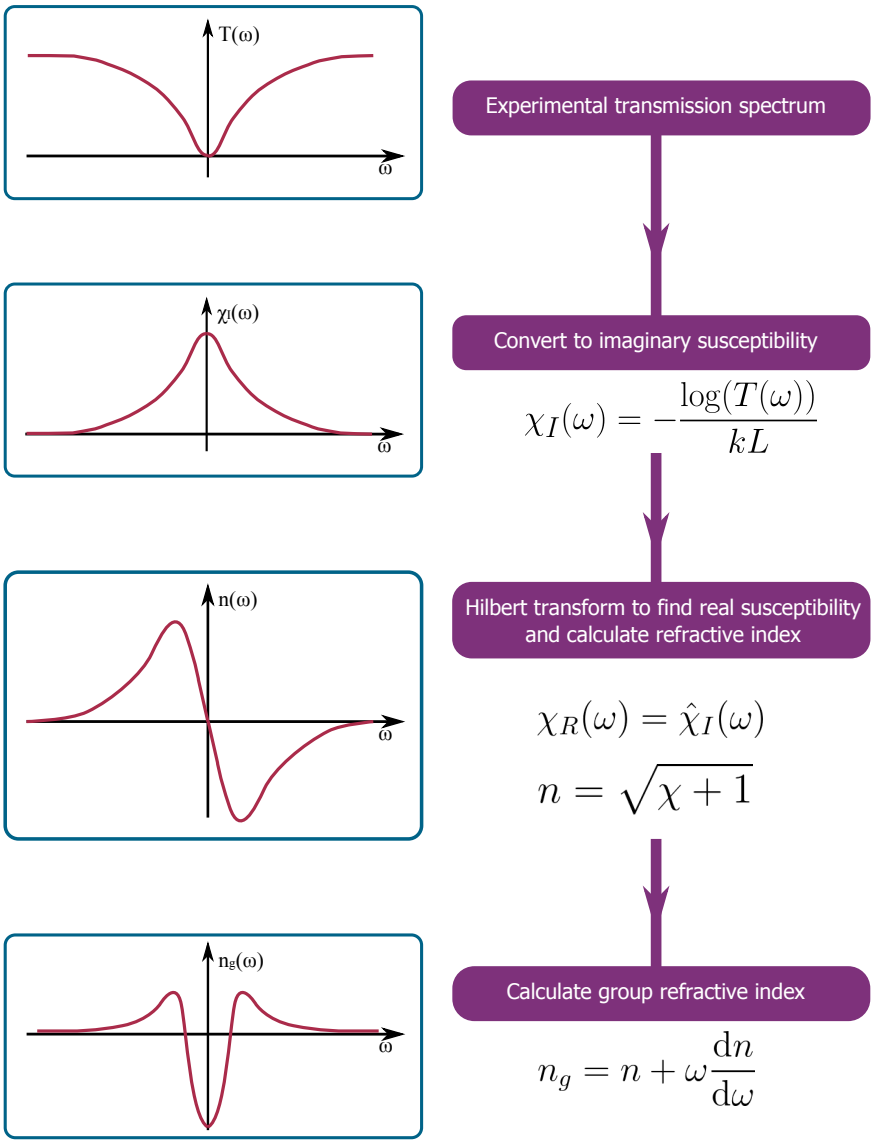

Figure 4.4: Process used to Hilbert transform data. After acquisition, the imaginary susceptibility is calculated using the propagation length and excitation wavelength. The data is then Hilbert transformed and the refractive and group refractive indices can be calculated.

4.2.2 Implementation

The HT is very simple to apply to atomic signals. The process is outlined in Fig. 4.4. A frequency-dependent experimental transmission spectrum, $\mathcal{T}(\omega)$, is taken and converted to the susceptibility using

$$\chi_{\mathrm{I}}(\omega) = -\frac{\ln[\mathcal{T}(\omega)]}{kL}, \tag{4.17}$$

where k is the wavevector ($\lambda/2\pi$) and L is the cell length in the direction of laser propagation. If the susceptibility does not approach zero in the wings of the measured spectrum, it should be linearly padded to approach zero. Padding to zero is required, as otherwise ringing artefacts appear in the wings of transformed spectra. The padding should be linear to avoid a discontinuity in the spectra, which would make the spectrum discontinuous, i.e. non analytic and the KK relations would no longer be valid. It is also advisable to use the padding step to make the length of the data array to be a power of two. Implementations of the HT utilize fast Fourier transforms (FFTs), and hence computation time will be reduced.

The data is then ready to be Hilbert transformed, step 3 on Fig. 4.4, to find the real part of the susceptibility. The refractive index and its derivatives can then be calculated using $n = \sqrt{\chi_{\mathrm{R}} + 1}$.

4.2.3 Advantages of the Hilbert transform

The Hilbert transform has many benefits. Firstly, it is already used in signal processing, and is therefore integrated in signal processing packages for programming languages like Python, MATLAB and C. Consequently, computation times for a HT have been greatly reduced though implementation of FFT based algorithms. To compute Hilbert transformed spectra of experimental data from this thesis, calculation times average 0.5 ms for a few thousand data points. For a simple KK code, the calculation time is 11 s, making the HT 10^4 times faster, allowing for potential *in-situ* monitoring of the refractive index.

Furthermore, as the HT is already available as a function, creation of code is much more accessible and rapid. There are publicly available codes for calculations of KK relations, but these are restricted to specific physical systems.

4.3 Applications in atomic systems

As previously discussed, the HT can be used on atomic absorption spectra to infer the refractive index of spectra. Performing refractive index measurements generally takes much more complex experimental set-ups than transmission spectroscopy and require extra equipment, planning and analysis. Knowledge of the refractive index and the full complex susceptibility can give much more information about the medium being probed, such as pulse propagation speeds [9], nonlinear effects [10] and reflectivity properties (discussed in Chapter 3).

From previous experiments performed in Durham [7], we have a particular interest in pulse propagation speeds. Ultra-thin cells make excellent media for pulse propagation experiments, as the combination of extremely high densities with sharp and narrow transitions result in large group refractive indices are experimentally easy to attain. This results in both very high and low propagation speeds. The group refractive index is derived from the frequency dependent refractive index n and is defined in Eq. 2.29.

Inspecting Eq. 2.29, it can be seen that stronger and narrower transitions result in higher n_g. This results in smaller group propagation velocities v_g, which is calculated from n_g using $v_g = c/n_g$. It is also important to note that group velocities can be either positive or negative, depending on the derivative of the group index. For single-beam transmission spectra from a nanocell it is possible to get large negative n_g and v_g, resulting in a phenomenon called superluminal propagation, where pulses entering the medium exit earlier than expected. Pulse propagation speeds are still lower than c and maintain causality in the medium [7]. For more complex interactions such as electromagnetically induced transparency (EIT), large positive n_g and therefore extremely low v_g can be attained, resulting in slowing or even stopping [9] of light pulses.

However, we must first verify the accuracy of Hilbert transformed spectra. To do this, we compare the refractive index calculated from HT transmission spectra to the expected theoretical refractive index obtained from the model outlined in chapter 3. An experimental spectrum of the Cs D1 line in a 670 nm length nanocell at 220°C was fitted using the model outlined in chapter 3. Each stage is demonstrated in Fig. 4.5, with the associated residuals between theory and experiments plotted beneath each panel. The experimental and theoretical transmission spectra are plotted in Fig. 4.5 (a). Experimental data (pur-

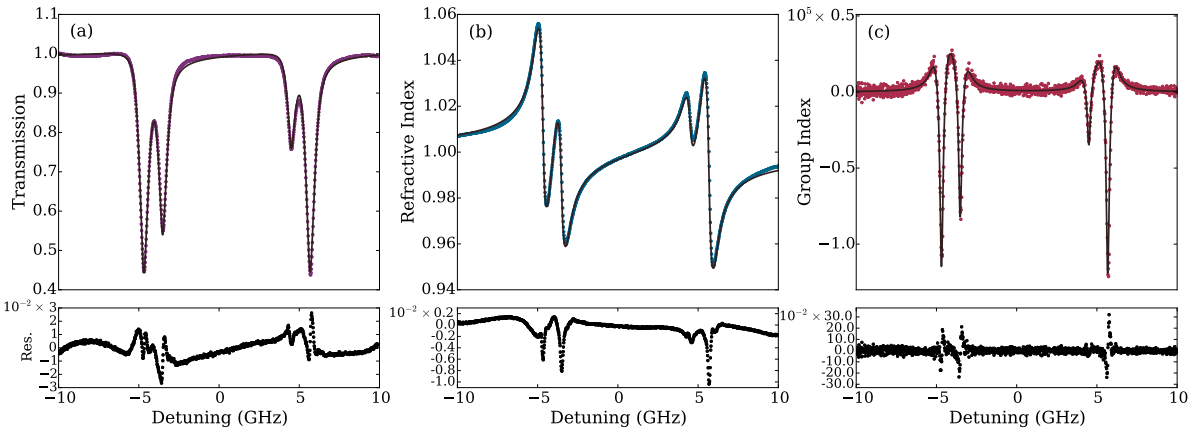

Figure 4.5: Demonstration of Hilbert transforming a spectra taken on the Cs D1 line in a 670 nm length nanocell at 220°C. Panel (a) shows experimental (purple) and theoretical (black) transmission. Panel (b) shows the refractive index, calculated theoretically (black line) and from the Hilbert transformed experimental susceptibility (blue points). In panel (c), the group index is calculated from the experimental data (red points) and theory (black line). Below each panels are the residuals between experiment and theory.

ple points) was taken and fitted to the model (black line), with a normalised root mean squared error (NRMSE) of 1.2%. The model also calculates the theoretical $n(\omega)$, plotted as a black line in panel (b). The experimental data were then converted to a refractive index via HT (blue points, panel (b)). Of note in Panel (b), the maximum group index measured in the experimental dataset shown in Fig. is -(1.21±0.03)×10^5, showing that Cs nanocells could be an excellent medium for superluminal propagation experiments. In panel (c) the group index $n_g(\omega)$ for both theoretical (black line) and HT data (red points) was calculated using Eq. 2.29. Fig. 4.5c shows the resulting theoretical (red line) and hilbert transformed experimental data (black points) $n_g(\omega)$. The agreement between experiment and theory is excellent, with an NRMSE of 2.6%. Hence, extremely reliable experimental spectra can be inferred using the HT.

Now we have confirmed the validity of the HT as a measurement tool, we can apply it further to nanocell spectra. We take experimental transmission spectra from a 442 nm length cell, and examine the temperature dependence of the spectra on the Cs D1 line. We then apply the Hilbert transform to very quickly generate a map of the frequency and temperature dependent $n(\omega)$ and $n_g(\omega)$, plotted in Figs. 4.6 (b) and (c) respectively. Similar experiments were performed over many different lengths, with the results from

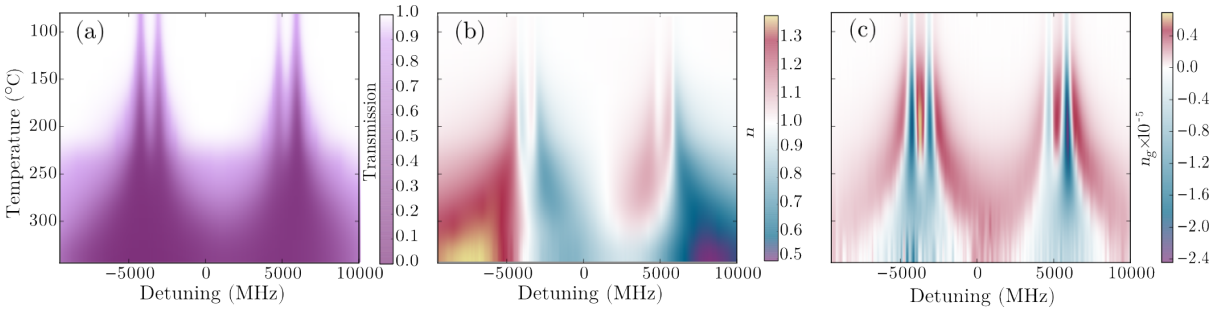

Figure 4.6: Experimental temperature dependence of transmission and inferred refractive index and group refractive index spectra for a 442 nm length nanocell being probed on the Cs D1 line. Panel (a) shows the temperature dependence of the transmission spectra, with each horizontal segment representing a single spectrum like that shown in panel (a) of Fig. 4.5. Panel (b) demonstrates the evolution of the refractive index, with each horizontal slice representing a spectra like that in Fig. 4.5(b). Finally panel (c) demonstrates the temperature dependence of the group refractive index.

L = 442 nm yielding the highest negative n_g of -2.4×10^5. From this it is very easy to identify the region where to attain maximal n_g for pulse propagation experiments.

Demonstrating the applicability of the HT across many area of atomic physics, Fig. 4.7 shows spectra that have had their n_g inferred easily from transmission spectra using the HT. Fig. 4.7 (a) shows transformed spectra from an ultra-cold experiment on the ^{87}Rb D2 transition through a cloud of length 100 μm, where any changes to measurements made involve weeks of careful set-up and realignment, ruling out many other options for refractive index measurements. Hence, applying the HT is excellent for knowledge of the full susceptibility, assisting in understanding even more aspects about this experiment. The group index measured is typical for cold atom experiments but the data here can assist in potential propagation experiments.

Fig. 4.7 (b) shows the resultant spectrum from an EIT experiment in a 2 mm cell at 80°C. The resulting maximal group index is much lower than hoped for, and so this was useful for ruling out the possibility of pulse propagation experiments in this particular set-up.

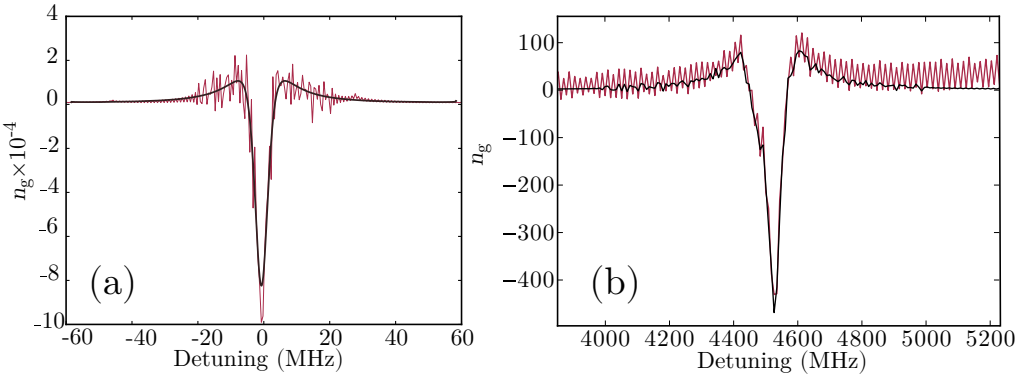

Figure 4.7: Hilbert transformed group refractive index spectrum from (a) an ultra-cold MOT on the ^{87}Rb D2 transition through a cloud of length 100 μm. Panel (b) an EIT experiment on the Rb D2 line in a 2 mm cell at 80°C. Blue lines represent theoretical calculations, and red lines are the Hilbert transformed experimental data. Data courtesy of Paul Huillery and Daniel Whiting

4.4 Conclusion

The Kramers-Kronig relations are an excellent tool for inferring difficult to measure quantities, such as the refractive index. However, implementation of them is challenging and time consuming. Hence, we can use the mathematically equivalent Hilbert transform to perform the same function. Calculation times are decreased by a factor of 10^4 and implementation is much quicker. Resulting spectra for $n(\omega)$ match excellently with theoretical predictions, meaning that the full susceptibility can be easily inferred for many atomic systems.

The HT is easily applicable to many cases, and revolutionises diagnostics of experimental systems. With more information about the complex susceptibility available, decisions about the direction an experiment can take can be made much more expediently. Hence, the Hilbert transform makes an efficient and useful addition to the mathematical toolbox for atom opticians.

Bibliography

[1] R. d. L. Kronig, J. Opt. Soc. Am. **12**, 547 (1926).

[2] H. A. Kramers, Atti. Congr. Internaz. Fisici. Como. (1927).

[3] N. Chiesa and B. Gustavsen, Power Deliv. IEEE Trans. **29**, 1511 (2014).

[4] M. V. Gorkunov and V. E. Dmitrienko, arXiv:1408.4977v1 (2014).

[5] Y. Ohno, Phys. Rev. B **39**, 8209 (1989).

[6] L. J. Wang, A. Kuzmich, and A. Dogariu, Nature **406**, 277 (2000).

[7] J. Keaveney, I. G. Hughes, A. Sargsyan, D. Sarkisyan, and C. S. Adams, Phys. Rev. Lett. **109**, 233001 (2012).

[8] B. Julsgaard, J. Sherson, I. Cirac, J. Fiurasek, and E. S. Polzik, Nature **432**, 482 (2004).

[9] M. Bajcsy, A. S. Zibrov, and M. D. Lukin, Nature **426**, 638 (2003).

[10] R. W. Boyd, *Nonlinear optics* (Academic press, Oxford, 2003), 3rd ed.

[11] G. B. Arfken and H. J. Weber, *Mathematical Methods for Physicists: A Comprehensive Guide* (Elsevier Science, Waltham, 2011).

[12] B. Hirschorn and M. E. Orazem, J. Electrochem. Soc. **156**, 345 (2009).

[13] S. H. Hall and H. L. Heck, *Advanced Signal Integrity for High Speed Digital Designs* (John Wiley and Sons Inc., New Jersey, 2009).

[14] R. Bracewell, *The Fourier Transform and Its Applications*, Electrical engineering series (McGraw Hill, New York, 2000), 3rd ed.

Part II

Nanocell experimentation

Chapter 5

Atom Surface interactions

The tight confinement of the atoms inside nanocells opens up opportunities to study the interaction of atoms with a nearby surface, explored using spectroscopy on both low-lying [1] and higher-lying excited states [2] or EIT spectroscopy of highly-excited Rydberg states [3]. This can be expanded to investigate the temperature dependence of the coefficients describing the strength of the atom-surface (AS) interaction [4] and cases where the usually attractive AS interaction becomes repulsive due to surface resonances [5]. Alternative methods to spectroscopy for probing the AS interaction have also been used, such as scattering or deflection of a beam close to a surface [6–11], atomic beam diffraction [12, 13] and reflection of an ultracold atom cloud from an atomic mirror [14, 15]. Such experiments use detection methods that take place some time after the interaction has occurred.

In this chapter we will describe a methodology that allows us to spectroscopically probe the AS interaction at the time of absorption. We describe an experiment that takes many absorption spectra over a range of temperatures and cell lengths, and uses fitting and error analysis to precisely measure the general form of the AS interaction within the near field. We first detail the methods of data acquisition for absorption spectra, where we utilize single photon counting modules (SPCMs) to acquire absorption spectra over long integration times. The ease of acquisition allows us to take many spectra for a range of cell lengths and temperatures. We then discuss how experimental error is accounted for and utilized to increase the precision of our measurements.

The theory section details the form of the AS interaction in the near field (van der Waals)

regime [16], discussing possible effects that may alter the final form, such as a transition between the near field and retarded (Casimir Polder) [17] regimes; the effect of multiple reflections and the effect of temperature on the interaction. We then give an overview of the fitting procedure performed on the spectra taken. The model we have developed accounts for self broadening [18], Dicke narrowing effects [19] and the AS interaction [16]. The results section presents fitting results for spectra taken on the Rb D2 line and the Cs D1 line, where we find that to describe spectra in the length range investigated herein, the van der Waals description of the AS interaction is optimal. We finally discuss the implication and accuracy of our results including a discussion of the limitations of the technique and perspectives for further work.

5.1 Theory

5.1.1 The atom surface potential

We start from the short description of the AS potential in chapter 3, and expand further to gain a better understanding of the atom-surface (AS) interaction. Physically, we can describe the AS interaction as the result of attraction between a dipole and its reflection in a surface. An induced dipole in the atomic medium induces a shift of charge in a nearby conducting or dielectric surface [16]. This charge redistribution results in a virtual dipole image [17], which has an attractive interaction with the original atomic dipole. This causes a red-shift of the atomic transitions, generally described using $-C_\alpha/r^\alpha$, where α is an exponent that varies between 3 and 4, depending on the interaction regime.

For a more analytical description, we can examine the Landau-Lifshitz interaction potential, or more simply from the full interaction potential between an atom and a nearby surface derived by Casimir and Polder [20]:

$$\mathcal{V}_{\mathrm{AS}} = -\frac{\hbar}{(4\pi)^2\epsilon_0 r^3}\int_0^\infty p(i\omega)\left[1+2\frac{\omega r}{c}+2\left(\frac{\omega r}{c}\right)^2\right]\mathrm{e}^{-2\omega r/c}d\omega, \tag{5.1}$$

where $p(i\omega)$ is the frequency dependent polarisability at an imaginary frequency of the atom and r is the atom-surface separation. This equation can be considered in two limits,

with r tending towards zero and infinity. Looking at the short range case first, we find:

$$\lim_{r\to 0} \mathcal{V}_{AS} = -\frac{\hbar}{(4\pi)^2\epsilon_0 r^3}\int_0^\infty p(i\omega)d\omega. \tag{5.2}$$

The interaction potential is effective when the AS separation is within the near field of the emitter, and is known as the van der Waal (vdW) AS potential. Gathering the prefactors and integral of the polarisability into a coefficient C_3 to describe the distance dependence of the AS interaction at close range, we can reduce the expression to:

$$U_{vdW} = -\frac{C_3}{r^3}, \tag{5.3}$$

where

$$C_3 = -\frac{\hbar}{(4\pi)^2\epsilon_0}\int_0^\infty p(i\omega)d\omega. \tag{5.4}$$

The C_3 coefficient has a dependence on the atomic polarisability, meaning that it is dependent on the strength of the electronic transition studied. When measuring the AS shift on an optical transition, the effective coupling coefficient is proportional to the strength of the probed transition. For this reason, we distinguish between coupling coefficients using a superscript denoting the transition, e.g. $C_3^{5S_{1/2}}$ for the ^{85}Rb $5S_{1/2}$ F_g = 2,3 ground states and $C_3^{5S_{1/2}\to 5P_{3/2}}$ for measurements taken on the ^{85}Rb $5S_{1/2}$ F_g = 2,3 to ^{85}Rb $5P_{3/2}$ F_e = 1,2,3,4 transition.

In a vapour cell, both walls contribute to this potential across the cell, meaning that the potential experienced by atoms inside a cell of length L is:

$$U_{vdW} = -\left(\frac{C_3}{r^3} + \frac{C_3}{L-r^3}\right). \tag{5.5}$$

This potential is plotted in Fig. 5.1a. As an inset to the panel, the change to the potential due to multiple AS reflections is plotted. These alterations are negligible, on the order of 100 kHz and are smaller than the range of shifts our experiment is sensitive to. They are excluded in future calculations.

Returning to the full interaction potential, we can also study what happens at longer length limits. When the inter-atomic separation r is sufficiently long, transit time of exchange photons mediating the interaction between the atom and surface must be accounted for. This results in a retarded potential which can be expressed by taking the limits of the CP potential to infinity [20]:

$$\lim_{r\to\infty} \mathcal{V}_{AS} = -\frac{3\hbar c p(0)}{2^5\pi^2\epsilon_0 r^4}. \tag{5.6}$$

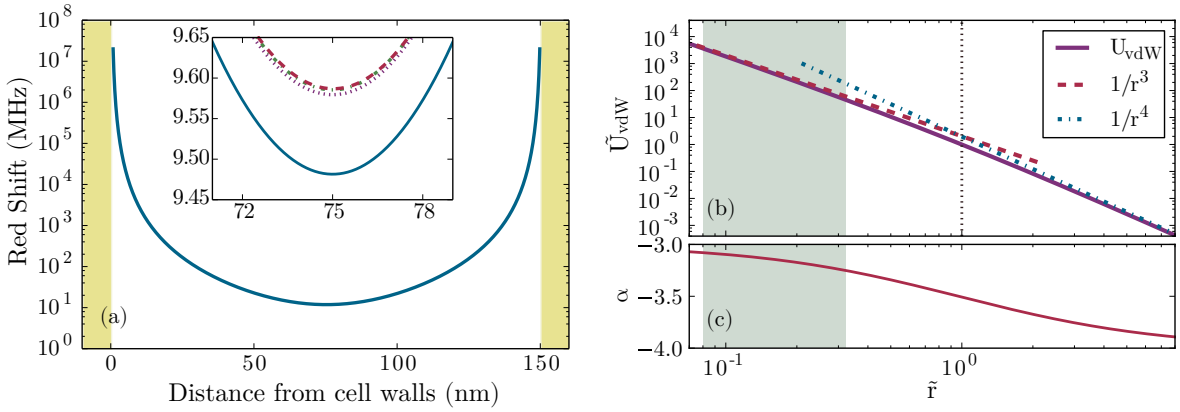

Figure 5.1: (a) The position-dependent red shift from the van der Waal $1/r^3$ AS potential. Inset: The effect of multiple reflections contributing to the vdW AS interaction. Plotted are shifts caused by accounting for a single (blue line); two (purple dotted line); three (red dashed) and four reflections (green dot dashed line). Panel (b) shows the length-dependent variation of AS potential (purple line) taken from equation (45) in [21], highlighting the transition between the short range $1/r^3$ vdW (red dashed line) and long range $1/r^4$ CP (blue dot dashed line) regimes. Most of the data come from the region highlighted in grey (length range of 10-40 nm). $\tilde{U}_{\text{vdW}}$ is scaled such that $\tilde{U}_{\text{vdW}} = 1$ at $\tilde{r} = \lambda/2\pi$. The length scale $\tilde{r}$ is scaled in units of $\lambda/2\pi$. In panel (c), the variation of the exponent α of the atom-surface attraction in the form $1/r^{\alpha}$ between the vdW and CP regime is shown, again with the length range the experiment is sensitive to highlighted in grey.

Again, gathering prefactors this can be expressed as a simple distance dependent potential with atomic polarization dependent coupling coefficient C_4:

$$\mathcal{V}_{CP} = -\frac{C_4}{r^4}. \tag{5.7}$$

This potential is known as the Casimir-Polder potential. The crossover point between the $1/r^3$ vdW potential and the $1/r^4$ potential is gradual, occurring at a length separation around the reduced transition wavelength $\lambda/2\pi$. The smooth transition between the vdW (near field) and CP regime [22] has been the subject of many studies [17, 21, 23], with estimates for the onset of the transition ranging from lengths of $\lambda/2\pi$ [21] to 0.03λ [24]. To identify the length regime our work covers, we inspect the full form of the AS interaction including both CP and vdW forms [21]:

$$U_{\text{AS}} = -\frac{\hbar^2}{2M}\left[\frac{r^3}{\beta_3} + \frac{r^4}{\beta_4}\right]^{-1}, \tag{5.8}$$

where M is the atomic mass and $\beta_{3,4}$ are length parameters related to the strength of the vdW/CP potential and are taken from [21]. Values taken are for ground state Rb ($5S_{1/2}$), unlike the transitions we investigate experimentally, which probe the difference in interaction coefficients between the ground ($5S_{1/2}$) and excited ($5P_{3/2}$) states. The potential is plotted in Fig. 5.1b. We use this comparison as an indicator for which interaction regime we expect our spectra to lie in. We expect that the ground-state case is a worse case scenario as we are further into the C_3 region for the excited state as the transition wavelengths to nearby states are longer. Fig. 5.1b shows the resulting potential for the ground state (purple line). $\tilde{U}_{\mathrm{vdW}}$ is scaled such that $\tilde{U}_{\mathrm{vdW}} = 1$ at $\tilde{r} = \lambda/2\pi$. The length scale $\tilde{r}$ is scaled in units of $\lambda/2\pi$. Both the CP and vdW interactions are plotted for comparison (blue dot-dashed and red dotted lines respectively). The length range that most of our data are produced for is shown as a grey area on the plot. At short lengths, there is good agreement with a $1/r^3$ vdW potential (red dashed line). At longer lengths there is reasonable agreement with a $1/r^4$ CP potential (blue dot dashed line). The transitional region has no strong agreement with either potential, but lies outside the effective range of our experiment and so should have no impact on final results.

In Fig. 5.1c we plot the length dependence of the exponent α of the AS interaction. Figs. 5.1b and c demonstrate that our experiment is sensitive to the shorter range van der Waals interaction regime. The average exponent in the length range $L = 10 - 40$ nm is $\alpha = 3.16$.

There are a range of factors that could potentially interfere with measurements of the AS interaction. The surface quality has several effects on the interaction. Equations quoted herein are effective for a perfectly conducting surface, but in reality there will be some attenuation of the interaction by the surface. This is accounted for by multiplying the C_3 coefficient with the factor $(\epsilon_s - 1)/(\epsilon_s + 1)$, where ϵ_s is the surface permittivity. For the sapphire surfaces used in this experiment, we use $\epsilon_s = 3.2$, resulting in an reduction of the C_3 coefficient by a factor of 0.52.

Surface quality also affects the interaction, with patch charges created by adsorbed alkali-metal on the cell surface interfering with the attenuation coefficient. Additionally, the surface roughness of the cell's interior surfaces can be a concern. In the sapphire nanocells, the surface quality has an rms roughness of 3 nm. However, atoms being studied are moving at thermal velocities of a few hundred ms^{-1} and therefore experience a time-

averaged potential of the AS separation, and so the surface roughness can be neglected in calculations.

The coupling coefficient C_3 also varies with temperature [4, 22]. However at short ranges the thermal dependence of C_3 is dominated by surface excitations [4], where the incident light also excites surface plasmon polaritons. This is not the case for the transitions investigated herein, as they do not concur with the frequencies of any surface plasmon excitations of sapphire [25]. There is still some temperature variation of the C_3 coefficient, this is on the order of 1% over the temperature ranges investigated herein and is hence negligible in the scope of this experiment [26].

5.2 Experimental methods

5.2.1 Data Acquisition

The first question to ask is how to probe the interaction. Transmission spectroscopy is not a good candidate, as high temperatures are required to obtain a sufficient signal. In high temperature regimes, exceeding 150°C, self broadening will smear out the asymmetry caused by the AS potential [18]. At lower temperatures where lines are sharp due to extreme Dicke narrowing, the change in transmission $\Delta\mathcal{T}$ is on the order of 0.5%, where any measurable signal will be lost in experimental noise sources, making transmission spectroscopy impractical. Due to this, we study the off-axis scattered light from a laser scanning over the resonant frequency of the state being probed.

Using off-axis detection of scattered light with single-photon counters, extremely high sensitivity spectra can be taken from shorter cell lengths at lower temperatures. This increases our experimental resolution as the extreme Dicke narrowing of the lines at low temperatures results in spectra with all hyperfine states resolved. Furthermore, all coherent effects based on summing of the electric fields of the incident beam and the atomic response, *i.e.* the collapse and revival of Dicke narrowing and the mixing of selective reflection and transmission signals can be ignored, simplifying fitting of spectra.

Absorption spectra were taken on the Rb D2 line. This was used because the large strength of the transition result in a strong AS interaction. Data were also taken on the Cs D1 line, used for its large 9 GHz ground state splitting and 1.2 GHz excited

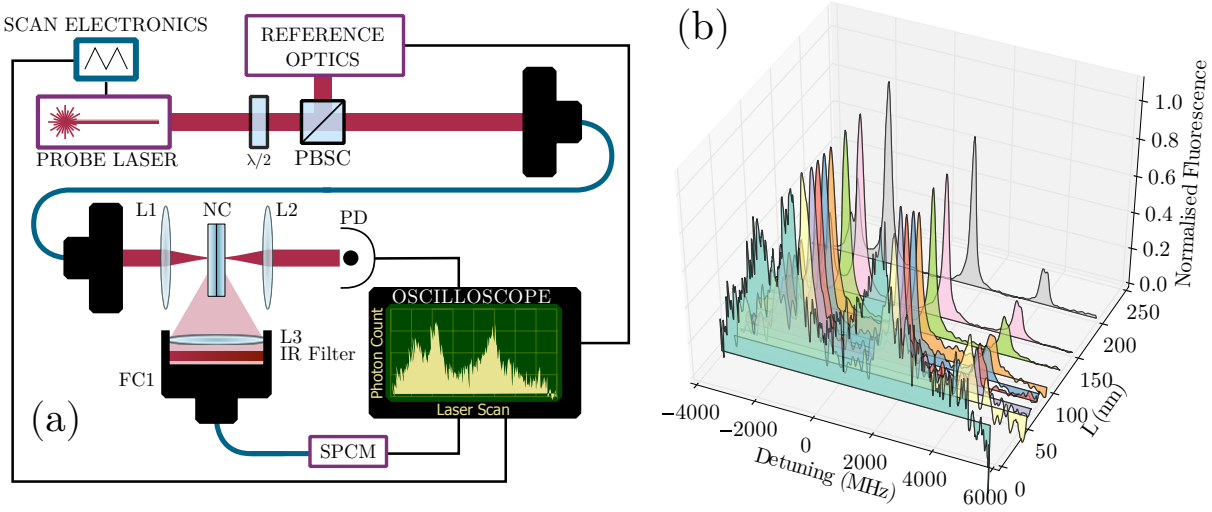

Figure 5.2: (a) Experimental schematic used to measure spectra of off-axis scattered light from the nanocell. (b) Waterfall figure demonstrating the evolution of acquired spectra with length.

state splitting, much larger than the Doppler width. All spectra were taken within the weak-probe limit [27].

The experimental layout is shown in Fig. 5.2a. Some of the light is sent though reference optics - a 7.5 cm reference vapour cell and a Fabry-Perot etalon, which are collected concurrently with the scattered light spectra to calibrate the laser frequency. The light is then sent down an optical fiber to the nanocell section of the experiment. The light is focussed in the centre of the nanocell by lens L1 to a spot size with a $1/e^2$ radius of 20 μm, then is recollimated by lens L2. Transmission data are recorded on a photodiode (PD). Off-axis scattered light is collected by lens L3, with background light and thermal photons from the cell heater are suppressed by an infrared filter. The signal is sent to a single-photon counting module (SPCM) via a fiber collimator, FC3. The counts are processed by a LeCroy Waverunner 610Zi oscilloscope into a histogram of arrival times corresponding to the frequency of the laser scan, according to the method outlined in [28].

The laser scan time is 50 ms, and individual bins in the histogram are 5 μs long, corresponding to a bin width of 2 MHz when the spectra have been frequency calibrated. Hence the detection method is sensitive to the frequency at which a photon was absorbed, meaning AS shifts measured map directly onto a particular AS separation for that frequency. This renders our method insensitive to any transient effects such as motion between the

time of absorption and fluorescence events or interruption of fluorescence decay by wall collisions [29]. Single scans return only a few photon counts, so long integration times (15 minutes to several hours) are used to build up statistics of arrival times, allowing for sensitive detection of spectra.

Fig. 5.2b shows the evolution of acquired spectra with increasing length. The dataset demonstrates very well how the signal develops with length, with the signal changing from extremely narrowed well defined Dicke narrowed peaks at longer lengths, to a broadened asymmetric signal at the shortest lengths. Signal-to-noise ratios (SNRs) are much worse at shorter lengths, as the signal is much weaker as there are fewer emitting atoms present. All spectra are normalised to have a peak count number of 1. These spectra will then be subjected to our fitting and analysis process outlined in the next subsection.

5.2.2 Extracting AS parameters

The next method to be determined is how to extract meaningful results about the AS interaction from the spectra obtained. It is tempting to simply take spectra and measure shifts of excited state transitions, but this can be problematic for several reasons. Firstly, despite the use of extremely sensitive data acquisition methods, when the cell length approaches the lower limit of detection, around 40 nm, signal to noise ratios (SNR) are very low, making peak detection challenging, with usual methods for removing noise such as smoothing and binning changing the locations of the shift, rendering them ineffective for determining an excited state shift.

Additionally, spectra will broaden into each other, altering the shift location. Potential sources include self broadening, the Doppler background of Dicke narrowing and the AS interaction itself. Shifts from the AS interaction can reach several GHz, overlapping with nearby transitions, altering the shift location. This can be evidenced by examining the length dependence of the shift of the ^{85}Rb $5S_{1/2}F_g = 2$ line to the ^{85}Rb $5P_{3/2}$ $F_e = 1,2,3$ transition for a calculated theoretical line-shape using realistic experimental parameters. The theory line-shape is generated using a pure $1/r^3$ potential from the model outlined in chapters 3. The peak location is then identified and plotted. We compare the resultant length dependent peak shifts to the shifts expected from only an AS shift. The results of this simulation are shown in Fig. 5.3. If the shift follows the AS potential, we would expect that on a logarithmic plot to see shifts linear with length with a gradient of 3, plotted for

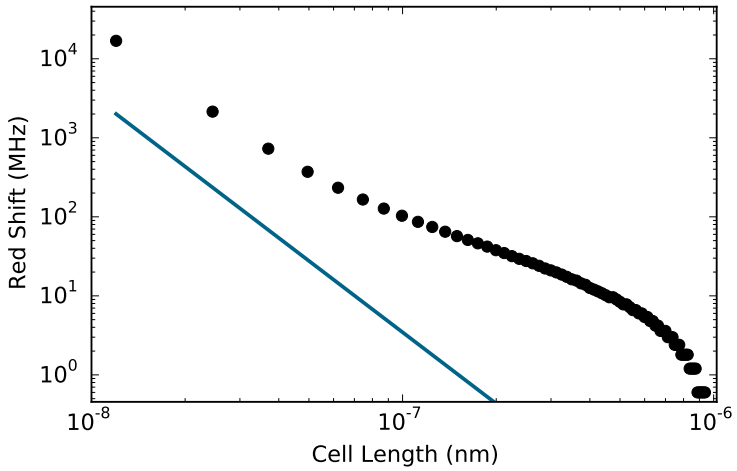

Figure 5.3: Length dependence of the shift of the ^{85}Rb $5S_{1/2}F_g = 2$ line to the ^{85}Rb $5P_{3/2}$ F_e = 1,2,3 transition (black points), taken from theoretical spectra generated with a $1/r^3$ potential. The resulting shifts do not follow a $1/r^3$ potential, plotted for comparison as a blue line.

reference on the figure as a blue line. However, Fig. 5.3 clearly demonstrates that this is not the case. There is no pure power law in the shifts, with a magnitude consistently larger than expected. Hence, direct measurement of shifts of these spectra will not yield meaningful results that directly correspond to information about AS induced shifts, as extracting a power law adjusted for all shifts and broadenings would introduce a large amount of guesswork and error into the results.

We therefore fit the entire spectrum, accounting for self broadening, Dicke narrowing and additional homogeneous broadenings, using the model of the frequency dependent atomic susceptibility of the vapour $\chi(\Delta)$ outlined in chapters 2 and 3. However, we exclude the final 2 stages of fitting, where absorption is converted to transmission and the mixing of selective reflection and transmission signals are calculated as these are not observed in off-axis scattered fluorescence. The modified process is outlined in Fig. 5.4. Each step is illustrated with an example line shape with the most relevant equation displayed beneath it. For comparison, the state of the line shape after (before) each step is shown in red (grey). Included in the fit parameters are the AS coefficient, C_α, and the exponent of the power law r^α, these will then be translated to a final measurement of these paramters for the vapour by averaging fit results by their reduced chi-squared parameter, discussed in the next subsection.

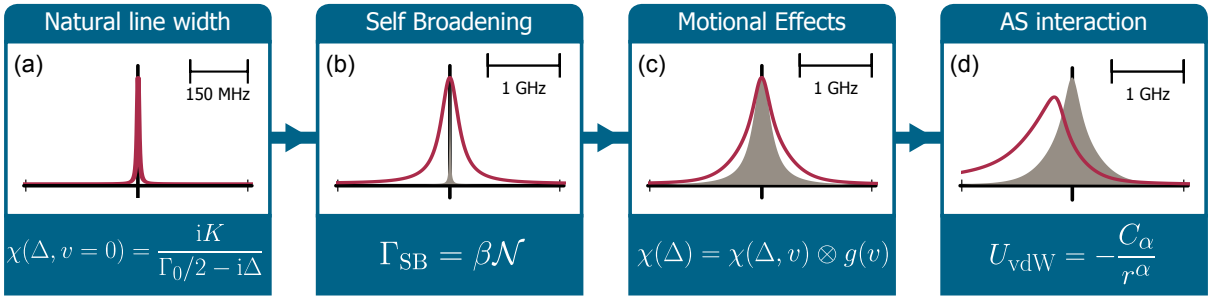

Figure 5.4: Illustration of the various contributing factors to the measured line-shapes. From left to right, the line-shape after each effect (red line) is added to the previous line shape (shown as grey area). Each step is accompanied by the most relevant equation used to describe the changes in the line shape. The spectra are generated for a cell length of 60 nm and temperature of 200°C. Panel (a) shows the natural line shape at zero velocity, $\chi(\Delta, v = 0)$. In panel (b), effects caused by density (N) dependent self (collisional) broadening are added to the widths of each transition. This results in a large Lorentzian broadening of the line. Panel (c) shows velocity-dependent effects on the line shape. The Doppler-broadened line shape $\chi(\Delta, v_z)$ is convolved with a bimodal velocity distribution $g(v)$ that represents the stronger contribution of 'slow' atoms to the line shape. The effect is a small additional width. In panel (d) the AS interaction is accounted for by adding a shift modeled using the AS potential U_{vdW} for the ground to excited state acting over the entire cell length. The change on the line shape is dramatic for short cell lengths, shifting the peak and causing a long red tail.

In panel (d) of Fig. 5.4, we account for the AS interaction by calculating the position-dependent AS shift $\Delta_{\mathrm{AS}}(r)$ across the entire cell length L:

$$\Delta_{\mathrm{AS}}(r) = -\left[\frac{C_\alpha}{r^\alpha} + \frac{C_\alpha}{(L-r)^\alpha}\right], \tag{5.9}$$

where C_α is a coupling coefficient describing the strength of the AS interaction, and α is an exponent describing the power law of the AS interaction. The two terms in Eq. 5.9 simply sum the AS interaction from both cell walls. Both C_α and α are used as floating fit parameters to determine the form of the AS power law. Δ_{AS} is then weighted by the position-dependent interaction times, discussed in Chapter 3. The result is an asymmetric line shape representing shifts across the entire cell weighted by interaction times. This line shape is then convolved with the Dicke narrowed line shape to give the final result of the fitting function.

Additional broadening effects that are not currently modelled are accounted for by adding an excess broadening parameter Γ_{ex} into the fit, which is added onto the self broadening expression, resulting in a total additional broadening of $\Gamma_{\mathrm{tot}} = \Gamma_{\mathrm{SB}} + \Gamma_{\mathrm{ex}}$. We suspect these additional broadenings may be caused by radiation trapping within the nanocell, a future avenue of investigation.

To summarize, the model takes the natural line shape, includes the well-known self broadening, and a fitted additional broadening, Γ_{ex}. We then convolve the line shape with a phenomenological bimodal velocity distribution to account for Dicke narrowing, with a fitted parameter a representing the strength of the contribution of traditional Maxwellian velocity classes. The last step is to convolve with a line shape generated using the AS interaction, fitting for the AS coefficient for the excited state transition $C_\alpha^{5S_{1/2}\to 5P_{3/2}}$ and the exponent of the interaction α. These fit results are then averaged to find a measurement of $C_\alpha^{5S_{1/2}\to 5P_{3/2}}$ and α.

5.2.3 Error analysis

As results are calculated using fitting, we must take a careful approach with error analysis, ensuring that we use appropriate measures of goodness of fit. Furthermore, signals collected can be very weak, with some scattered light spectra contributing just 4% of the total signal for data where the signal is very weak, requiring long interrogation times and

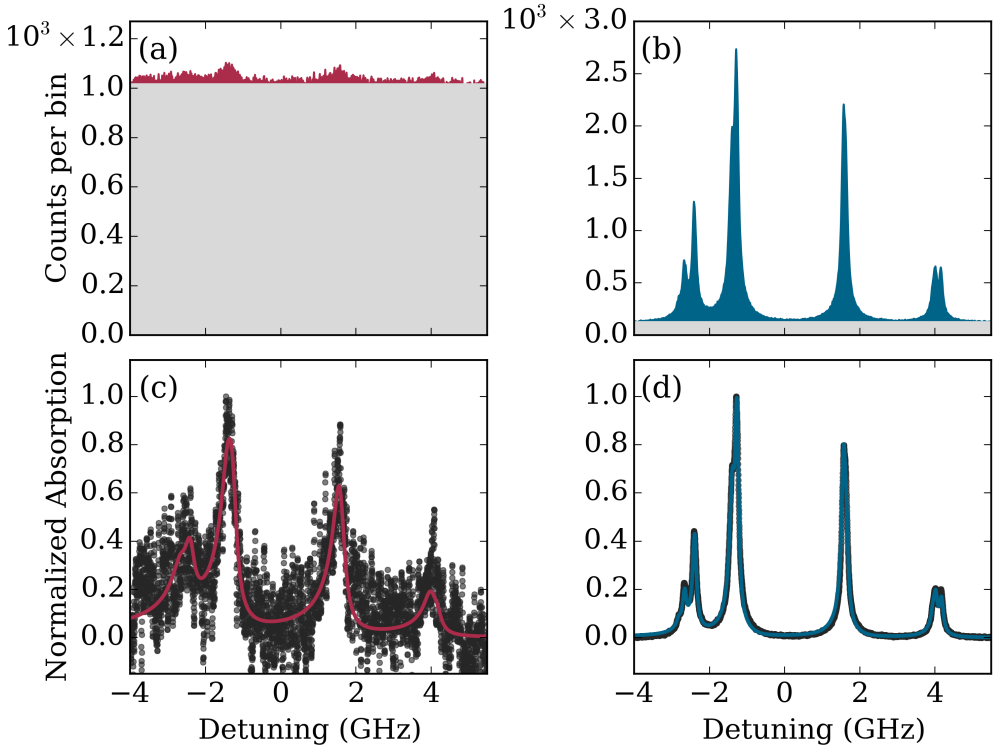

Figure 5.5: Off-axis scattered photons measured using an excitation laser scanned across the Rb D2 resonance. The figure shows a comparison of raw data (shaded grey areas, panels (a) and (b)) to processed data (black points, panels (c) and (d)) on the Rb D2 line at a temperature of 125°C for (a,c) 60 nm and (b,d) 250 nm cell lengths. Background counts are shown in grey and the atomic signal highlighted in red and blue for lengths of 60 and 250 nm respectively. Panel (a): The atomic signal, highlighted in red, is small in comparison to the background count because the interrogation volume is so small that there are relatively few atoms contributing to the signal, necessitating a long interrogation time that results in large background counts. Therefore, the error is dominated by the error of the background count. Panel (b): The atomic signal is the main component of the raw signal because far more atoms are contributing to the signal, resulting in much smaller relative error compared to panel (a). Panel (c): The fit for $L = 60$ nm (red line) has a 'goodness of fit' parameter, Υ, of 0.1. The small value of Υ is caused by the large background counts involved for such small cell lengths, illustrated in panel (a). Panel (b): the fit for $L = 250$ nm (blue line) has a reduced chi squared Υ [30] of 1.7, indicating an excellent fit. The background photon count is much smaller than for $L = 60$ nm, resulting in lower relative error and an Υ closer to 1.

resulting in a large accumulation of background signal. The background signal consists of a frequency independent background; random noise evenly distributed across the entire spectrum, which comes from ambient light sources and some scattered light from the incident laser.

The errors in the atomic signal, $A(\omega)$, are calculated by taking the frequency-dependent raw spectrum $R(\omega)$ and subtracting the background count B.

$$A(\omega) = R(\omega) - B. \tag{5.10}$$

For data acquisition, the errors in the atomic signal (s_{A}) are Poissonian counting statistics; each data point in the raw counts $R(\omega)$, with a number of counts N_{count}, has an associated error of $\sqrt{N_{\mathrm{count}}}$ [30]. The errors can be calculated as:

$$s_{\mathrm{A}} = \sqrt{s_{\mathrm{R}}^2 + s_{\mathrm{B}}^2}, \tag{5.11}$$

with s_{R} and s_{B} as the errors in the raw and background signals, respectively. The relative error bars are very small for spectra similar to Fig. 5.5b because $A(\omega)$ is large and B is small. However for spectra with low signal-to-background ratio like that in Fig. 5.5a, i.e. $B \gg A(\omega)$, the error of the raw signal is roughly equal to the error of the background signal, $s_{\mathrm{R}} \approx s_{\mathrm{B}}$. Hence, s_{A} can be approximated as $s_{\mathrm{A}} \approx \sqrt{2s_{\mathrm{B}}^2}$. This results in large relative error for shorter cell lengths when compared to the error bars for longer cells with better signal-to-background ratios.

We fit the spectra using the Marquardt-Levenburg method [30] to minimise the sum of the squares of the difference between theory and experiment, normalized by the error bar. For errors in fitted parameters for an individual spectrum, we use the standard deviations of the mean calculated by the fitting routine. An example of the fitted results is shown in panels (c) and (d) of Fig. 5.5. Zero detuning on each plots is the weighted centre of the transitions probed.

For the analysis performed on Rb spectra, we take an average of the fitted parameters weighted by the reduced χ-squared of the fit. The reduced χ-squared is a goodness of fit measurement, represented here by Υ to avoid confusion with the vapor susceptibility. Υ is calculated as

$$\Upsilon = \frac{1}{\nu} \sum_{\omega} \frac{[A(\omega) - T(\omega)]^2}{s_A^2}, \tag{5.12}$$

where $A(\omega)$ is the observed frequency-dependent atomic signal, $T(\omega)$ is the theoretical signal and ν is the degrees of freedom, calculated as $\nu = N_{\text{points}} - N_{\text{param}}$, where N_{points} is the length of the data set and N_{param} is the number of fitted parameters.

Values for Υ of our fitted spectra vary between 0.1 to over 1000. Generally, a Υ close to 1 indicates a good fit, and any value much lower than 1 indicates overestimated errors [30]. However, this is not the case in our experiment; the smaller values of Υ are caused by the huge background counts for shorter cell lengths, illustrated in Figs. 5.5a and b. The small values of Υ can be accounted for by considering the large relative error margins that arise when the atomic signal is small resulting in a higher proportion of the fitted spectra within the error margins of the atomic signal. Consequently, the resulting Υ is much less than 1, but still a valid measure of goodness of fit.

5.2.4 Simulated annealing

To test the robustness of our fits, we fit sample spectra from our data set using a simulated annealing (SA) fitting algorithm [31] instead of the Marquardt-Levenberg (ML) method. The SA fitting algorithm was adapted from the code in [32] to use our model of the absorption spectra from the previous section. To identify the best fit the SA algorithm tries fit parameters and calculates a cost value, calculated as the absolute value of the sum of the theoretical fit subtracted from the dataset. The parameters are varied such that a global optimal fit is found as opposed to a local optimal fit which can returned by a ML fit. The SA algorithm was further adapted to return attempted fit parameters along with the cost value returned for that attempt. However, SA fits are extremely time consuming, with calculation times for a rigorous analysis taking a full day. Hence SA analysis is restricted to only a few datasets to confirm validity of our results.

Fig. 5.6 shows the resulting cost values for $C_\alpha^{5S_{1/2}\to 5P_{3/2}}$, panel (a), and α, panel (b). Final fitted values from the SA fit, $C_\alpha^{5S_{1/2}\to 5P_{3/2}} = 1.1$ kHz μm^3 and $\alpha = 2.99$ are plotted as dashed red lines on their respective plots. Panel (a) shows that there is very little variation in the lowest cost value for $C_\alpha^{5S_{1/2}\to 5P_{3/2}}$ over the range of values explored by the SA fitting algorithm, indicating a larger error bar. Conversely, there is a clear region of lowest cost for attempted values of α, centred around the fitted value of $\alpha = 2.99$, in agreement with previous analysis.

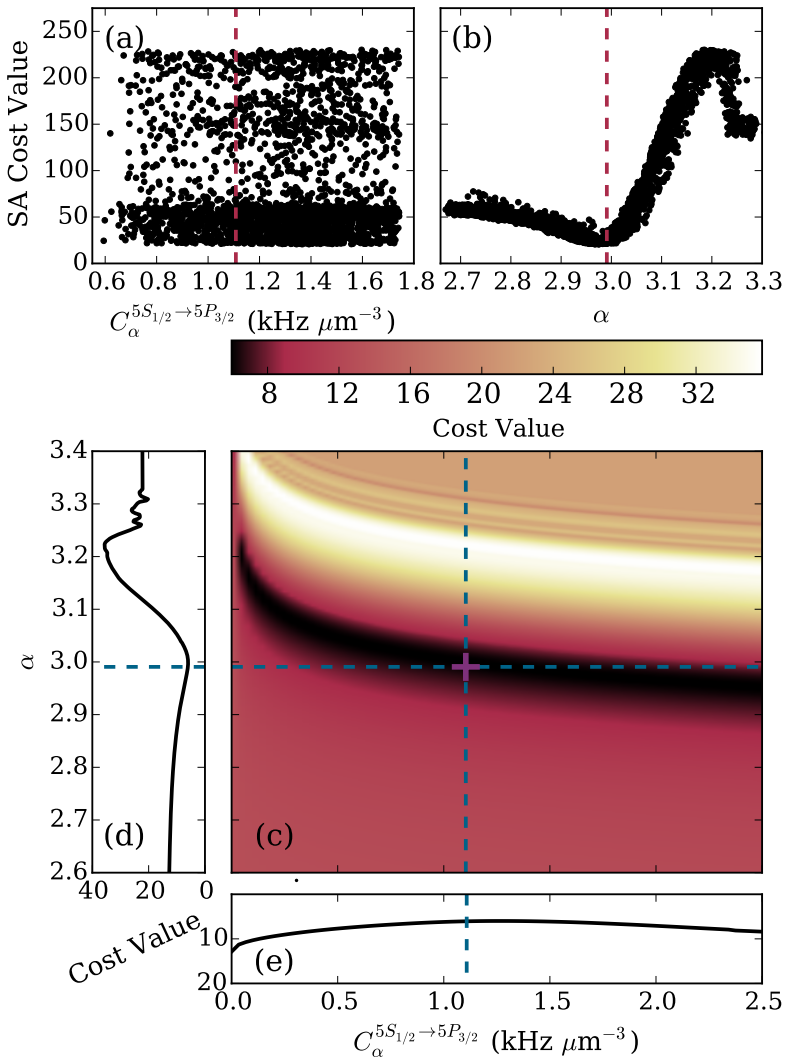

Figure 5.6: Analysis of simulated annealing (SA) fits for a cell of length 80 nm, temperature 125°C. (a) Cost values of attempted C_α coefficients tried by the simulated annealing fitting algorithm, with the final fitted value plotted as a red dashed line. There is no clear best value of C_α over the range explored. (b) Cost values of exponent α explored by the SA fitting algorithm. Here, there is a clear region between $\alpha = 2.9$ and 3.1 where the fit is best. The fitted value found by the SA fitting algorithm is shown as a red dashed line. (c) Parameter space showing cost value across an array of C_α and α with the rest of the fit parameters kept constant. Panels (d) and (e) show the cost values along the fit parameters found by the SA fitting algorithm, highlighting that the region where α is the best fit parameter is very narrow, whereas there is smaller relative variation in the cost value for C_α.

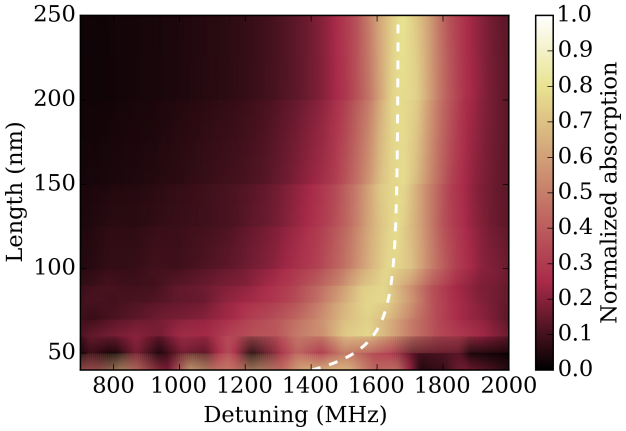

Figure 5.7: An accumulation of many spectra for different cell lengths. Here we highlight the length dependence of the absorption spectra on the ^{85}Rb $5S_{1/2}F_g = 2$ line to the ^{85}Rb $5P_{3/2}$ $F_e = 1,2,3$ excited state for T = 150°C. The expected AS shift for $r_{\max} = L/2$ is plotted as a white dashed line, using $\Delta_{\mathrm{AS}} = -C_\alpha^{5S_{1/2}\to 5P_{3/2}}/r_{\max}^3$. This data set clearly demonstrates the length dependence of the red tail caused by the AS interaction. However in Rb, the red tail and shifts are not appreciable until cell lengths shorter than 80 nm, i.e. maximum AS separations of 40 nm. Hence, fits performed will not be sensitive to the AS interaction outside of this length range.

To explore the possible best fit values, we generated a theoretical parameter space. We kept all parameters aside from α and $C_\alpha^{5S_{1/2}\to 5P_{3/2}}$ constant, then calculated the cost values across an array of $C_\alpha^{5S_{1/2}\to 5P_{3/2}}$ and α. The resulting parameter space is shown in Fig. 5.6c. We also show the variation in the cost value along the axes defined by the fitted SA parameters (purple cross), for α in Fig. 5.6d and for $C_\alpha^{5S_{1/2}\to 5P_{3/2}}$ in Fig. 5.6e. The selections are highlighted on panel (c) as blue dashed lines. Again, the region of lowest cost value for α is much narrower than for $C_\alpha^{5S_{1/2}\to 5P_{3/2}}$, showing that this method of fitting spectra is more effective in identifying the exponent, α, of the AS interaction. However, the larger uncertainty in best cost value for $C_\alpha^{5S_{1/2}\to 5P_{3/2}}$ in the parameter space shows that this method is less suited to find an accurate value of $C_\alpha^{5S_{1/2}\to 5P_{3/2}}$.

5.3 Experimental results

5.3.1 Rubidium D2 line

Spectra were taken over a length range of $L = 40 - 250$ nm at temperatures $T = 125$, 150, 175 and 200 °C. The relative ease of acquisition of spectra also allows us to take many readings over long integration times, increasing the precision of the experiment.

A colour map showing the length dependence of the AS induced shifts is shown in Fig. 5.7. Data are on the ^{85}Rb $5S_{1/2}F_g = 2$ line to the ^{85}Rb $5P_{3/2}$ $F_e = 1,2,3$ line of the Rb D2 resonance taken at $T = 150$°C. Each horizontal slice shows an experimental spectrum like those in Figs. 5.5c and d, i.e. with background counts subtracted, then normalized such that 1 on the colour scale is the peak of the ^{85}Rb $5S_{1/2}F_g = 2$ to the ^{85}Rb $5P_{3/2}F_e = 1, 2, 3$ excited state transitions. The figure demonstrates a clear length dependence of the asymmetric red tail, as expected for the AS interaction. The expected AS shift for atoms in the centre of the cell is plotted as a white dashed line. The actual peak shift does not follow exactly the expected $1/r^3$ form because the asymmetric red tail and self broadening from nearby transitions skew the peak location.

At long lengths ($L > \lambda/4$), shifts due to the AS interaction on the ground state transitions are very small - on the order of a few MHz. The impact on the line shape is minimal until shorter cell lengths. For the Rb D2 line the asymmetric tail is not appreciable until cell lengths less than 80 nm as evidenced in Fig. 5.7. The asymmetric red shift characteristic of the AS interaction is not fully evident until the cell length is below 80 nm with maximum AS separation $r_{\max} = 40$ nm. This means our fits are most effective in the length region $r_{\max} = 10$ - 40 nm, where there is a sufficiently large red tail to fit to.

After background-count subtraction and normalization, spectra are fitted using the model outlined in the previous section. Examples of fit results on the Rb D2 line for a temperature T = 125°C are shown in Figs. 5.5c and d. They show experimental spectra (black points) processed from the raw data shown in Figs. 5.5a and b, fits performed for cell lengths of 60 nm (red line) and 250 nm (blue line).

Upon visual inspection, both spectra have excellent fits. The fit for $L = 250$ nm in panel (b) has an Υ of 1.7 indicating an excellent fit, although with no AS induced shifts

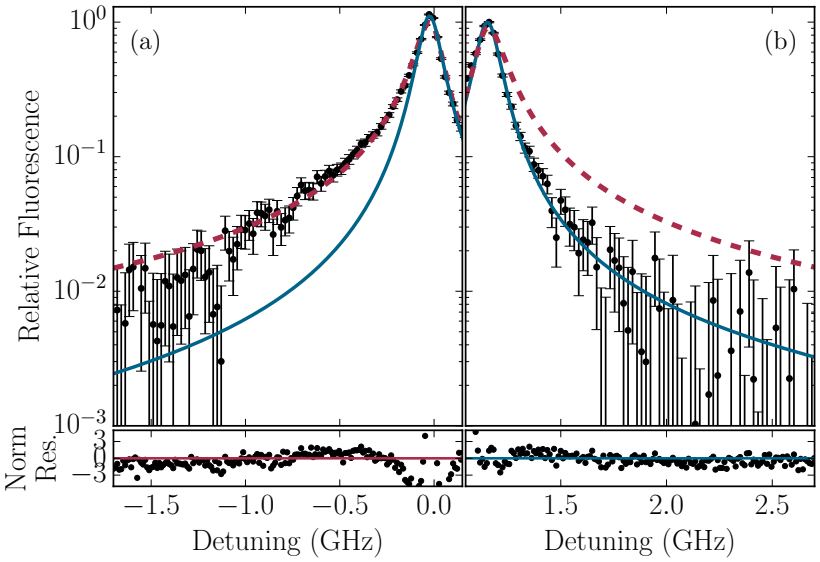

Figure 5.8: Comparison of the red wing of the Cs $6S_{1/2}F_g = 3$ to $6P_{1/2}F_e = 4$ transition (a), and the blue wing of the Cs Cs $6S_{1/2}F_g = 3$ to $6P_{1/2}F_g = 3$ to $6P_{1/2}F_e = 3$ transition (b). Zero detuning is the resonance frequency of the line. There is a remarkable difference between the two wings, showing what a profound impact the AS interaction has on the line shape. The data (black points) are compared to the red wing as fitted by our model (dashed red line, mirrored in panel (b) for comparative purposes) and a Lorentzian fit to the blue wing (blue line). A Lorentzian fit is sufficient to model the blue wing, because Doppler broadening is suppressed by Dicke narrowing of the resonance. Data and Figure reproduced with permission from James Keaveney.

apparent because of the long cell length. The fit for $L = 60$ nm in panel (a) with an Υ of 0.1 indicates a possible overestimation of the errors involved in the fitting procedure [30]. However, as discussed earlier, this is caused by the large background counts for such a short cell length.

5.3.2 Caesium D1 line

To corroborate the results found in Rb, and to test the model with other alkali-metal atoms, the experiment was performed in a Cs nanocell on the Cs D1 894 nm line, with large hyperfine splittings (9 GHz for the Cs ground states and 1.2 GHz on the excited states). Each hyperfine transition is separated such that it can be considered in isolation from all others, even in the presence of a large AS interaction. This allows the reliable

measurement of shifts with a precision of a few MHz.

Whilst the ability to address individual transitions gives exceptionally high resolution, the technical challenges of the Cs D1 line are greater than the Rb D2 line, primarily due to the transition wavelength. Firstly, the quantum efficiency of Si, used for detection in the SPCMs, is much lower at 894 nm than at 780 nm and hence the detectors are not as sensitive. Secondly, high transmission, narrow bandpass filters are currently not available at 894 nm meaning relatively more thermal background photons (of which there are more in absolute number compared to 780 nm) reach the detector. As a result of these two factors, we limit our investigation to nanocell thicknesses greater than 100 nm for the Cs D1 line in order to generate spectra with sufficiently high signal-to-background ratio.

Using the same methods as those to extract parameters for Rb, we find a value of $C_3^{6S_{1/2}\rightarrow 6P_{1/2}} = (1.9 \pm 0.1)$ kHz μm^3, a value that, while similar to the Rb coefficient, is in disagreement with theoretical expectations of $C_\alpha^{6S_{1/2}\rightarrow 6P_{1/2}} = 1$ kHz μm^3 [33].

In Fig. 5.8, we present a comparison of the red and blue wings of AS shifted transitions, the Cs $6S_{1/2}F_g = 3$ to $6P_{1/2}F_e = 3$, panel (a), and $F_e = 4$, panel (b). The blue line on both plots is a Lorentzian fit, i.e. one that excludes the AS interaction. The red line on panel (a) is a fit including the AS interaction, and is mirrored in panel (b), highlighting the asymmetry of the AS interaction.

Additional physical effects occurring in the cell not included in our simplified model [29], are fitted as a phenomenological excess Lorentzian broadening Γ_{ex}. Although this excess broadening does not account for all physical effects occurring inside the cell, it can be seen from Fig. 5.8b that it is sufficient in describing the line-shape in the absence of any AS effects. In this excitation scheme AS induced shifts are exclusively a red shift, as evidenced in Fig 5.8a. Hence, if the model can sufficiently describe the line-shape, the simplification of using Γ_{ex} is justified.

5.4 Determining the power law

To extract an exponent α, fit results from all spectra are taken, and we calculate an average weighted by the inverse of the Υ of the fit. The same treatment is performed on fitted values of $C_\alpha^{5S_{1/2}\rightarrow 5P_{3/2}}$ to determine the coupling coefficient. Ultimately we have

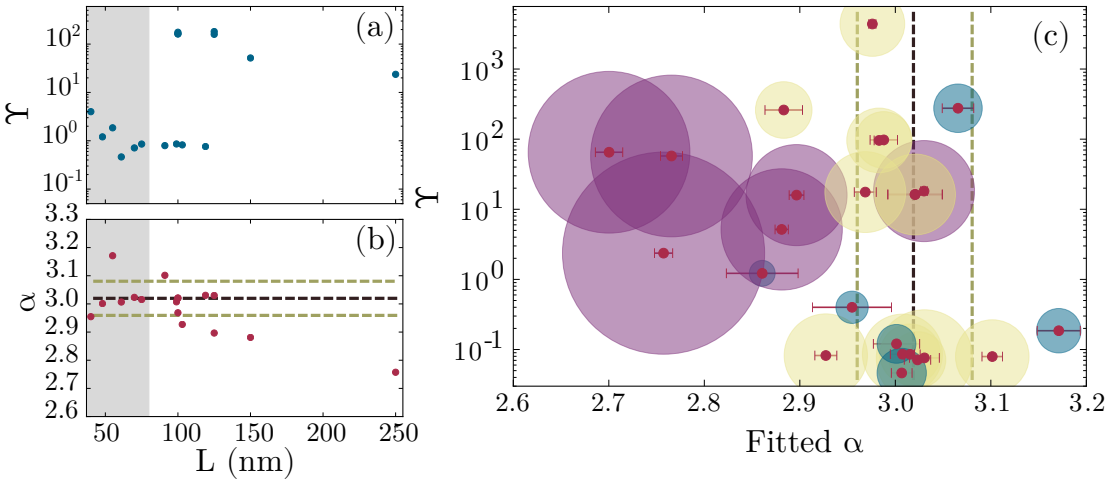

Figure 5.9: Length dependence of goodness of fit parameter ϒ [30], purple points in panel (a), and the fitted AS exponent α, red points in panel (b). The results from longer cell lengths generally have poorer fits than shorter cell lengths where the AS interaction dominates ($L <$ 80 nm), highlighted as a grey area. The final value of $\alpha = 3.02 \pm 0.06$ is plotted as a dashed black line, with the error bars plotted as beige dashed lines. (c) Fitted values of α and their goodness of fit [30], where lower values are indicative of a better fit. The sizes of the circles enclosing each point is relative to the maximum AS separation $r_{\max}$ used in the measurement, where $r_{\max} = L/2$. The results from longer cells ($r_{\max} > \lambda/2\pi$, purple circles) generally have poorer fits than cell lengths where the AS interaction dominates (32 nm $< r_{\max} < \lambda/2\pi$, yellow circles) and ($r_{\max} <$ 32 nm, blue circles). Most results from the thinner regions fall within the error bars (beige lines) calculated for this measurement (final value plotted as black line for reference).

determined the best values of α and $C_\alpha^{5S_{1/2}\to5P_{3/2}}$ for use in future fitting of absorption spectra. Using this method, we extracted a value of $\alpha = 3.02 \pm 0.06$, a value in good agreement with the theoretical expectation of $\alpha = 3.16$ for the ground state interaction, discussed in section 5.1.1. We also find a value of $C_\alpha^{5S_{1/2}\to5P_{3/2}} = 1.4 \pm 0.3$ kHz μm^3, not in agreement with theoretical calculations of $C_\alpha^{5S_{1/2}\to5P_{3/2}} = 2.1$ kHz μm^3 [26]. Quoted errors for all results are based on the standard deviation of the fit and do not include systematic effects.

The length dependence of the ϒ (blue points) of each ML fit with the corresponding fitted values of α (red points) are plotted in Figs. 5.9 a and b respectively. In panel b, the experimentally determined value is highlighted with a black dashed line, with the standard deviation plotted as grey dashed lines. Recalling Fig. 5.6 c, there is a range of

α where the cost value is minimal, between $\alpha = 3.2$ and 2.9. Comparing with Fig. 5.9c, we can see that the fitted α from the ML fitting method all lie within this length range, showing that the ML fit explored the whole region of lowest cost values of α, and still returns final fit parameters clustered around our final quoted value of α. In panel (a) the Υ of the fit is generally larger for longer cell lengths, where the AS shift is not appreciable. Fitted values of α and $C_3^{5S_{1/2}\rightarrow 5P_{3/2}}$ calculated at these longer lengths have very little bearing on the nature of the AS interaction, and a weighted average using Υ will decrease their impact on the final measured value. For shorter cell lengths $L < 80$ nm, the AS interactions have much stronger effects on the line shape also coinciding with smaller values of Υ, with most fitted values of α in good agreement with the final average value and its associated errors.

There may be more complex interactions occurring inside the cell [29], such as additional motional effects between photon absorption and fluorescence, multiple reflections and surface charges. However, we have demonstrated that a simple model is sufficient to describe the power law of $1/r^3$ for spectra over the length scales investigated. Furthermore, the effects of surface roughness [29] (on the order of 3 nm in both cells) are not a concern for our measurements. Atoms travel inside the cell at rms velocities exceeding 200 ms^{-1}, meaning atoms experience the surface roughness as a time averaged potential. Therefore at the distance ranges probed by this experiment, the AS separation can be considered to be well defined.

We postulate that the discrepancies between experiment and theory may be caused by rubidium adsorbed on the interior surface of the cell, interfering with the surface permittivity and therefore the reflection coefficient used to calculate $C_3^{5S_{1/2}\rightarrow 5P_{3/2}}$ [10, 23]. The effect of metallic layers on the surface affects only the $C_3^{5S_{1/2}\rightarrow 5P_{3/2}}$ coefficient, leaving the exponent of r^α unchanged [23]. This, in conjunction with the wide spread in low cost-value fitted C_α coefficients demonstrated in Fig. 5.6 leads us to conclude that vapour cells may not be an appropriate medium for the accurate measurement of C_3 without a rigorous theoretical treatment to account for the effects of surface atoms, currently beyond the scope of this experiment.

5.5 Outlook

In future we intend to utilize the methods developed herein to aid future investigations on the AS interaction, including the search for bound states close to the surface [34] and investigate higher-excited D states [5]. To further characterize our system, we also hope to look at the effects of radiation trapping [35]. Finally, we will use the model developed to aid in the fabrication and testing of nanocells being developed in Durham.

Bibliography

[1] K. A. Whittaker, J. Keaveney, I. G. Hughes, A. Sargsyan, D. Sarkisyan, and C. S. Adams, Phys. Rev. Lett. **112**, 253201 (2014).

[2] I. Hamdi, P. Todorov, A. Yarovitski, G. Dutier, I. Maurin, S. Saltiel, Y. Li, A. Lezama, T. Varzhapetyan, D. Sarkisyan, et al., Laser Phys. **15**, 987 (2005).

[3] H. Kübler, D. Booth, J. Sedlacek, P. Zabawa, and J. P. Shaffer, Phys. Rev. A **88**, 043810 (2013).

[4] A. Laliotis, T. P. d. Silans, I. Maurin, M. Ducloy, and D. Bloch, Nat. Comm. **5** (2014).

[5] H. Failache, S. Saltiel, M. Fichet, D. Bloch, and M. Ducloy, Phys. Rev. Lett. **83**, 5467 (1999).

[6] H. Bender, P. W. Courteille, C. Marzok, C. Zimmermann, and S. Slama, Phys. Rev. Lett. **104**, 083201 (2010).

[7] T. A. Pasquini, Y. Shin, C. Sanner, M. Saba, A. Schirotzek, D. E. Pritchard, and W. Ketterle, Phys. Rev. Lett. **93**, 223201 (2004).

[8] V. Druzhinina and M. DeKieviet, Phys. Rev. Lett. **91**, 193202 (2003).

[9] F. Shimizu, Phys. Rev. Lett. **86**, 987 (2001).

[10] C. Sukenik, M. Boshier, D. Cho, V. Sandoghdar, and E. Hinds, Phys. Rev. Lett. **70**, 560 (1993).

[11] V. Sandoghdar, C. Sukenik, E. A. Hinds, and S. Haroche, Phys. Rev. Lett. **68**, 3432 (1992).

[12] R. Grisenti, W. Schöllkopf, J. Toennies, G. Hegerfeldt, and T. Köhler, Phys. Rev. Lett. **83**, 1755 (1999).

[13] J. Perreault and A. Cronin, Phys. Rev. Lett. **95**, 133201 (2005).

[14] A. Landragin, J. Y. Courtois, G. Labeyrie, N. Vansteenkiste, C. I. Westbrook, and A. Aspect, Phys. Rev. Lett. **77**, 1464 (1996).

[15] A. K. Mohapatra and C. S. Unnikrishnan, Europhys. Lett. **73**, 839 (2006).

[16] J. E. Lennard-Jones, Trans. Faraday Soc. **28**, 333 (1932).

[17] H. B. G. Casimir and D. Polder, Phys. Rev. **73**, 360 (1948).

[18] L. Weller, R. J. Bettles, P. Siddons, C. S. Adams, and I. G. Hughes, J. Phys. B **44**, 195006 (2011).

[19] R. H. Dicke, Phys. Rev. **89**, 472 (1953).

[20] M. DeKieviet, U. D. Jentschura, and G. Lach, *Casimir Physics* (Springer Berlin Heidelberg, Berlin, Heidelberg, 2011).

[21] H. Friedrich, G. Jacoby, and C. G. Meister, Phys. Rev. A **65**, 032902 (2002).

[22] A. Caride, G. Klimchitskaya, V. Mostepanenko, and S. Zanette, Phys. Rev. A **71**, 042901 (2005).

[23] E. Eizner, B. Horovitz, and C. Henkel, Eur. Phys. J. D **66**, 321 (2012).

[24] H. de Freitas, M. Oria, and M. Chevrollier, Appl. Phys. B **75**, 703 (2002).

[25] M. Fichet, F. Schuller, D. Bloch, and M. Ducloy, Phys. Rev. A **51**, 1553 (1995).

[26] S. Ribeiro, (private communication).

[27] B. E. Sherlock and I. G. Hughes, Am. J. Phys. **77**, 111 (2009).

[28] J. Keaveney, Ph. d. thesis, Durham University (2013).

[29] D. Bloch, Phys. Rev. Lett. **114**, 049301 (2015).

[30] I. G. Hughes and T. P. A. Hase, *Measurements and their Uncertainties: A practical guide to modern error analysis* (OUP, Oxford, 2010).

[31] S. Kirkpatrick, C. D. Gelatt, and M. P. Vecchi, Science **220**, 671 (1983).

[32] M. A. Zentile, J. Keaveney, L. Weller, D. J. Whiting, C. S. Adams, and I. G. Hughes, Comp. Phys. Comm. **189** (2015).

[33] M. Chevrollier, M. Fichet, M. Oria, G. Rahmat, D. Bloch, and M. Ducloy, J. Phys. II **2**, 631 (1992).

[34] E. G. Lima, M. Chevrollier, O. Di Lorenzo, P. C. Segundo, and M. Oriá, Phys. Rev. A **62**, 013410 (2000).

[35] A. Fioretti, A. Molisch, J. Müller, P. Verkerk, and M. Allegrini, Opt. Comm. **149**, 415 (1998).

Chapter 6

Driving coherent dynamics

6.1 Introduction

The systems studied thus far have all been in the steady state and has not covered the time evolution of an atomic system driven by a laser. Furthermore all studies have been within the weak probe limit, where the intensity of the incident beam is so weak that negligible population transfer takes place. In this chapter we explore excitation by high powered beams, where large amounts of population are transferred between states. When there is sufficient population inversion, the exciting beam instead stimulates emission events returning population back to the ground state where it is ready to be re-excited. Hence, the medium has a mechanism to oscillate between the ground and excited state, called Rabi oscillations or alternatively, Rabi flopping.

In this chapter we drive this form of population transfer in the nanocell. Rabi oscillations have been well studied in many media including thermal vapours [1–3], ultra-cold atoms [4, 5] quantum dots [6, 7], electrical circuits [8], and semiconductors [9, 10]. However, the strong atomic confinement and high densities that can be reached in nanocells offer a unique new medium to study Rabi oscillations, with the full impact of extremely high densities on atomic level populations to be investigated. Furthermore, we can easily reach high density regimes where the inter-atomic separation is less than the excited state reduced wavelength. Atoms are therefore within each other's near field and are able to interact with each other via the dipole-dipole interaction. This leads to effects such as the cooperative Lamb shift [11]. Dynamics of such regimes have not been previously investi-

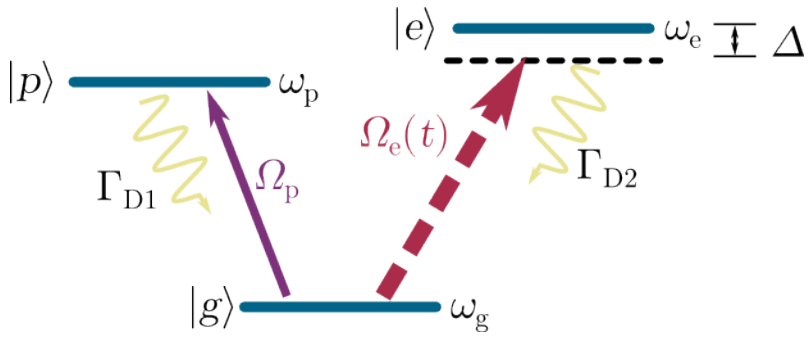

Figure 6.1: Level scheme used to probe coherent dynamics in the vapour. We use a 'vee' scheme exciting from ground state $|g\rangle$ to excited state $|e\rangle$ using a pulsed laser tuned to the rubidium D2 line with coupling frequency $\Omega_e(t)$ (dashed red arrow). The system is probed on the $|g\rangle$ to $|p\rangle$ transition using a CW laser on the D1 transition with coupling Rabi frequency Ω_p (solid purple arrow).

gated meaning that the study of coherent dynamics on nanocells presents a fascinating opportunity.

This chapter first builds a theoretical model, starting from a 2 level atom, moving up to a 3 level atom excited on a 'vee' system, using the basis of the optical Bloch equations discussed in chapter 2. Building on this, we develop a theoretical description of the time dependent dynamics occurring for a high power light pulse travelling through an atomic medium. We then describe the experimental set-up used to drive Rabi oscillations inside the nanocell and introduce the extended model used to simulate experimental results. The results are then discussed, where discrepancies between theory and experiment are closely examined with a particular emphasis of the effect of propagation effects of a pulse travelling through a medium with no effective decay mechanisms.

6.2 Coherent dynamics

6.2.1 2 level vapour response

We first review the 2 level optical Bloch equations that describe the time evolution of the density matrix $\hat{\rho}$ from chapter 2, derived using the Linblad master equation:

$$\dot{\hat{\rho}} = [\hat{\rho}, \mathcal{H}] - \hat{\Gamma}, \tag{6.1}$$

where $\mathcal{H}$ is the system Hamiltonian and $\hat{\Gamma}$ is the decay matrix. For a 2 level system with a ground state $|g\rangle$ and excited state $|e\rangle$ this results in a set of four coupled equations that describe the evolution of the system. For brevity, we concentrate only on the excited state population, starting from an initial rate equation derived directly from the master equation, initially excluding decay mechanisms:

$$\dot{\rho}_{\mathrm{ee}} = -\frac{i\Omega}{2}(\rho_{\mathrm{ge}} - \rho_{\mathrm{eg}}), \tag{6.2}$$

where Ω is the Rabi frequency, previously defined in section 2.1.1 as:

$$\Omega = -\frac{E_0 d_{\mathrm{ge}}}{\hbar}, \tag{6.3}$$

where d_{ge} is the dipole moment. Equation 6.2 describes the time dependent evolution of the excited state. Examining it, we can see that it is solely dependent on atomic coherences, meaning that when there are no coherences present population transfer cannot take place. Solving these and taking initial conditions of $\rho_{\mathrm{ee}}(t = 0) = 0$,$\rho_{\mathrm{ge}}(t = 0) = 0$ we find the solution (see *e.g.* [12]):

$$\rho_{\mathrm{ee}}(t) = \frac{\Omega}{\Omega'} \sin^2\left(\frac{\Omega' t}{2}\right), \tag{6.4}$$

with Ω', the effective Rabi frequency:

$$\Omega' = \sqrt{\Omega^2 + \Delta^2}, \tag{6.5}$$

where $\Delta = \omega - \omega_0$ is the detuning of the driving field frequency ω from the excited state resonant frequency ω_0. Ω is the Rabi frequency, first defined in Eq. 2.7, which describes the strength of the atom-light coupling induced by the driving laser field. We can see from Eq 6.4 that the population undergoes sinusoidal oscillations at frequency Ω', called Rabi oscillations.

When exciting an atomic medium instead of a single atom, oscillations are a collective response of the vapour. If all population is initially in the ground state, each atom will simultaneously start a Rabi oscillation keeping in phase with each other. Decoherence mechanisms such as spontaneous emission or collisional broadening result in a single atom returning to the ground state and restarting a Rabi oscillation out of phase with the rest of the medium. In time this results in loss of coherence as all atoms are oscillating in population at different rates. The medium eventually loses all coherence resulting in no further oscillations and the response reaches a steady state.

Rabi oscillations can be exploited to control state populations in an atomic medium. One such manipulation is the transfer of all population to either the ground or excited state via excitation of a medium by a laser pulse of an appropriate length. A pulse of length $t = \pi/\Omega$ is known as a 'π pulse'. For an atomic ensemble which initially has all population in the ground state a π pulse will transfer all population to the excited state. Extending this, a $\pi/2$ pulse of length $t = \pi/2\Omega$ transfers all population to an equal superposition of ground and excited states, an operation that has many utilities in quantum computation [13].

Nanocells offer a singular medium for study of such dynamics, as the reduced optical thickness means Rabi oscillations at high atomic vapour densities can be studied. At high densities, collisional effects reduce state lifetimes so strongly that a GHz driving Rabi frequency is required to observe some oscillatory dynamics before a steady state is reached. This is because the decay rate of atoms has a strong effect on the amount of oscillations observed. When the decay rate is large compared to the Rabi frequency, oscillations are quickly damped and only a few can be observed before the system reaches a steady state. If the Rabi frequency is large compared to the decay rate, many oscillations can occur before a steady state is reached.

6.2.2 3 level vapours

In chapters 2 and 3, all discussion is centred on vapours excited on a two level scheme in the weak-probe regime [14]. In this chapter we study dynamics in a 3 level system above the weak probe limit. Beyond the weak probe limit, optical pumping will occur in the vapour, resulting in population transfer between the states involved.

We probe a Rubidium vapour in a 2 μm length cell, using the 'vee' system displayed in Fig. 6.1. The vapour is excited from the $5S_{1/2}$ ground state $|g\rangle$ to the $5P_{3/2}$ excited state $|e\rangle$ by a 800 ps FWHM pulse (excitation wavelength $\lambda = 780$ nm), resulting in a time dependent coupling Rabi frequency $\Omega_e(t)$ (dashed arrow on Fig. 6.1). The resulting Rabi oscillations are monitored by a weak probe beam between state $|g\rangle$ to the $5P_{1/2}$ level, denoted as state $|p\rangle$ (excitation wavelength $\lambda = 795$ nm), purple arrow on figure.

Each state decays with their corresponding natural line-width $\Gamma_{D1,D2}$ and an additional rate Γ_{SB} corresponding to a reduction in lifetime caused by inter-atomic collisions previ-

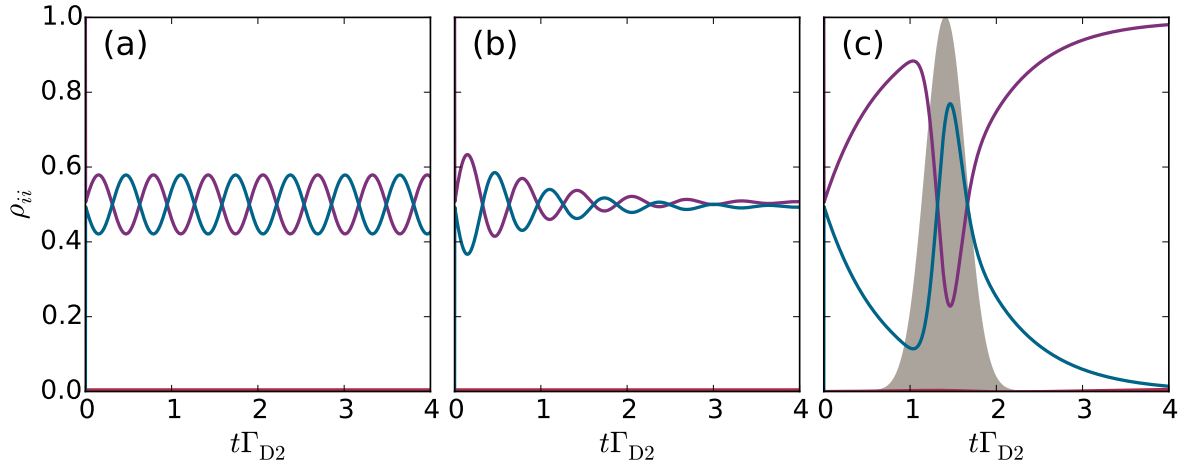

Figure 6.2: Optical Bloch simulation results for the 3 level vee system shown in Fig. 6.1, for starting parameters $\rho_{gg,ee} = 0.5$, $\Omega_e/2\pi = 127$ MHz and $\Omega_p/2\pi = 5$ MHz. The ground state population ρ_{gg} is plotted as a set of blue lines, the excited state ρ_{ee} is plotted in purple. The probe state population ρ_{pp} is plotted in red. Panel (a) shows the system response for CW excitation with no decay mechanisms present. Panel (b) shows the system response for a vapour with both spontaneous decay and decay due to inter-atomic collision events. Panel (c) shows the time evolution for a pulsed excitation beam of FWHM 10 ns. The exciting pulse is plotted as a grey area for reference. The time axis is scaled to the natural line-width of the excited state transition Γ_{D2}.

ously discussed in section 2.3.4. In order to apply the density matrix formalism outlined in section 2.2, some modifications must be made to the atomic Hamiltonian $\mathcal{H}$ and the decay matrix $\hat{\Gamma}$.

Firstly, a third level must be added resulting in a 3×3 Hamiltonian. Each state will have its own coupling Rabi frequency. As the system is excited by a pulsed pump laser, the Rabi frequency for state $|e\rangle$ is time dependent and takes the form of a Gaussian pulse, denoted as $\Omega_e(t)$. Each state can have effective detuning Δ_e and Δ_p for states $|e\rangle$ and $|p\rangle$ respectively. The resulting Hamiltonian is:

$$\mathcal{H} = \frac{\hbar}{2}\begin{pmatrix} 0 & \Omega_p & \Omega_e(t) \\ \Omega_p^* & -2\Delta_p & 0 \\ \Omega_e^*(t) & 0 & -2\Delta_e \end{pmatrix}, \tag{6.6}$$

where a * denotes a complex conjugate. The decay matrix is also altered to include decay

rates of both states:

$$\hat{\Gamma} = \begin{pmatrix} -(\Gamma_{D1} + \Gamma_{D2} + \Gamma_{SB})\rho_{gg} & \frac{\Gamma_{D1}+\Gamma_{SB,D1}}{2}\rho_{pg} & \frac{\Gamma_{D2}+\Gamma_{SB,D2}}{2}\rho_{eg} \\ \frac{\Gamma_{D1}}{2}\rho_{gp} & (\Gamma_{D1} + \Gamma_{SB,D1})\rho_{pp} & 0 \\ \frac{\Gamma_{D2}+\Gamma_{SB,D2}}{2}\rho_{ge} & 0 & (\Gamma_{D2} + \Gamma_{SB,D2})\rho_{ee} \end{pmatrix}, \tag{6.7}$$

where $\Gamma_{D1,D2}$ are the natural line-widths of the Rb D1 and D2 transitions, respectively.

Finding solutions for this system analytically is complex, requiring a 9×9 matrix to solve the resulting set of coupled equations. We therefore opt to solve it numerically to predict the system response. The results of such a simulation for a vapour excited at zero detuning (*i.e.* $\Delta_{e,p} = 0$) are shown in Fig. 6.2. Excited state population ρ_{ee} is plotted as a set of purple lines, ground state ρ_{gg} is plotted in blue and probe state ρ_{pp} is plotted in red. Panel (a) shows the population change with no decay mechanisms present, i.e. $\Gamma_0 = 0$ and $\Gamma_{SB} = 0$. Both the pump and probe beams are CW with time independent Rabi frequencies $\Omega_p = 2 \times 2\pi$ MHz and $\Omega_e = 120 \times 2\pi$ MHz. The time axis is scaled to the natural line-width of the excited state transition. The ground and excited state populations oscillate with no decay and will continue if the system is not perturbed. The probe state is weakly driven and hence the state occupation is low, as there are no other available channels for population transfer to take place.

Panel (b) shows the change in state populations for a vapour with decay mechanisms present. The state decays contain the natural line-widths of the D1 and D2 transitions for the probe and excited state respectively, as well as an additional self broadening term for a vapour at a temperature of 200°C, corresponding to self broadenings of approximately $\Gamma_{SB,D1} = 130$ MHz and $\Gamma_{SB,D2} = 190$ MHz. All other parameters are identical to those in panel (a). The populations still oscillate, but eventually reach a steady state.

Panel (c) shows the response for pulsed excitation, where $\Omega_e(t)$ is now a time dependent Gaussian with a FWHM of 10 ns with a peak Rabi frequency of $120 \times 2\pi$ MHz centred at $t = 1.40\Gamma_{D2}$, plotted on panel (c) as a grey area for reference. Here the response is centred around the peak of the exciting pulse, with states decaying naturally after the excitation excitation is finished.

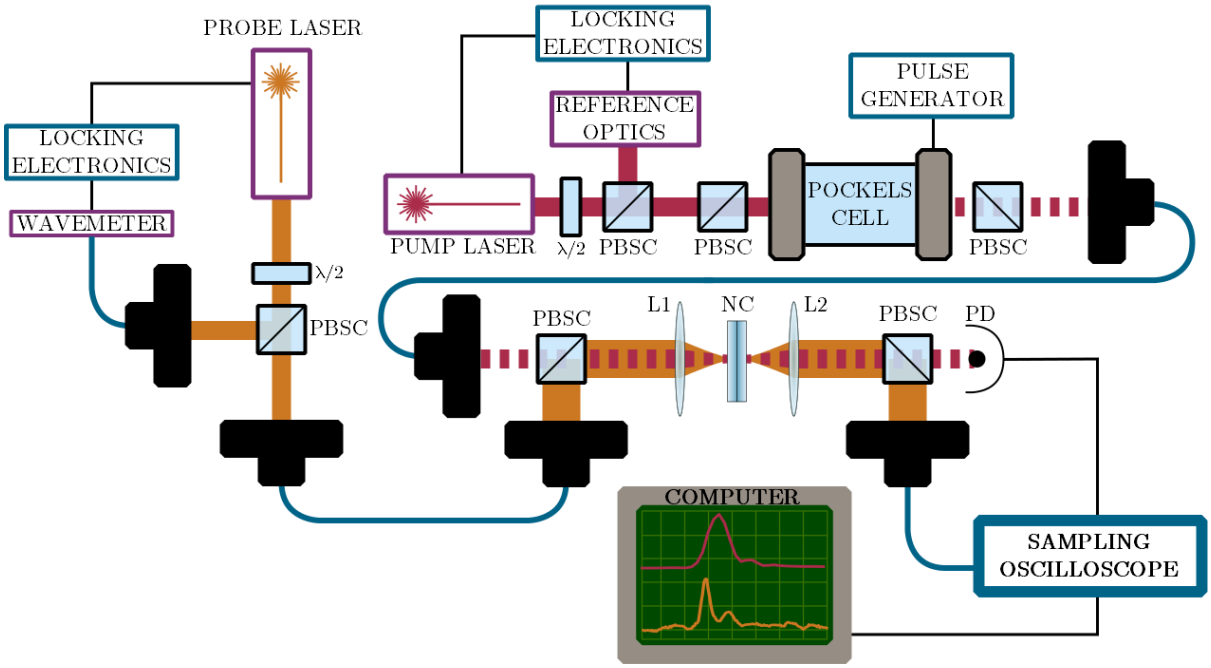

Figure 6.3: Experimental set-up used to probe coherent dynamics in the nanocell. The pump beam, orange, is tuned to the Rb D1 transition. Part of the beam is split off by a polarising beam splitter cube (PBSC) to be analysed by a wavemeter connected to a LABVIEW locking program that keeps the beam at a particular detuning. The rest of the beam is sent via an optical fibre to the nanocell. The pump beam, red, is tuned to the Rb D2 line. Part of the beam is split off by a PBSC to an reference optics for the locking electronics. The rest of the beam is sent though a Pockels cell. The Pockels cell is connected to an electrical pulse generator, which results in a pulsed beam that is sent via fibre to the nanocell. The pump and probe beam are combined on a PBSC before being sent though the nanocell. After the nanocell, the beams are split and sent on separate channels to the sampling oscilloscope, which on the figure displays typical signals $\Delta\mathcal{S}$ seen for a 800 ps FWHM pulse propagating through a heated nanocell. Signals from the scope are compiled on a computer ready for analysis.

6.3 Experimental Methods

The experimental set-up is shown in Fig. 6.3. Both the pump and probe beam are generated by diode lasers. The pump beam is displayed on the figure as a red beam. It is first split by a polarising beam-splitter cube (PBSC). The split beam is sent to reference optics which contain a polarisation spectroscopy set-up [15]. The signal is used as a reference for the locking electronics that keep the laser tuned to the ^{85}Rb F_g=3 to $F_e = 4$ transition. The rest of the pump beam is sent to a Pockels cell. On either side of the Pockels cell are crossed Glan-Taylor PBSCs. These PBSCs have an extremely high extinction ratio, exceeding 10^{-5} [16], resulting in negligible beam power transmitted through the Pockels cell when it is not activated. The Pockels cell is connected to an electrical pulse generator that generates an approximately Gaussian pulse with a FWHM $\tau_p = 800$ ps. The change in laser intensity of when the pulse is applied for a beam propagating through free space was measured on a single-photon counting module to determine the correct FWHM of the pulse. The electro-optic response of the Pockels cell results in a pulsed beam that can be sent to the nanocell.

The probe beam, illustrated in orange on Fig. 6.3, is tuned to the Rb D1 line. It is first split by a PBSC. Part of the beam is sent to a HighFinesse WS-7 wavemeter, resolution 0.1 pm. The laser wavelength is monitored and controlled by a LABVIEW locking program, allowing easy control over the detuning of the probe beam. The rest of the beam is fibred to the nanocell section of the experiment.

To ensure ease of detection the pump and probe beams are orthogonally linearly polarised so that the weak probe beam can be polarisation filtered from the strong pump signal after interacting inside the cell. The beams are combined on a PBSC before being focussed into the nanocell by lens L1. The probe beam has a larger initial diameter than the pump beam, resulting in a smaller focussed beam spot. This ensures that the region probed is well within the volume of vapour that has been optically excited by the pump beam, and that the region probed has minimised intensity variations from the Gaussian spatial profile of the pump beam. Lens L2 then re-collimates both beams for detection. The beams are then separated by another PBSC. The beams are detected by a PicoScope 9221A sampling oscilloscope, ideal for measurement of repetitive waveforms. The scope takes a single sample at a point in time from an individual waveform and repeats over many contiguous waveforms, varying the time that the sample is taken to reconstruct

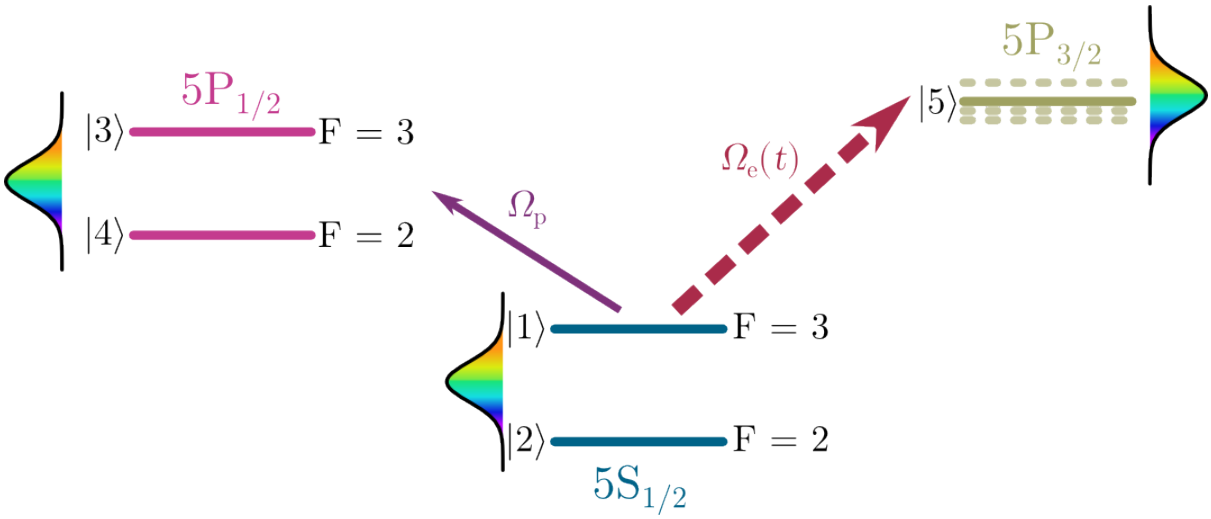

Figure 6.4: 5 level 'vee' system used to simulate experimental results. 5 Levels are needed to account for the bandwidth of the exciting pulse, plotted for reference next to each manifold as a rainbow coloured area. Both hyperfine splittings of the ground state manifold are used, resulting in two levels $|1\rangle$ and $|2\rangle$ corresponding to the $F = 3$ and $F = 2$ hyperfine states respectively (blue lines). The D1 manifold hyperfine splittings are also included, with states $|3\rangle$ and $|4\rangle$ corresponding to the $F = 3$ and $F = 2$ hyperfine states (pink lines). The frequency difference for the Zeeman hyperfine splittings of the D2 manifold are less than the pulse bandwidth and so is included as a single state $|5\rangle$ (beige lines).

the full waveform. Outputs are necessarily averages and are compiled on a connected computer, resulting in a measurement of the overall change in signal $\Delta\mathcal{S}$. The pump beam is detected by an EOT 2030A fast photodiode with a 2 GHz bandwidth. The probe signal is sent to the optical input of the PicoScope (8 GHz bandwidth) via a fibre collimator.

As we are studying interactions at high temperatures, decoherence induced by inter-atomic collisions is much more probable, with lifetimes at a maximum of 5 ns. Hence, in order to observe evolving dynamics large Rabi frequencies on the order of GHz must be used. For this reason we excite on the D1 and D2 transitions, used for their large dipole moments. The strength of these transitions mean that large Rabi frequencies can be attained with relatively low beam powers.

6.4 Results

In this section we present a comparison of experimental results to the expected response calculated by an optical Bloch simulation. The simulation used includes 5 levels and is outlined in [11], with the energy level diagram shown in Fig. 6.4. The bandwidth of the exciting pulse is 1 GHz, illustrated as a rainbow area on Fig. 6.4. The laser bandwidth is broader than the frequency difference of the hyperfine splittings of the $5P_{3/2}$ manifold, hence these states are considered as a single state in the simulation with decay rate Γ_{D2}. However, this bandwidth is smaller than the hyperfine splittings of the $5S_{1/2}$ to $5P_{1/2}$ transition, and so we consider both the F = 2 and F = 3 states of the $5P_{1/2}$ manifold in the simulation, with decay rate Γ_{D1}. The hyperfine splitting of the $5S_{1/2}$ state is also larger and so both the F = 2 and F = 3 hyperfine states are considered in the model. Hence the resulting theoretical model is a 5 level 'vee' system encompassing all possible transitions.

All measurements were taken in a 2 μm length cell, the maximum nanocell length available. This length was used as a high powered beam can still be transmitted through the cell on resonance at high temperatures (exceeding 300°C), despite the high density. Additionally, it has some small propagation length to allow dynamics to evolve. The responses investigated are dependencies on density, power and detuning. We first examine the density dependent results, expecting that the probe laser will show an increase of oscillations with increasing temperature, before such a high temperature is reached that inter-atomic collisions cause dephasing and therefore loss of coherent dynamics, where the probe response will have no oscillations in population. We will next examine the pump power dependence, expecting from the dependence on electric field in Eq. 6.3 that we will observe a $\sqrt{P}$ dependence on the Rabi frequency. We then examine the response of the probe laser detuning. As the detuning increases, we expect that in accordance with Eq. 6.5 the observed Rabi flopping will increase in frequency but the strength fo the signal will be reduced as less atoms are excited. This will result in lower signal-to-noise as the contrast between fringes is greatly reduced.

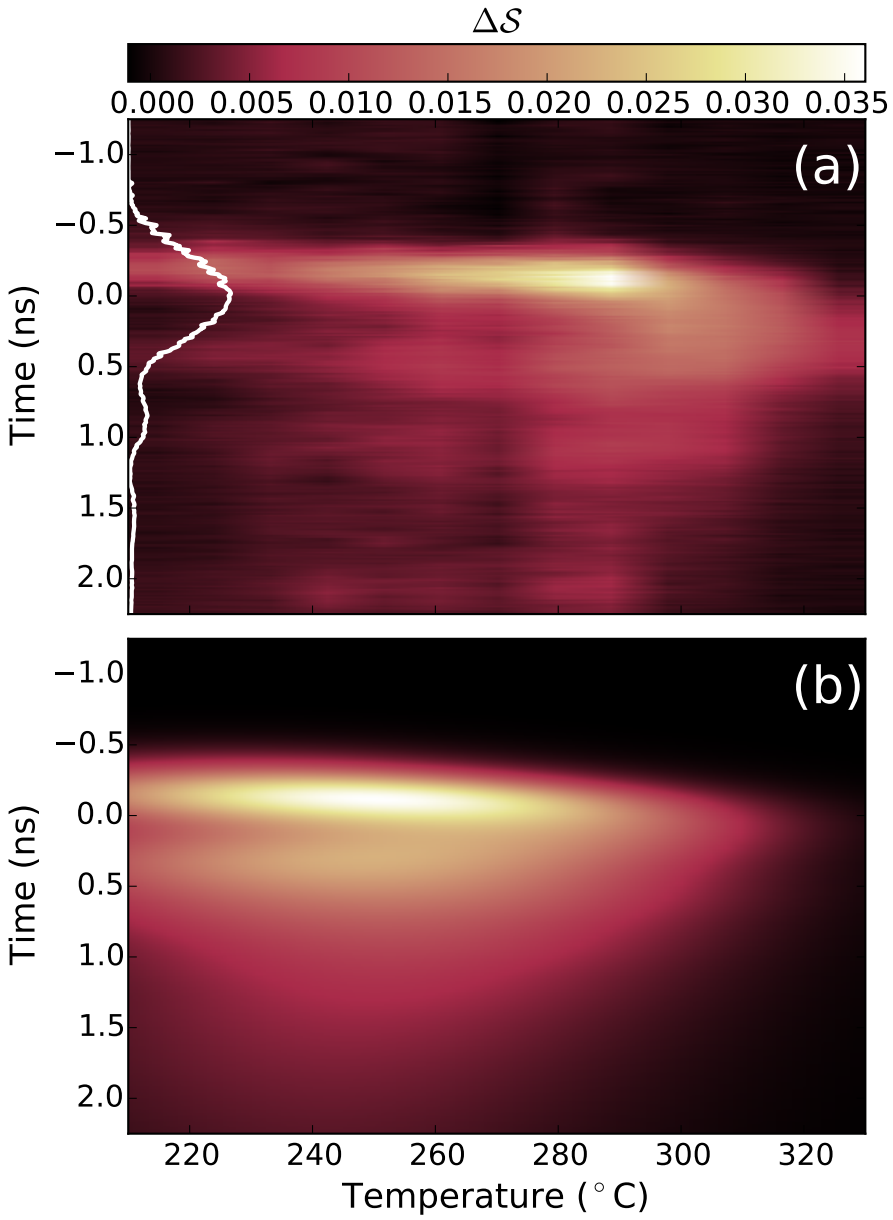

Figure 6.5: (a) Response of vapour to increasing temperature. Each vertical slice represents the change in signal strength $\Delta\mathcal{S}$ of the probe beam at temperature T. The exciting pulse is plotted as a white line for reference. The time axis is shifted such that $t = 0$ represents the peak of the input pulse. (b) Expected vapour response as calculated by the 5 level optical Bloch simulation.

6.4.1 Density dependence

The density dependent results were taken on resonance ($\Delta_{\mathrm{p,e}} = 0$) at a peak pump power of 86 mW. The resultant detected change in signal is plotted in Fig 6.5a. Each vertical slice represents the change in detected probe signal at a particular temperature. For reference, the detected excitation pulse is plotted as a white line. The time axis is shifted such that $t = 0$ s corresponds to the peak of the exciting pulse. For comparison the theoretical vapour response is plotted in panel (b) of the figure.

It is clear that there is some qualitative similarities between the experimental and theoretical results. The pulse dynamics evolve similarly in both instances, with several oscillations initially discernible. The oscillations diminish at high temperatures as increased collisional effects result in a loss of coherence. However, the experimental probe response is narrower and has a peak response at a higher temperature. These differences are indicative that our model of the response is incomplete and that further dynamics beyond a linear optical Bloch model are occurring within the vapour.

6.4.2 Power dependence

The power dependent results were taken on resonance ($\Delta_{\mathrm{p,e}} = 0$) at a vapour temperature of $T = 200^{\circ}$ C, corresponding to a density of $9.2{\times}10^{16}$ cm^{-3}, corresponding to a Γ_{SB} of 190 MHz. Each vertical segment on Fig 6.6a shows the experimental change in signal $\Delta\mathcal{S}$ of the probe beam for increasing pump beam power (calculated as the power at the peak of the input pulse). The response at $P = 5$ mW shows no oscillatory response as the pump laser power is not strong enough to induce coupling between the states and therefore no Rabi oscillations. Hence the response at $P = 5$ mW follows the profile of the input pulse.

For comparison the theoretical response of the vapour is plotted in Fig. 6.6(b). Again, both signals have a qualitative agreement. However, the secondary oscillation in the experimental response is static in time with the peak response of the second oscillation staying constant around $t = 0.25$ ns. In contrast, the secondary theoretical oscillation peak responses are not static in time moving from 0.5 ns to -0.1 ns as the pump power increases. Again, this is indicative that further dynamics are occurring inside the cell.

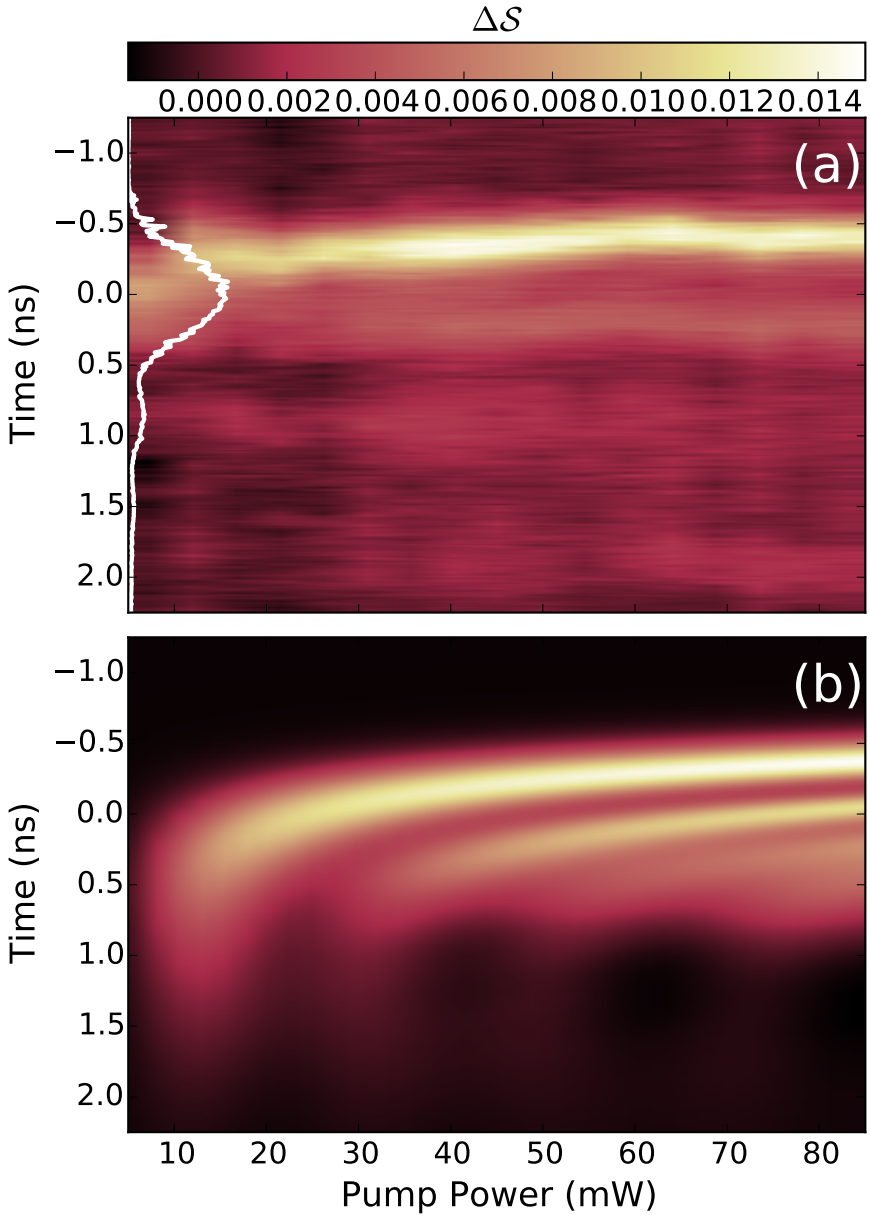

Figure 6.6: (a) Experimental change in signal $\Delta\mathcal{S}$ of the probe signal for increasing pump laser power. The detected pump pulse is plotted as a white line for reference. The time axis is scaled such that $t = 0$ represents the peak of the input pulse. (b) Expected vapour response as calculated by the 5 level optical Bloch simulation.

Parameter	$\Upsilon_{\text{RiseTime}}$	$\Upsilon_{\text{PeakTime}}$
Δ	23	760
P	0.93	15
T	2.5	44

Table 6.1: Reduced chi-squared values (Υ) for the theoretically calculated rise times and peak times of the probe response.

6.4.3 Detuning dependence

The detuning dependent results were taken at a peak pump laser power of 85 mW at a vapour temperature of $T = 200°$ C, corresponding to a density of 9.2×10^{16} cm^{-3}. The resultant change in signal at various probe detunings Δ_{p} are shown as vertical slices on Fig. 6.7. The probe pulse is plotted as a black line, and time scales are shifted such that $t = 0$ is the peak of the probe pulse. For comparison the theoretical response as calculated by the 5 level optical Bloch simulation is plotted in panel (b).

Again, there is some qualitative agreement between the theoretical and experimental responses. However, this data set demonstrates a very large difference in peak response between experimental and theoretical results. The experimental response for the first oscillation is much earlier and narrower than theoretically expected. In the next section we will further quantify these differences by comparing the difference in the time of the initial response for experimental and theoretical results as well as the rise time of the first probe response.

6.4.4 Pulse Steepening

To quantify the differences between theory and experiment, we plot the 10-90% rise times of the first oscillation for each experimentally measured probe response as blue squares on Fig 6.8a-c. The values calculated from the theoretical optical Bloch simulation are plotted as black points. The responses for the detuning, power and temperature dependences are shown on panels a, b and c respectively. We also calculate the reduced chi-squared Υ [17] of each dataset as a measure of accuracy of the theoretical model. The results are shown in Table 6.1. Υ is calculated as in section 5.2.3. Inspecting the 90-10% rise times on Fig. 6.8a-c, we can see that the results for probe detuning and temperature are

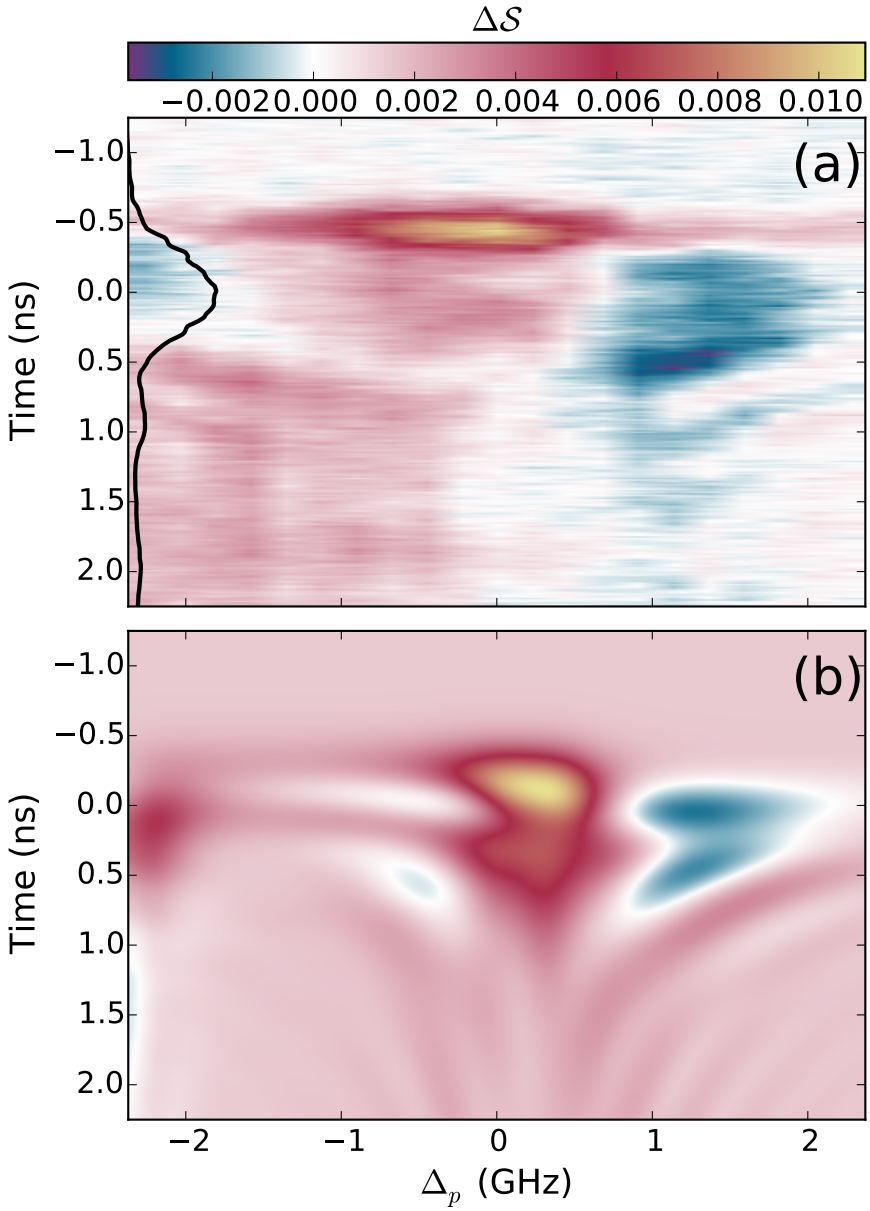

Figure 6.7: (a) Experimental change in signal $\Delta\mathcal{S}$ of the probe signal for a range of probe beam detunings. The detected pump pulse is plotted as a black line for reference. The time axis is scaled such that $t = 0$ represents the peak of the input pulse. (b) Expected vapour response as calculated by the 5 level optical Bloch simulation.

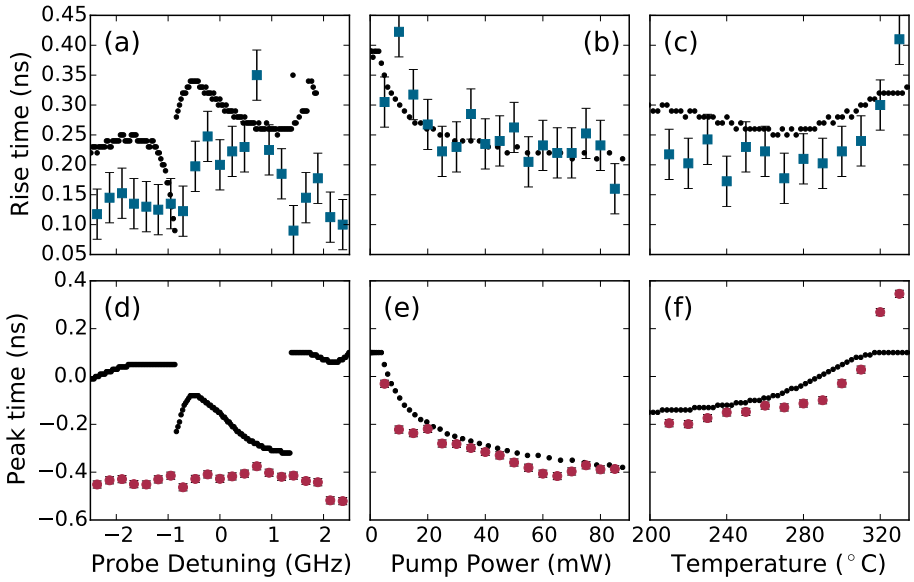

Figure 6.8: Comparison of experimental and theoretical rise times (panels a-c) and peak response times (panels d-f) with their associated errors. The rise times and peak response times are plotted for each data set shown in the previous subsection- Detuning dependence (panels a and d), power dependence (panels b and e) and temperature dependence (panels c and f). Experimental data for the 10-90 % rise times are plotted as blue squares on panels a-c. Theoretical values are plotted as black points. Experimental data for the time of the peak probe response are plotted as red circles on panels d-f. For comparison the theoretical values are plotted as black points

consistently faster than expected theoretically, indicating some steepening of the vapour response. The results for pump power dependence have an excellent fit, meaning that failure of the model is likely based in density and detuning dependencies.

The peak response time results in Fig. 6.8d-f demonstrate that the response is generally earlier than expected. This is most striking in the detuning results (with an Υ of 760) but is a common trend across all three sets, with no data presenting as a good fit. Combined with the general trend of decreased rise times, we can conclude that propagation effects are missing from the model. The inclusion of propagation effects necessitates a far more complicated Maxwell-Bloch model, which is beyond the scope of this thesis.

6.5 Discussion

All results have demonstrated an unexpected response of the vapour. The probe signal, specifically the peak response time, evolves significantly faster than would be expected for a typical 3 level vapour. Peak responses are detected earlier than the peak of the pulse, where one would typically expect the strongest probe response. Hence we must conclude that there are further dynamics taking place that are unaccounted for.

We can certainly infer from the results shown herein that the current model needs to account for propagation effects within the medium. As the laser pulse propagates through the medium, its electric field will have some effect on the complex electric susceptibility of the vapour it is incident upon, although this effect is negligible in the weak probe regime. When the driving field is strong enough to induce level population changes, significant differences can be observed. This leads non-linear effects and often have a strong dependence on the density of the vapour. This is evidenced in the results with dynamics evolving faster than predicted, particularly for the temperature and detuning dependence results, both of which have large effects on the refractive index and therefore propagation dynamics.

To properly simulate propagation effects, the change in polarisation must be calculated for each infinitesimal layer dz over the entire cell length z. Solutions for the Bloch equations must be calculated for each layer in order. The calculations simulating propagation effects in this experiment were performed by Thomas Ogden and are fully outlined in [18]. The results of the simulation have excellent agreement with the experimental measurements presented and hence suggest the formation of optical simultons inside the medium [19]. Simultons are simultaneously propagating solitons. To explain this we must consider the area theorem of Mccall and Hahn [20]. The theorem examines the interaction of pulsed coherent light with a medium by studying it in terms of the pulse area, expressed as an envelope function of the electric field of the pulse. In doing so, they find that the pulse area is altered as it propagates though the medium.

We first consider a pulse with an enclosed area greater than π propagating through the medium. If the pulse is sufficiently short that that there are no available decay mechanisms, i.e. $\tau_{\text{pulse}} < 1/(\Gamma_0 + \Gamma_{\text{col}})$, pulse areas will tend towards the nearest even multiple of π. In the case of pulses of area smaller than π, the area will tend to zero

and the signal will absorbed in the medium following the familiar Beer-Lambert law. If the pulse area is greater than π, the area tends towards 2π as it propagates though the medium. The resulting 2π pulse induces a full population oscillation where state populations move from the ground to excited and back to the ground state. The net result is a pulse of area 2π that propagates losslessly though the medium.

It can further be shown that for a pulse propagating under these conditions, the *only* solution is a pulse of area 2π [21]. Hence, if a pulse has an enclosed area greater than 3π, like the pulses we excite with herein, it will split up into multiple pulses of varying width, amplitude and velocities [22]. The results observed here could certainly be interpreted as an initial splitting of the input pulse into two, and the results presented in [18] presents the formation of simultons as a compelling explanation for the dynamics observed in these results.

However, the modelling demonstrates that the lengths used in this experiment are too short for these dynamics to fully develop, with the resultant pulse exiting the medium relatively unchanged. Splitting of the pulse is predicted to be observed at lengths exceeding 10 μm [18]. However, the partial formation of simultons still has a strong effect on coherent dynamics in the medium, including decreased response time in the medium.

6.6 Outlook

Driving coherent dynamics in the nanocell has led to some very unexpected results. The induced population oscillations have a strong trend of faster than expected reaction times that are not predicted with a theoretical model that excludes propagation effects. When propagation effects are included [18], there is strong evidence for the formation of simultons inside the medium. Simultons have yet to be corroborated experimentally in non crystalline media, and so these results represent an exciting new development in the field of pulse propagation. However, full splitting of the pulse into two simultaneously propagating solitions is not predicted for the lengths available in the nanocell, and so future experiments will focus on repeating the experiment in cells of a length of 10 - 100 μm, produced at NAS in Armenia. The experiment is expected to produce experimental corroboration of simulton formulation inside the medium.

This chapter concludes the section of this thesis discussing experiments performed using

nanocells. With their strong confinement they offer an excellent controlled medium to study fundamental physics, and have been used in many other instances for excellent studies, such as superluminal propagation [23], experimental confirmation of the cooperative Lamb shift [24] and the study of the hyperfine Paschen-Back regime [25, 26]. There is also some potential for practical applications, as the extremely narrow resonances and high densities make nanocells excellent candidates for high transmission atomic line filters [27]. However, for future experiments or to customise cells for particular applications, we need more control over the fabrication process. Hence the next part will discuss to design and fabrication of nanocells in Durham.

Bibliography

[1] B. Huber, T. Baluktsian, M. Schlagmüller, A. Kölle, H. Kübler, R. Löw, and T. Pfau, Phys. Rev. Lett. **107**, 243001 (2011).

[2] T. Baluktsian, B. Huber, R. Löw, and T. Pfau, Phys. Rev. Lett. **110**, 123001 (2013).

[3] Y.-H. Chen, F. Ripka, R. Löw, and T. Pfau, Applied Physics B **122**, 1 (2016).

[4] E. Nicklas, H. Strobel, T. Zibold, C. Gross, B. A. Malomed, P. G. Kevrekidis, and M. K. Oberthaler, Phys. Rev. Lett. **107**, 193001 (2011).

[5] S. Blatt, J. W. Thomsen, G. K. Campbell, A. D. Ludlow, M. D. Swallows, M. J. Martin, M. M. Boyd, and J. Ye, Phys. Rev. A **80**, 052703 (2009).

[6] Q. Q. Wang, A. Muller, P. Bianucci, E. Rossi, Q. K. Xue, T. Takagahara, C. Piermarocchi, A. H. MacDonald, and C. K. Shih, Phys. Rev. B **72**, 035306 (2005).

[7] T. H. Stievater, X. Li, D. G. Steel, D. Gammon, D. S. Katzer, D. Park, C. Piermarocchi, and L. J. Sham, Phys. Rev. Lett. **87**, 133603 (2001).

[8] D. R. McCamey, H. A. Seipel, S. Y. Paik, M. J. Walter, N. J. Borys, J. M. Lupton, and C. Boehme, N. Mat. pp. 723–728 (2008).

[9] O. D. Mücke, T. Tritschler, M. Wegener, U. Morgner, and F. X. Kärtner, Phys. Rev. Lett. **87**, 057401 (2001).

[10] S. T. Cundiff, A. Knorr, J. Feldmann, S. W. Koch, E. O. Göbel, and H. Nickel, Phys. Rev. Lett. **73**, 1178 (1994).

[11] J. Keaveney, Ph. d. thesis, Durham University (2013).

[12] R. Loudon, *The Quantum Theory of Light* (OUP, Oxford, 2000), 3rd ed.

[13] C. Monroe, D. M. Meekhof, B. E. King, W. M. Itano, and D. J. Wineland, Phys. Rev. Lett. **75**, 4714 (1995).

[14] B. E. Sherlock and I. G. Hughes, Am. J. Phys. **77**, 111 (2009).

[15] C. P. Pearman, C. S. Adams, S. G. Cox, P. F. Griffin, D. A. Smith, and I. G. Hughes, J. Phys. B **35**, 5141 (2002).

[16] Y. Takubo, N. Takeda, J. H. Huang, K. Muroo, and M. Yamamoto, Meas. Sci. and Technol. **9**, 20 (1998).

[17] I. G. Hughes and T. P. A. Hase, *Measurements and their Uncertainties: A practical guide to modern error analysis* (OUP, Oxford, 2010).

[18] T. P. Ogden, Ph. d. thesis, Durham University (2016).

[19] L. Allen and J. H. Eberly, *Optical Resonance and Two-Level Atoms* (Wiley, New York, 1975).

[20] S. L. McCall and E. L. Hahn, Phys. Rev. Lett. **18**, 908 (1967).

[21] L. Matulic and J. H. Eberly, Phys. Rev. A **6**, 1258 (1972).

[22] G. L. Lamb, Rev. Mod. Phys. **43**, 99 (1971).

[23] J. Keaveney, I. G. Hughes, A. Sargsyan, D. Sarkisyan, and C. S. Adams, Phys. Rev. Lett. **109**, 233001 (2012).

[24] J. Keaveney, A. Sargsyan, U. Krohn, I. G. Hughes, D. Sarkisyan, and C. S. Adams, Phys. Rev. Lett. **108**, 173601 (2012).

[25] A. Sargsyan, R. Mirzoyan, and D. Sarkisyan, JETP Letters **96**, 303 (2012).

[26] A. Sargsyan, G. Hakhumyan, C. Leroy, Y. Pashayan-Leroy, A. Papoyan, and D. Sarkisyan, Opt. Lett. **37**, 1379 (2012).

[27] J. Keaveney, A. Sargsyan, D. Sarkisyan, A. Papoyan, and C. S. Adams, Journal of Physics B: Atomic, Molecular and Optical Physics **47**, 075002 (2014).

Part III

Nanocell fabrication

Chapter 7

Nanocell Fabrication

7.1 Introduction

The nanocell experiments outlined in previous chapters have all been performed inside cells produced by colleagues at NAS in Armenia. However, to expand upon these experiments and to find practical applications for the cells, further customisation is needed. In order to make cells tailored to our needs, we have expanded the experiment into cell fabrication.

By producing our own ultra-thin cells, we can make changes to the interior cell chamber, including small microstructures to guide atoms inside the cell, similar to experiments done in photonic hollow core fibers [1], or work on vapours trapped inside porous structures [2]. Further changes could include small plasmonic structures on the cells interior windows [3] to alter electric fields and therefore interactions inside the cell. Ultimately, customising the interior will allow us to fine tune interactions occurring inside the cell, opening up new physical regimes to study in thermal vapour cells.

With full control over the fabrication process, we are also able to have a complete knowledge of all materials and processes involved, and can minimise common problems with other cells, such as the use of glues, which offer easy fabrication methods but are not suitable for high temperature applications. By careful selection of materials used for the science chamber, we can also improve operating temperatures of the cells, allowing even higher densities to be reached, giving the option to study atom-atom interactions.

Additionally, we will be able to ensure the purity of the cells atmosphere and measure the internal pressure before the cell is filled with alkali-metal. Finally, every property of the cell can be carefully monitored, giving us far greater knowledge about the cell properties, for example, surface roughness measurements of the cell interior, allowing us to characterise the full length variation at very short distances.

Building our own cells means that we can adapt them for use in many applications. With the right set up, alkali vapour cells can be used as very sensitive (fT level) magnetometers [4], for imaging of electric fields [5], frequency filters [6], atomic clocks [7] and optical isolators [8].

There is some competition in the field of microfabrication of alkali vapour cells, with much work [9–11] focusing on mm length cells produced by anodic bonding of stacks of glass and silicon, producing several compact cells simultaneously at wafer level before dicing for the creation of tens of cells simultaneously. Anodic bonding is a relatively popular construction method, and has also been used to produce micron length vapour cells with internal electrodes included inside for work on Rydberg atoms [12].

The production of micron and sub-micron length cells is also an active field of study. Pfau *et al.* in Stuttgart have produced several cells with lengths on the order of tens of microns, initially using optical contacting to create the cell science chamber, before moving onto anodic bonding. Sargsyan *et al* in Yerevan produce the nanocells used in previous experiments discussed in this thesis. The cells are made of two aluminium oxide windows. One window is ground to a very large radius of curvature (R >100 m), resulting in a very slight length variation. The windows are then bonded using an unknown method, resulting in a cell with a length variation between 50-2000 nm with a maximum operating temperature of 350°C and lifetimes on the order of several years.

For cells produced in Durham, we have several requirements. The primary requirement is a sub-micron thickness, to continue working in the physical regimes studied in this thesis, including dynamics of a very thin vapour layer; interactions in extremely reduced volumes; interactions at extreme vapour densities and atom-surface interactions.

Secondly, a reasonably large maximum operating temperature to allow for measurement of spectra. For extremely short cell lengths, the absorption is not detectable until a sufficiently high density has been reached, which occurs at a temperature around 150 °C for a 500 nm length cell. However, maximum operating temperatures are limited by the

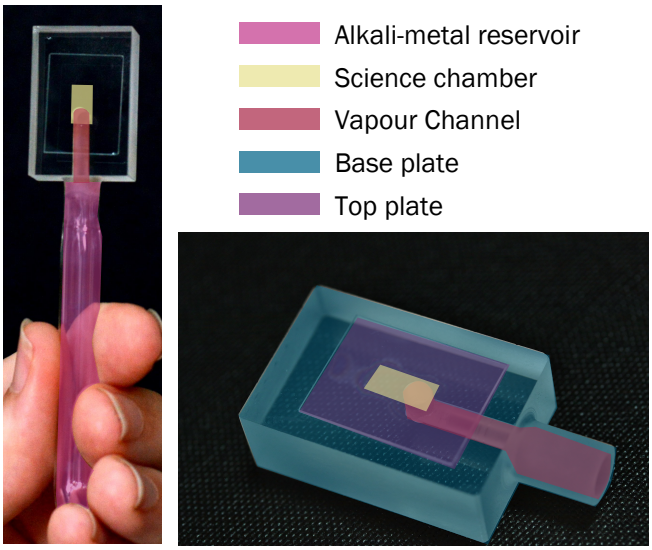

Figure 7.1: Vapour cell demonstrating nomenclature for areas of ultra-thin cells that will be used in this chapter.

adhesive used for construction, or the reaction of the alkali vapour with the cell window material, weakening it and forming brown alkali-metal oxides which reduce transmission of light through the cell.

Good optical access is also required, as many experiments we perform involve collecting light from angles all around the cell, for example collecting off-axis scattered light, see chapter 5. Finally, we require good control over the cell atmosphere. For initial cells we wish to entirely remove any buffer gases, with a final product that is evacuated to a high vacuum before loading to ensure a completely pure atmosphere. However, the production methods must also allow for specially selected buffer gases to be included for use in later experiments where the presence of buffer gases can enhance instead of confuse experimental results.

For clarity and ease of discussion, Fig. 7.1 shows a picture of a vapour cell labelled with the nomenclature used for sections of the cell within this chapter. Vapour cells have a reservoir, highlighted in pink on the figure, where the alkali-metal is kept and heated to produce vapour. There is also a cell science chamber, highlighted in yellow, where the gas is confined for laser interrogation. Leading between the reservoir and science chamber is the vapour channel, highlighted in red, allowing the gas to move from the reservoir to the science chamber. Cells made herein will also have 2 extra parts, a 'top plate', purple, which is etched with a thin region that will act as the science chamber, and a 'base plate',

blue area, containing the vapour channel.

In this chapter, I will cover the entire cell fabrication process, from initial research to final testing. Initially construction methods will be discussed, explaining choices made in the final design; potential bonding and fabrication methods; selection of appropriate materials and alkali-metal loading methods. Next the fabrication process will be fully outlined, discussing successes and failures of initial prototypes before outlining the full fabrication process for the final cell design. The success of the cells will be measured via testing of the cells interior atmosphere, measurements of the interior length and corroborating the behaviour of spectra from the new cell with spectra from previous experiments, to check the spectra from the cell are in agreement with other fully functional cells. Finally, we will discuss designs for future cells and discuss possible experimental uses for them.

7.2 Methods

7.2.1 Bonding and construction

Standard alkali-vapour cells are often made using scientific glass blowing methods or by gluing of cell windows. Modern cell fabrication has moved beyond these methods. For many applications, adhesives can be harmful to experimental results, as they generally have high vapour pressures, contaminating the cell atmosphere and interfering with spectral widths [13]. Although low-outgassing glues for high vacuum applications such as Torr Seal are available, such glues are limited in their maximum operating temperature to below the minimum required to measure spectra in ultra-thin cells. Additionally, many adhesives have poor hermiticity, allowing contaminants from the ambient atmosphere to diffuse into the cell, further contaminating the atmosphere and reducing potential cell lifetimes [13]. For specialist cells outside of operation at room temperature, glues are not an appropriate construction method, and we have avoided the use of them.

Scientific glass blowing certainly creates high quality cells, with no dangers of outgassing. Despite this obvious advantage, standard glass blowing techniques cannot create a cell chamber with the incredibly short length that we are seeking to make, and hence we seek construction methods that can be used in conjunction with glass blowing for our final design.

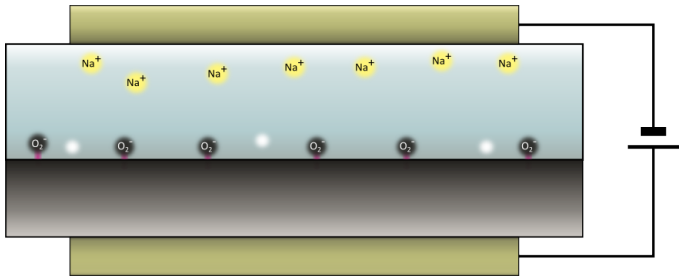

Figure 7.2: Schematic of the anodic bonding process. Substrates to be bonded are placed between 2 electrodes. Vacancies are formed at the bond interface by the diffusion of sodium atoms towards the cathode. Silicon atoms can then move into these vacancies forming silicon-oxide bonds.

Vacuum encapsulation methods used as a part of Micro-Electro-Mechanical Systems (MEMS) technology can easily be adapted for use in vapour cell fabrication. We will examine two MEMS methods that have already been adapted to vapour cell technology; anodic bonding and optical contacting.

Anodic Bonding uses two reasonably well polished (surface roughness $R_A < 10$ nm [13]) wafers of high sodium content glass and silicon. The wafers are positioned together and placed between a cathode and anode, with the cathode in contact with the glass, as shown in Fig. 7.2. The set-up is then heated to 500 °C and a voltage of 1 kV is sent though the bonding area. High voltages are required to allow the dielectric glass to conduct the electric field. Na^+ and O_2^- ions in the glass act as charge carriers, their mobility enhanced by the high temperature. The mobile sodium ions are attracted towards the cathode, leaving vacancies near the bond interface as seen in Fig. 7.2. The oxygen ions move towards these vacancies forming a permanent silicon-oxide bonds at the interface that holds the surfaces together. The bonded wafers are then slowly cooled, forming a strong hermetic bond between the two wafers [13].

Anodic bonding is popular for cell fabrication as it offers a relatively low fabrication temperature. It does however require the use of sodium doped glass, limiting the possible materials used and also requires the use of silicon, reducing optical access into the cell. However, the silicon layer can be very thin and can be sputtered on in thin layers to provide the silicon needed to form the bond [12]. The bonded surfaces should be clean, but the bond is still relatively resistant to surface impurities.

This method can also be used to include other structures inside the science chamber, as

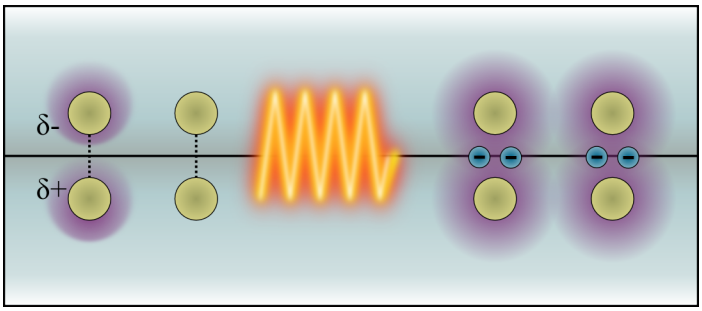

Figure 7.3: Illustration of the optical contact bonding process. An initial bond is formed via van der Waal forces at the interface. After an annealing step where the bond is heated to over 1000°C, permanent covalent bonds are formed at the bond interface.

demonstrated by Daschner *et al.* [12] with the inclusion of gold electrodes inside their vapour science chambers. Choice of metallic structures should be careful, as some metals such as platinum repel the bonding interface, causing a void around the structure which can be undesirable. This could, however be used as a design feature to create voids several microns thick [14], providing a potential self construction method for micron length cells with internal plasmonic structures.

Drawbacks to this method include the need for high voltages and a good match in coefficient of thermal expansion (CTE) of the materials. If the CTEs are not well matched, cracks due to stresses caused by different expansion rates will occur during the cooling process [13]. Hence, cells made using this process require a CTE close to that of silicon.

Optical Contact Bonding [15] (OCB), known in silicon MEMS as direct bonding requires no glues or intermediate layers, relying instead on inter-surface forces. Two clean surfaces with a high flatness ($< \lambda/20$) and extremely low surface roughness (R_A < 1 nm) [13] are brought into intimate contact. At sub nm length ranges, the van der Waal and dipole-dipole attraction between both surfaces are very strong, and join the two surfaces together, as seen in Fig. 7.3. This bond is not permanent and can easily be broken by pulling the two wafers apart, but it can be made permanent by an annealing step, using chemical, pressure or thermal methods to make the bond permanent. The bond is also very sensitive to any contaminants on the surface as inter-surface separations must not exceed more than a nanometre and impurities such as dust can reach sizes of a micron, disrupting the bond and forming a void, a space in the bond interface where the bond has not formed.

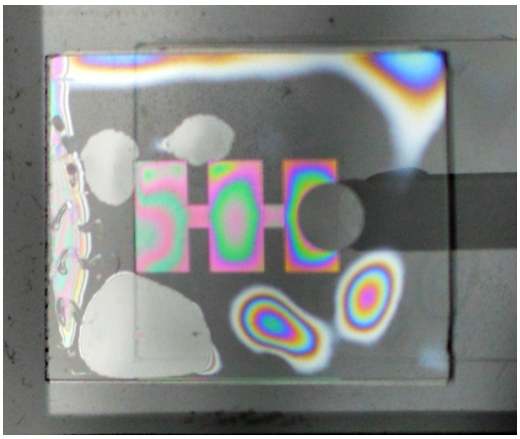

Figure 7.4: Demonstration of voids in an OCB bond. The voids appear as interference fringes from white light incident on the bonded interface. Several void sizes can be observed, with the larger voids reaching the coherence length of white light

The bond can be made permanent by an annealing process, often implemented by heating to high temperatures. For glasses this is close to the transition temperature T_g [13]. At such elevated temperatures it is now energetically favourable for the formation of siloxane bonds at the interface. Siloxane is two silicon atoms bonded to a single oxygen atom, denoted here as Si−O−Si, where − represents inter-atomic bonds. The chemical formation of these bonds comes from a reaction between silicon that is embedded in the surface and hydroxyl groups present on the surface itself, mediated in part by water present on the surface. The final step involves the formation of siloxane bonds, which can only occur at temperatures exceeding 800°C. A by-product of the reaction is the formation of excess water molecules, which then diffuse away from the bonded area. The full description is beyond the scope of this thesis, and can be found in [16] but the overall chemical reaction is described as:

$$\mathrm{Si-OH + OH-Si \rightarrow Si-O-Si + H_2O.}$$

The final result of the process is a strong bond that is almost entirely clear, with a reflection coefficient of $2{\times}10^{-5}$ [15]. Bond strength is also sensitive to differences in CTE [13].

Bonding temperature can be lowered to accommodate for temperature sensitive components. If the bonding temperature is lowered, heating must take place for an extended time to allow for enough siloxane bonds to be formed at the surface. However, if the

annealing temperature is too low, the water formed during the bonding process cannot sufficiently diffuse from the bonding interface [16] forming voids in the bonded surface.

Voids in the bond are areas where the bond has not formed properly. They are caused by surface impurities or defects, which increase the distance between the two surfaces, reducing the strength of the inter-surface forces. These voids are demonstrated in Fig. 7.4, which shows an OCB between an etched fused silica plate and a fused silica substrate. The bond has then been annealed at 1000°C to make the bond permanent. The etched area is the coloured rectangular regions on the figure. The bonding voids are identified as the amorphous areas with coloured interference fringes, caused by white light interference in the areas where an OCB has not formed. The figure demonstrates several void thicknesses; the shorter voids have wider and widely distributed fringes. The thickness of larger voids approach the coherence length of white light (50 microns for a white LED), evidenced by closely spaced barely perceptible fringes.

In this case, the voids are likely caused by impurities or defects on the surface and have degraded the quality of the bond. In the particular case of the bond shown in Fig. 7.4, it is unsuitable for use as a vapour cell, as the bonded area around the etched region is not large enough and may not be sufficiently hermetic. The shape and distribution of voids changes during the heating process, with some voids disappearing as the surface relaxes, and some increasing in size if water has not diffused sufficiently from the bonding interface. Hence it is not always possible to determine if an OCB is successful until after the heating process. Reduction of void formation during the bonding process has been extensively studied [17, 18], and can be reduced through thorough cleaning processes, plasma or UV treatment of the bonding surfaces and careful control of the annealing process.

OCB has many features that are advantageous for the cell we wish to build, namely the clarity of the bond, allowing for much greater optical access. The initial positioning step is reversible, so several attempts can be made to reposition the surfaces, ensuring a bond is well aligned and of high quality. It is also suitable for a wide range of materials, including silicon, borosilicate, fused silica, aluminium oxide and many metals.

All methods discussed here are susceptible to cracking under thermal stress if different materials are used for components due to differences in CTE. Hence, we choose to use the same material for the entire cell.

For the final product, we have chosen to use optical contacting, which will result in a cell that has maximal optical access; is suitable for a wide variety of materials and requires only one material to make. Additionally, OCB can be performed by hand requiring a minimum of instrumentation- only cleaning materials and a high temperature furnace. OCB can also be performed using bonding tools, with procedures outlined in excellent detail in [13].

7.2.2 Optical engineering methods

To create a sufficiently short cell we use plasma etching to remove small amounts of material from the top plate surface. Plasma etching is a dry etch process, using ionised gas to remove material, as opposed to a wet etch method that uses acids such as Hydrogen fluoride or Nitric acid to remove selected areas.

The material removal process for plasma etching takes place in a large evacuated chamber containing the substrate to be etched and the plasma. In preparation for the etching process, the substrate is covered in a mask, usually a photoresist layer, that leaves the area to be etched exposed. The process can be repeated several times with different masks to achieve multiple different etch depths.

The material removal process is a chemical reaction, an ion is adsorbed on the surface and then reacts with it, bonding with atoms in the surface to form a molecule. By control of parameters such as the surface temperature, the product molecule is encouraged to desorp from the surface where it can be pumped away from the system. For plasma etching process used in this project, material removal rates are 40 nm min^{-1}. The process used does not attack the entire surface evenly, meaning that some areas are etched more than others resulting in an additional surface roughness on the etched surface. These irregularities are on the order of a few nm, and so will be quantified during the cell production process.

For machining other parts, we use ultrasonic milling, a method superior to machining with diamond tip drills, as the stress induced on the glass by the friction from direct contact with the drill creates cracks in the glass around the machined area. Ultrasonic machining cuts glass using an oscillating tool surrounded by an abrasive slurry. All the cutting is done by the slurry, so the stress to the glass is greatly reduced, resulting in a

clean cut with no cracks [19].

7.2.3 Loading

There are 2 options for cell loading, either vacuum encapsulation of alkali-metal dispensers or distilling of liquid alkali-metal into the cell reservoir.

Alkali metal dispensers (AMDs) are made of compounds containing alkali metals, which upon heating generate a controlled amount of high purity alkali metal vapour along with inert vacuum safe (low outgassing) by-products of the chemical reaction used to create the vapour. The heating can come from ohmic heating via electrical connectors attached to the dispenser or by shining a focussed laser onto the dispenser.

Dispensers offer many attractive options for vacuum encapsulation and miniaturization of cells because they are easy to work with. They can come in contact with air and can be handled without any safety equipment. However, they are limited to a maximum temperature of 700°C, making it an unsuitable candidate for encapsulation in an optically contacted structure because of the high thermal load during the annealing phase.

Gaseous by-products created by some dispensers include CO_2,N_2 and C_2H_4 [20]. In cold atom experiments, these by-products are not harmful to an ultra-high vacuum environment as experiments are usually continuously pumped, removing the excess gas. However, alkali metal vapour cells are self contained vacuum systems so excess gases produced cannot be pumped away and will permanently contaminate the cell atmosphere. This can be mitigated by including getter material inside the cell, a compound that readily absorbs the by-products of AMDs. Getters have been effectively used in mm length cells [9] and in the production of ultra-compact MOTs [21].

Using scientific glass blowing methods, pure alkali metal can be distilled into a reservoir by connecting the cell to a glass loading manifold, pictured in Fig. 7.5. The loading manifold comprises of 3 sections- a connection to a vacuum pump, an ampoule containing the alkali metal to be loaded and a connection to the cell science chamber.

The Rb must be kept isolated from air to avoid oxidation of the surface and combustion. Hence, the Rb is initially kept in a break-seal ampoule, drawn schematically in Fig 7.5. The ampoule has a thin 'tail' on one end surrounded by short tubing that can be attached to the loading manifold. Ball bearings are also placed inside the manifold that are

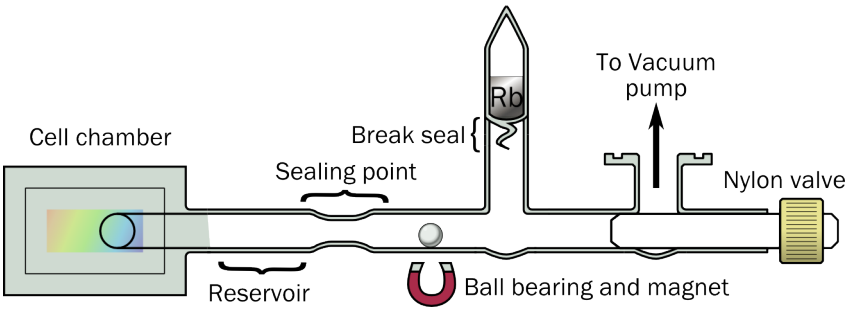

Figure 7.5: Loading manifold for sealing with pure Rb. Rb is sealed in a chamber that can be broken using a ball bearing that is placed inside the manifold. The rubidium is then distilled into the cell reservoir using a heat gradient.

manipulated using magnets to break the glass tail once the loading manifold has been evacuated.

To load a cell using distilled Rb, the manifold in Fig. 7.5a is evacuated to a high vacuum, around 10^{-5} mbar in the case of cells made in this thesis. Once the cell has been pumped down, the ball bearing inside the manifold is manipulated from the outside using a magnet to shatter the break-seal containing the Rb. A temperature gradient is then applied to the manifold, with the Rb break-seal ampoule heated and the desired cell reservoir cooled, causing the heated Rb to condense in the reservoir region.

The main body of the cell is connected to the manifold, with a narrow restriction between the final cell region and the loading manifold. When Rb has successfully been distilled into the cell reservoir, the narrowed region is heated to a working temperature, and forces due to the pressure differential between the exterior atmosphere and the evacuated manifold interior pull in the narrowed cell walls, forming a permanent seal and cutting the cell off from the loading manifold.

Loading using pure alkali metal offers many advantages over the use of AMDs. The technique is well known to professional glass blowers, and impurities inside the cell are minimised. We choose to use distillation of liquid Rb to load the cells as it is simple and easily accessible. Future designs may feature encapsulation of AMDs as manipulating Rb without the need for inert atmosphere or vacuum offers many possibilities for miniaturisation [9].

7.2.4 Material selection

Appropriate selection of materials is paramount. Our cell must be made of only one material, to avoid any stresses on the bonded interface induced by differing CTEs, as the cell will be regularly cycled in heat. Important aspects for the chosen material to have are: chemical inertness/resistance, to avoid interactions between extremely reactive rubidium and the cell walls; good transmission in the near-infrared range for good optical access and finally, it must be suitable for glass-blowing techniques. We do not consider permeability of the cell material as the cell can function sufficiently in high vacuum conditions.

The reaction of the cell material with hot alkali vapour is of particular concern. Alkali vapour attack not only discolours the wall, decreasing the amount of light transmitted through the cell, but attacks the cell surface itself, increasing surface roughness, which will potentially distort wavefronts propagating through the cell. Furthermore, it can also weaken the material itself, making it brittle and susceptible to breakage [22].

Borosilicate Glass: Silica glass mixture doped with boric oxide for good chemical resistance and strength. It is commonly used for optical elements, laboratory and kitchen glassware, and low temperature vapour cells. Maximum temperature for borosilicate cells is limited to 150°C due to rubidium reacting with the glass at higher temperatures. Borosilicate is extremely suitable for glass blowing, having a relatively low working temperature (500°C) and being easy to cut and dice [23].

Fused silica: Non-crystalline quartz (SiO_2) which has high chemical stability and excellent optical properties. Used for substrates in semiconductor material growth, high temperature vacuum chamber windows and high quality optics. Maximum cell temperature is limited to 230°C before the windows brown due to reaction with the alkali metal [12]. Fused silica can be manipulated using glass blowing techniques, although its higher viscosity means that workability is less than that of borosilicate [23].

Aluminium oxide, or pure sapphire is an excellent candidate for alkali-metal cell material, with extremely high chemical resistivity, able to withstand attack from hot alkali vapours at temperatures exceeding 1000°C [24]. It is extremely hard and brittle, making it difficult to machine. Its crystalline structure also means that it cannot be manipulated using glass blowing techniques.

The final choice for cell material is fused silica. The maximum temperature before reaction with the alkali vapour is sufficient for initial prototyping to test the construction methods. Aluminium oxide cells would be a preferable choice for future cells, as the high chemical resistance means that even higher density regimes could be accessed, and its hardness means that the cell will be more resistant to damage, increasing the potential cell lifetime. However, it is not suitable for glass blowing techniques, and so we elect not to use it for the initial prototypes. It may, however, be used in future cells in conjunction with encapsulation of AMDs.

In conclusion, the cells will be made from fused silica, chosen because of its reasonable chemical resistance and suitability for glass blowing. The cell science chamber will be plasma etched, and cell parts will be machined using ultrasonic milling. For construction of the cell, surfaces will be bonded using optical contact bonding as it is relatively simple to implement, can be used in conjunction with etched substrates to create suitably short cell lengths and produces a strong permanent hermetic clear bond. The cell will then be loaded with liquid Rb via a distillation process. In the next section, the fabrication process will be discussed, from initial testing and prototyping to final testing.

7.3 Fabrication

Fabrication has several stages, with initial prototyping to test out processes and ideas, production of the first and second generation of cells and finally testing of successful cells.

7.3.1 Adhesives and AMDs

For an initial test of alternative fabrication processes, we explored the use of AMDs and adhesives. To test this, 10 mm diameter borosilicate tubes were glued at one end with a glass disc using a glue to be tested. An AMD was placed inside each tube before they were evacuated and permanently sealed from atmosphere. As a control, an additional tube sealed only by glass blowing methods containing an AMD was also made. The AMDs were activated by heating with a focussed 3 W laser at 780 nm. After 10 minutes of heating, sufficient vapour was released by the dispenser for a signal to be observed.

The tubes are pictured in Fig. 7.6a. Glues tested were two types of room temperature

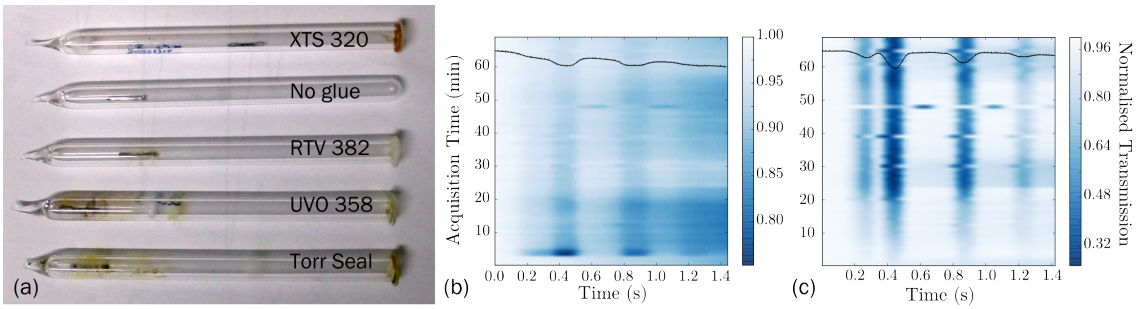

Figure 7.6: (a) Borosilicate tubes containing an AMD used for testing glues. Each sample is an evacuated tube sealed at one end with a glass disc attached with a glue to be tested. Also pictured is a reference tube containing just an AMD. (b) Time dependence of transmission signal from XTS 320 test tube heated to 120°C. The black trace shows a sample signal from when absorption is at its maximum(c) Time dependence of transmission signal from reference tube, taken simultaneously with panel (b). The black trace shows an example signal.

vulcanising silicone glues, RTV 382 and XTS 320; UV curing glue UVO 358 and an adhesive recommended for high vacuum operations, Torr Seal. All tubes gave an initial signal after laser activation of the AMD, but all glued tubes lost their signal within a few hours due to degradation of the glue from reactions with the Rb vapour, the extreme heat applied or the poor hermiticity of the glue. This is demonstrated with spectra taken from the XTS 320 tube in Fig. 7.6b. Acquisition was started at time = 0 min when the heater was turned on. The temperature eventually reached a maximum of 120°C at 25 mins into data acquisition. For spectra from the XTS 320, absorption gradually increased, although was then quickly lost. Additionally, a sample signal from when absorption is maximum is plotted on the panel as a black trace. The spectral lines are also broadened, indicating the presence of contaminant gases, possibly caused by the reaction of Rb vapour with the glue. Signals from all other glued tubes exhibited the same behaviour, therefore we conclude that these adhesives are not appropriate for construction of ultra-thin cells, as they will need to withstand much higher temperatures and attack from Rb vapour. The adhesives used are a good representative of low-outgassing glues that are commercially available. Although these are suitable for use in lower temperature applications, the high temperatures requires for nanocell functionality make them unsuitable for use. Future use of adhesives could centre around seeking specialist glues, but these can still limit maximum operating temperature to a few hundred degrees, and will be subject to a larger thermal expansion than a pure glass or crystal cell.

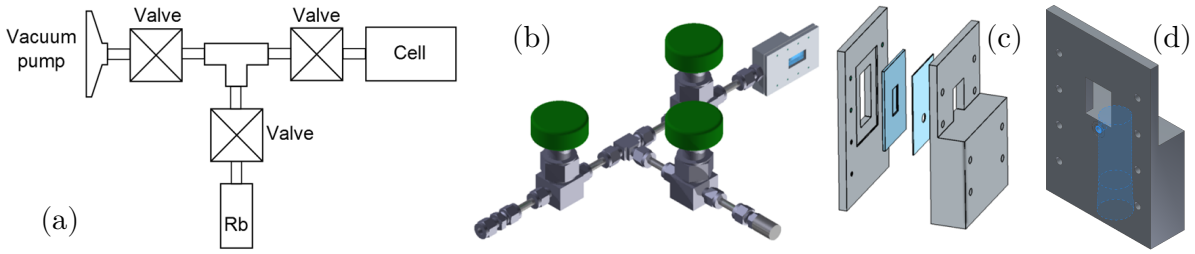

Figure 7.7: (a) Schematic of initial cell prototype, rendered in panel (b). A stainless steel main body with a modular design that connects an Rb reservoir, optically contacted cell region and vacuum pump connector via 3 valves. Panel (c) shows an exploded view of the cell science chamber.

The time dependence of transmission spectra from the reference tube is plotted in Fig. 7.6c, with a sample spectrum shown as a black line on the panel. The signal evolves exactly as expected for a heated alkali-metal vapour, and the signal stays consistent after an hour of acquisition, indicating that as long as an AMD is properly sealed inside a container, it is a sufficient source for an alkali-metal reservoir. Hence, we will consider AMDs for future cell fabrication.

7.3.2 Prototype 1

The first ultra-thin cell prototype is a modular design with a main body made of stainless steel Swagelok vacuum components. The main body connects 3 valves via a T-junction that leads to a vacuum pump, Rb reservoir and the science chamber, shown schematically in Fig. 7.7a and rendered in Fig. 7.7b.

7.7c shows an exploded view of the science chamber. It is made of 2 optically contacted fused silica plates, one etched with a 500 nm deep rectangular region, and the other with a hole drilled though to allow Rb vapour to flow into the cell. The science chamber is connected to the main body via an o-ring connection to a custom stainless steel connector, pictured in Fig. 7.7d. The delivery channel for Rb vapour to move from the reservoir to the cell science chamber is highlighted in blue.

The Rb reservoir was loaded in a nitrogen glove box, where Rb was melted and transferred to a glass test-tube with a glass to metal seal connecting the reservoir to the main cell body.

This design was created in collaboration with colleagues at the Max-Planck Institute for Light in Erlangen. The stainless steel body was chosen to avoid glass blowing methods, streamlining the production process, as using glass blowing techniques requires professional assistance which adds waiting times onto the overall production time. It can also easily be disconnected and reconnected to a vacuum pump, meaning the cell atmosphere can be monitored and maintained. The alkali-metal reservoir can be removed and replaced

Production time for this design was relatively fast, taking a month to fabricate. However, the final cell yielded no measurable results. The cell was very large, meaning that gaining an even distribution of temperature for every part of the cell was challenging. The temperature required to gain a measurable spectrum could not be reached across the whole cell, with local hot and cold spots that could have encouraged condensation of Rb before it reaches the science chamber. The glass to metal seal used also limits the maximum possible temperature for the cell to 200°C, and means that extreme care should be taken when cycling in temperature.

Another possibility for failure could be diffusion of Rb into the cell science chamber. Rb atoms must diffuse around a corner though a 5 mm x 500 nm gap. As no signal was measured from the cell, monitoring diffusion of the atoms could not be performed. However, this phenomenon can be studied in future successful cells.

Another observation from the production of this prototype was that under vacuum, flat plates will bow inwards due to the pressure differential between the high vacuum interior and the exterior atmospheric pressure. Such bowing can be modelled using Kirchoff-Love theory for rectangular plates [25], and the expected length variation for the plate used in the prototype is shown in Fig. 7.8.

This means cell science chambers will always have some length variation, which can be considered both an advantage and a flaw; length variation is very useful for performing length dependent experiments, but requires focussing of the beam to ensure only one particular length is being probed. Additionally, this requires the need to introduce measurements of the position dependent length of the cell.

Design features that will be brought forward from this initial prototype are the optically contacted chamber, which worked successfully, with the bond appearing to be hermetic-no pressure loss was observed inside the cell science chamber. The custom stainless steel

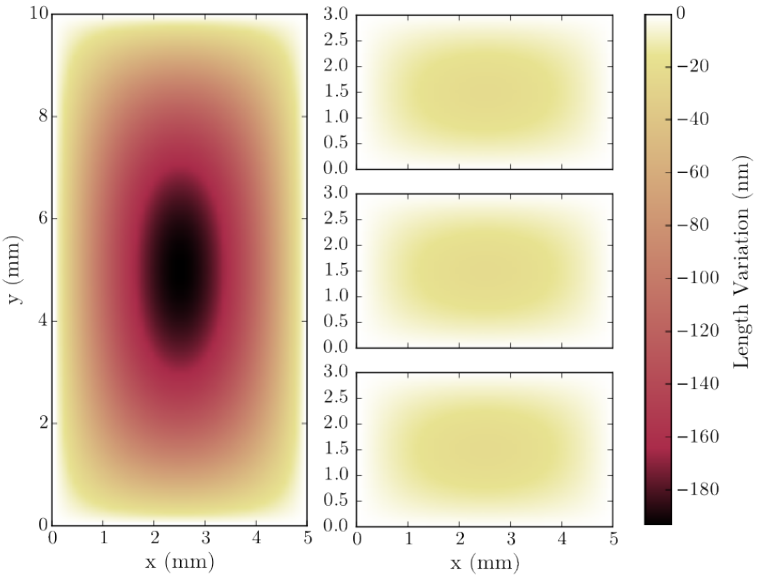

Figure 7.8: (a) Expected length variation due to bowing under atmospheric pressure of a 5×10×0.5 mm quartz plate. (b) Expected length variation of several smaller 5×3×0.5 mm plates, of thicknesses 0.5, 0.75 and 1 μm length from top to bottom. The thicknesses used are representative of a layout used for later cell designs.

connector was also adapted to be made entirely of fused silica.

7.3.3 Second Prototype

Several adaptations were made to the prototype to make a functional cell. Firstly, the cell is made entirely of fused silica, removing any stainless steel parts. The steel vacuum components greatly increased the size of the cell, and the reaction between Rb vapour and steel at high temperatures is unknown. Additionally, the increased thermal conductivity makes heating quicker, but without proper insulation leads to many temperature gradients all over the construction, harming the cells final function.

The full process used to fabricate this cell is shown in Fig. 7.9. Most fabrication steps were performed in-house (red boxes on Fig. 7.9) at Durham, although some were too expensive or technical to carry out ourselves, and so were contracted out to external professional services, highlighted as blue boxes on Fig. 7.9. To ensure a high quality OCB, some stages are carried out in a clean room and are highlighted in yellow on Fig. 7.9.

The cell is also no longer modular and is instead a permanently sealed vacuum system

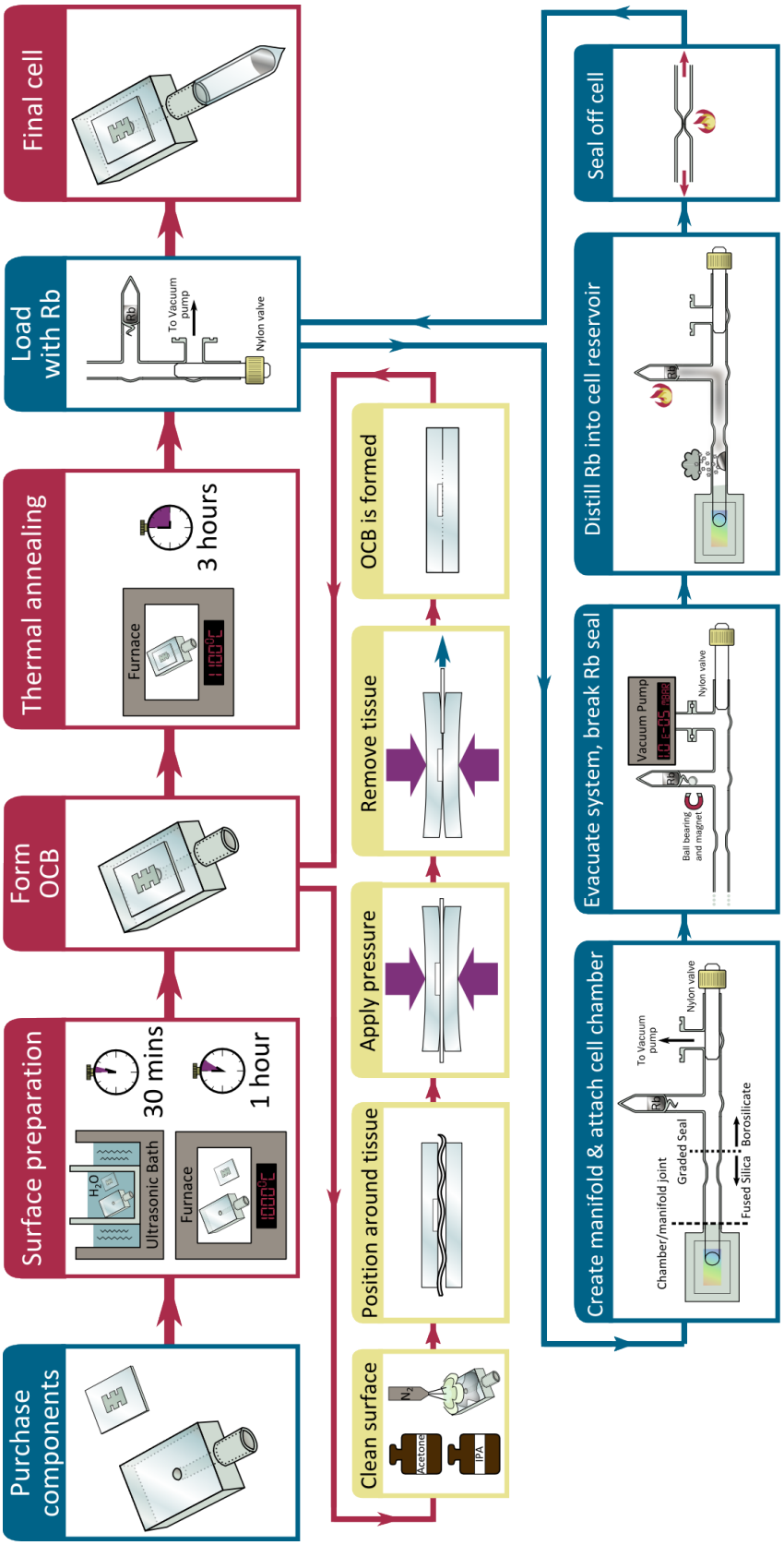

Figure 7.9: Production process used to fabricate fused silica nanocells. The boxes are colour coded such that blue boxes indicate the process was contracted externally, red boxes are steps performed in Durham, and yellow boxes indicate the step was performed in a clean room environment. The optical contact bonding (OCB), outlined in section 7.3.4, and Rb loading phases, outlined in section 7.3.5 are expanded below the main process.

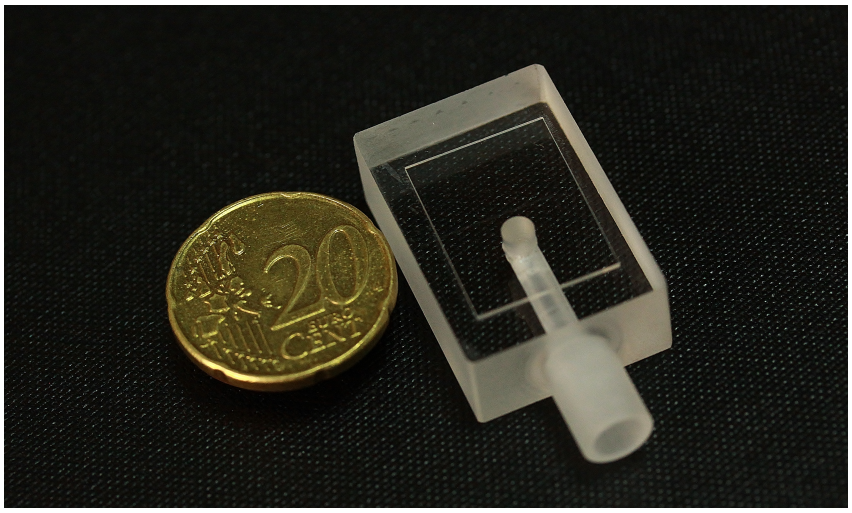

Figure 7.10: Optically contacted base plate and top plate, with a 20 cent piece for size comparison

loaded with liquid rubidium as discussed in section 7.2.3. This stage is also outlined on the bottom row of Fig. 7.9. To allow Rb vapour to flow from the reservoir to the science chamber, the custom stainless steel piece from the prototype was adapted to be made of fused silica.

The piece, shown in Fig. 7.10 and is referred to as the 'base plate'. It is a 20×30×10 mm block of ultrasonically machined fused silica, with an 8 mm external diameter tube protruding from the front face to allow for connection to a quartz loading manifold. Running from the front face to the top surface is a 3 mm diameter tube. An etched fused silica slide, called the 'top plate' is optically contacted to the top surface, so the top surface requires an extremely high quality polish finish, with a surface roughness $R_A < 1$ nm. The base plate is manufactured by GPE engineering

The plasma etched pattern on the windows is also altered, as seen in Fig. 7.11a. In order to minimise bowing of the flat plates due to pressure differentials, the etched region was split into 3 smaller regions of depth 1, 0.75 and 0.5 microns connected by a 1 micron deep trench to allow Rb to flow between each chamber. The smaller area of each chamber reduces the force applied to the chamber and therefore the amount of bowing, modelling using Kirchoff-Love theory for rectangular plates is shown in Fig. 7.8. The figure demonstrates the new expected length variation from atmospheric pressure on the cell windows should be less than 20 nm.

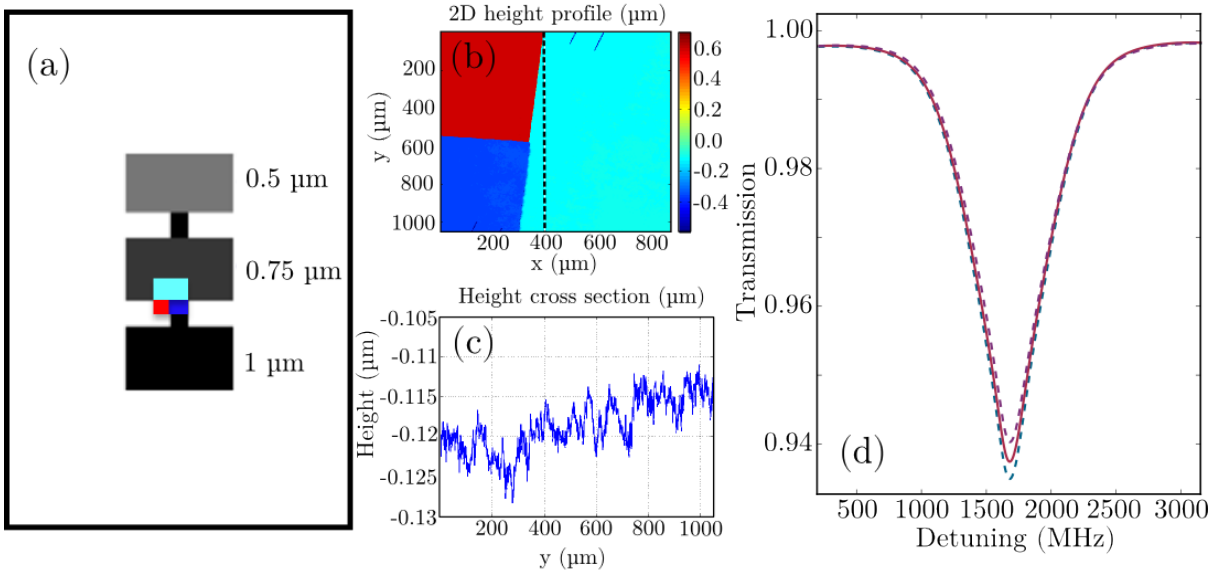

Figure 7.11: (a) Etch mask used for top plate to create ultra-thin region, with areas probed by AFM highlighted. (b) AFM image of etched region, taken at the point highlighted in panel (a). Data courtesy of Benjamin Greer. (c) Cross section detailing surface roughness across black dotted line from panel (b). (d) Change to transmission of the ^{85}Rb $F_g = 2$ transition for change in surface roughness inside the cell for a cell length of 0.745 μm (dashed purple line), 0.7 μm (solid black line) and 0.755 μm (dashed blue line). The overall theoretical change in transmission for a change of 5 nm is less than 1%.

The surface roughness inside the etched windows was also measured using atomic force microscopy (AFM), with the results shown in Fig. 7.11b. A plot of the variation in surface roughness across the black dotted line in panel (b) is shown in Fig 7.11c, showing that variations in surface roughness inside the cell are less than 5 nm, just 1% of the expected final minimum cell length. This level of surface roughness is similar to that of cells used for experiments described earlier in this thesis and hence should not impact measurements made inside the cell.

Alterations to the transmitted line-shape are modelled in Fig. 7.11d. The expected line-shape for the ^{85}Rb $F_g = 2$ transition for a cell length of 0.7 μm is plotted as a solid red line. The line-shapes for lengths of 0.745 and 0.755 μm are plotted as purple and blue dashed lines respectively. The change in peak transmission varies by 1%, and variations due to interior reflections are minimal. These changes are within the usual signal-to-noise ratio of spectra, so fitting is not expected to be affected.

7.3.4 Forming the optical contact bond

The procedure used for OCB is outlined in yellow on Fig. 7.9. The first step is surface preparation. Substrates to be bonded are purchased with a sufficiently high quality, $R_A < 1$ nm, and are first cleaned in an ultrasonic water bath to initially remove surface contaminants left over from machining methods. The OCB process is undertaken in a clean room to avoid dust contaminants from settling on the surface, the steps performed in a clean room are highlighted in yellow boxes on Fig. 7.9. Immediately prior to bonding, surfaces are first cleaned with HPLC (high purity) acetone, then HPLC isopropyl alcohol (IPA). In between cleaning steps, the surface is dried with a stream of compressed N_2 to prevent any residue forming on the surface. Residue left on the surface can be identified by visual inspection, appearing as smears and patches of lower reflectivity.

The surfaces to be bonded are then placed on either side of a lens tissue. Using fingers, light pressure is applied to either side of the interface to be bonded. Some pressure should be applied, but not so much that the substrates to be bonded bend significantly, as this will reduce the amount of area in contact, resulting in a lower quality bond. Whilst light pressure is being applied, the lens tissue is pulled out. The lens tissue adds a small static charge in between the two plates, assisting the initial formation of the bond. If successful, a bonded area can be observed. The bonded area is clear, and surrounded by interference fringes where the bond has not formed. Voids where contaminants or surface imperfections are present can also be identified by the interference fringes.

The bonded area can be increased by applying pressure at the edge of the bond interface. If the bond has formed, but is not of a sufficiently high quality, e.g. if there are too many voids or the bonded area is too small, the surfaces can be pulled apart and the bonding process can be repeated. The surfaces may need to be cleaned again with acetone and IPA after several failed attempts.

The cell is then heated to 1100°C to form a permanent bond and is then ready for loading. During the heating phase, voids can both appear or increase in size, depending on the bonding temperature used. Causes of this include the diffusion of water away from formed siloxane bonds as discussed in section 7.2.1, but also from hydrocarbon residue on the surface that has survived the cleaning process. This second problem can potentially be remedied by including a cleaning stage with warm nitric acid to remove such hydrocarbons [17]. Other voids can also disappear based on the length of time the

bonded plates are annealed for. Longer times result in more diffusion of trapped gases, reducing the size of voids [17].

7.3.5 Loading with Rb

The cell is then ready for loading with liquid Rb, using the methods outlined in section 7.2.3. Importantly, alkali vapour cells that are regularly cycled in temperature should not have a graded seal (e.g. from fused silica to borosilicate) included in their final construction. The stresses induced in the seal by chemical attack from the vapour and thermal shock from regular cycling of heating and cooling result in failure of the joint, observed in early prototypes of the cell fabricated in Durham.

For the loading stage, the cell has an extended 8 mm outer diameter quartz tube attached to the base plate which can be connected to fused silica tubing that will form the cell reservoir. The tubing is then narrowed to allow the fused silica reservoir to be sealed off from atmosphere after the cell has been loaded with Rb. The fused silica tubing is then connected via a graded seal to borosilicate tubing. The location of the graded seal is marked on Fig. 7.9. The seal is placed below the narrowed region to avoid the failure of graded seals discussed earlier. The rest of the loading manifold is made of borosilicate for ease of workability in making and manipulating the manifold. The process then follows that outlined in section 7.2.3.

The final result, shown in Fig. 7.12a is a cell made entirely of fused silica, loaded with pure Rb with 3 science chambers of length 0.5, 0.75 and 1 micron. These areas can be identified in Fig. 7.12a as coloured rectangular areas. The colour is caused by thin film interference inside the science chambers from the white light illuminating the cell. The colour variation indicates length variations inside the cell, which will be measured and explored in the next section. The photograph in Fig. 7.12a was taken after 2 months of usage and demonstrates slight browning of the walls of the delivery channel that connects the cell reservoir to the science chambers. This is Rubidium oxide formed on the walls due to high temperature induced reaction between the Rb and the cell walls.

Fig. 7.12b shows a zoom of the cell chamber, highlighting the length variation in the cell. It also shows the quality of the OCB achieved; most of the top plate surface is bonded, with minimal fringes at the edge and only 2 small voids near the science chamber.

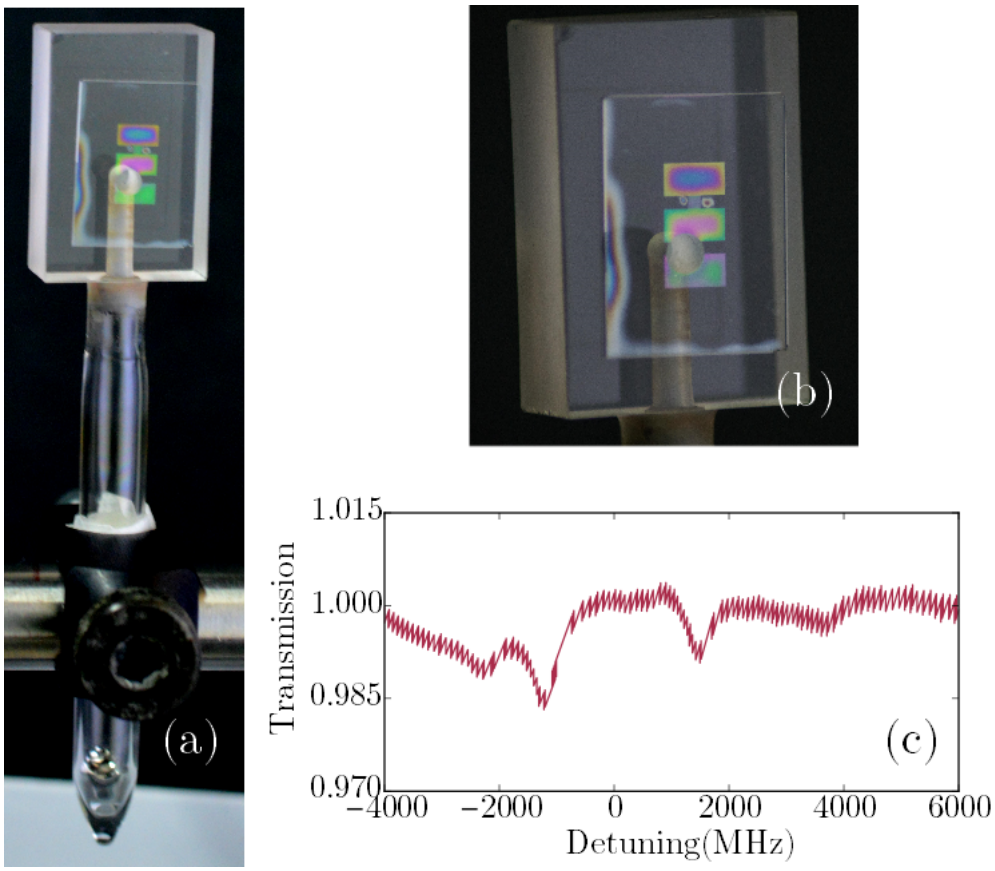

Figure 7.12: Second prototype cell fabricated in Durham. (a) Full cell after 2 months of use, of note is the slight browning in the delivery channel. (b) Zoom of science chamber region, highlighting change in colour for each different chamber length and voids in OCB. (c) Initial signature from cell at 120° C demonstrating clear Dicke narrowed peaks.

In order to confirm the initial functionality of the cell, single beam transmission spectroscopy was performed, resulting in the first spectra from the cell, shown in Fig. 7.12c. The spectra was taken from the 0.75 μm region, and displays the features expected for a thin cell spectrum- relatively small absorption with Dicke narrowed peaks. The functionality of the cell will be further demonstrated in the next section.

7.4 Testing

In order to determine if the cell is operating as expected, we perform several tests. Utilising our model from chapter 3 describing the cell transmission for known lengths and

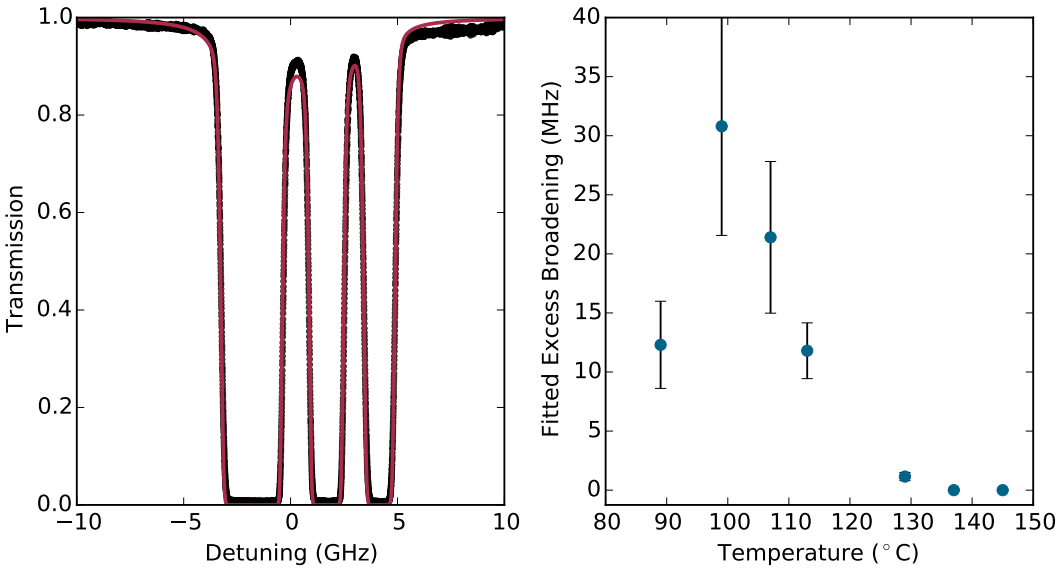

Figure 7.13: (a) Sample fitted data for a temperature T = 99 °C and Γ_{ex} of 11.8 MHz. Taken from the 6.5 mm length channel in the cell. (b) Temperature dependence of fitted Γ_{ex}

temperatures, we are able to use fitting to ascertain if the cell response matches the theoretical response.

In addition, the tube connecting the cell to the reservoir also lies in the optical path. With an optical path length of 6.5 mm, spectra acquired from this region can be modelled using ElecSus [26], a powerful fitting program developed in Durham that can be used to fit spectra from longer cell lengths. Its high accuracy means that it can be used to determine the presence of buffer gases.

7.4.1 Cell Atmosphere

The quality of the cell atmosphere is paramount to the success and lifetime of the cell. For cells fabricated herein, the intended atmosphere is a high vacuum occupied only by Rb vapour. The cell is permanently sealed after loading, so atmospheric purity can only be inferred.

To test for the presence of contaminant gases, we use line-width measurements. If excess gases are present, lines will be broader than expected from inter-atomic collisions between Rb atoms. This broadening is caused by extra collisions between Rb and non-Rb atoms,

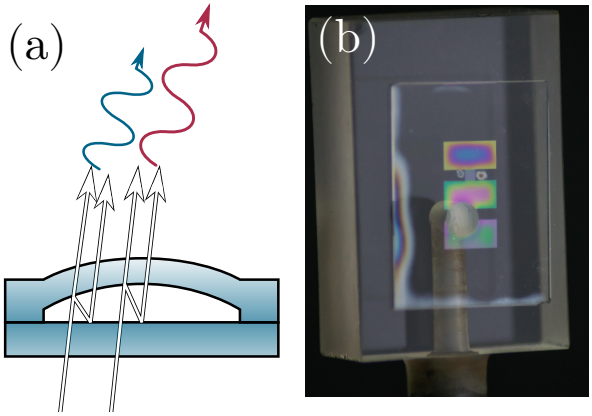

Figure 7.14: (a) Length dependent constructive interference of white light incident inside the cell. (b) Photograph of thin film interference observed inside the cell.

similar to collisional broadening described in chapter 2. The collisions further shorten the atomic lifetime, therefore broadening the spectral lines.

To measure increases in line-width, we apply fitting methods similar to those used to characterise the atom-surface interaction in chapter 5. However, spectra are taken from the vapour channel perpendicular to the surface to the cell. This channel is 6.5 mm long in the direction of beam propagation, and hence we can use ElecSus [26], discussed in the previous section, as the channel length is too long for nanocell effects to have significant impact on the line-shape. If excess gases are present, an increase in temperature will result in an increased broadening as more collisions will be taking place.

The temperature dependence between 86 to 146°C are plotted in Fig. 7.13a. Each spectra was fitted for excess broadening Γ_{ex} using ElecSus, with the results plotted in Fig. 7.13b. Excess Γ_{ex} are minimal, with absolutely no increase with temperature. The larger broadenings at low temperature can be attributed to background variations in the laser amplitude interfering with measurements, evidenced by the large errors associated with those measurements. Hence it can be concluded that the cell atmosphere is sufficiently pure for our purposes.

7.4.2 Length measurements

Due to the length variation of the windows, measurement of the cell length in the optical path is essential. Unfortunately, the cell design does not accommodate standard length

measurement detailed previously in this work. The top plate of the cell is very thin (0.5 mm) and so back reflections from the front and interior surfaces of the cell cannot be resolved.

Measurement of length is paramount for performing experiments with the fabricated cell. Much analysis is done via inspection and fitting of spectra from the cell. Fitting of spectra requires a length measurement because temperature cannot be directly probed, only estimated from measurements of the external cell temperature and later fitting for an exact vapour temperature. When fitting there is a large crosstalk between fitted length and temperature parameters; both parameters have strong effects on the overall transmitted line strengths. Hence to improve the quality of fits our results rely on accurate length measurements, removing length as a fitting parameter.

Additionally, with inspection of the cell windows, it appears that the windows are not concave, as expected if the plates were bowing inwards from external atmospheric pressure, but are instead convex. This can be seen when considering thin film interference inside the cell, illustrated in Fig. 7.14a. White light entering the cell reflects multiple times within the cell, with different wavelengths destructively or constructively interfering depending on the cell length. For example, where the science chamber appears red, it is indicative of a length that is an integer multiple of 650 nm. This effect is only visible in thin films, as at a longer lengths each length can be a multiple of many wavelengths and hence multiple wavelengths can be transmitted, eventually resulting in the full spectrum being transmitted.

If the cell windows were concave, as expected, thin film interference inside the science chamber would have a colour variation moving from the red end of the spectrum at the edges where the cell is thickest, moving towards the blue end in the centre where the cell length is expected to be minimal. However, we can see from images of the cell windows in Fig. 7.14b that the opposite is the case, indicating that the windows are convex. We can also estimate from these images that the length variation is a few hundred nm in magnitude, as the full optical spectrum is not observed or repeated in any of the cell windows. However, this change in length is still far greater than the 20 nm length variation predicted for the rectangular plates modelled using Kirchoff-Love plate theory in Fig. 7.8.

Furthermore, by taking the minimum of transmission spectra across the science chamber,

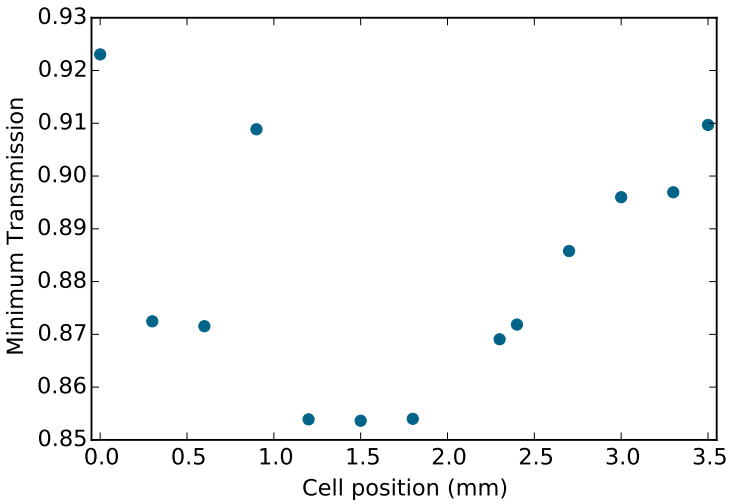

Figure 7.15: Change in minimum transmission as the probe beam (λ=780 nm) is moved laterally across the cell science chamber. Minimum transmission decreases towards the centre of the cell, indicating that it is increasing in length.

shown in Fig. 7.15, minimum transmission decreases towards the centre of the cell, again indicating a longer optical path length in the centre of the cell as more absorbing medium is present.

Using a single wavelength, the ratio between reflections from the front and interior of the cell is measured, similar to cell length measurement used in chapter 5 and outlined in appendix A. This was initially tested in the cell by adding thick fused silica plates coated with refractive index matching oil to the front of the cell. The index matching oil removes any reflections from the interfaces between where the additional plate meets the cell, allowing for standard measurement to be performed. The expected change in ratio for 780 nm incident light is plotted in Fig. 7.16 as a red line. However, the signal is sinusoidal, meaning that without an initial known length to use as a reference point, an absolute length measurement cannot be made. We introduce a second wavelength of 532 nm, colinear through the cell with the 780 nm beam, before being split and separately detected after interactions inside the cell. The expected change in intensity ratio for the 532 nm beam is plotted as a green line on Fig. 7.16. Using the second wavelength it possible to increase the accuracy of the measurement, as there are a reduced amount of points where the ratio of reflections for the two wavelength coincide but some uncertainty remains. Therefore, this method still cannot return a sufficiently accurate

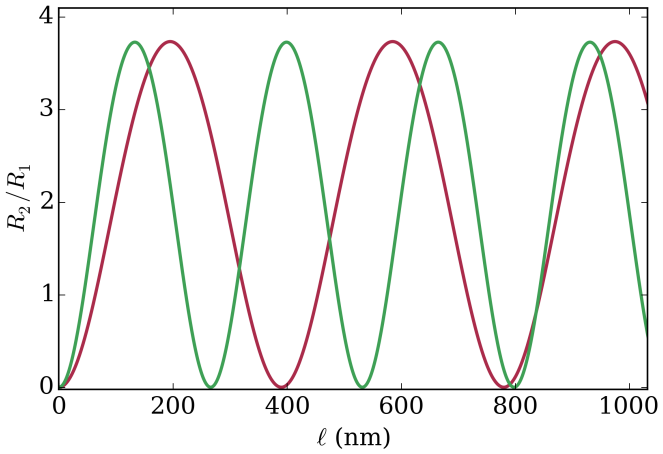

Figure 7.16: Intensity ratios for back reflections from the front window (R_1) and interior cavity (R_2) of an ultra-thin cell for wavelengths of 780 nm (red line) and 532 nm (green line).

length measurement.

As standard measurement cannot be used, we use an alternative method of length measurement. The experimental set-up is shown in Fig. 7.17c. White light generated by a white LED is first propagated over a few metres, before being sent though an aperture to collimate the light. It is then combined with the probe laser beam on beam-splitter BS1 and focussed into the region to be measured. The transmitted output is sent to a spectrometer with a wavelength range of 400-700 nm. A reference spectrum of the light before it is transmitted though the cell is taken and automatically subtracted from the transmitted white light spectrum by the spectrometer's analysis program. The resultant signal is a set of wavelength dependent Fabry-Perot (FP) peaks. This method measures several hundred wavelengths simultaneously, limited only by the resolution of the spectrometer, vastly increasing the accuracy of our measurements.

The expected transmitted signal for a 10 μm length cell is shown in Fig. 7.17a. The etalons are modelled assuming normal incidence, but include a wavelength dependent refractive index $n(\lambda)$, calculated using the Sellmeier equation with the appropriate coefficients for fused silica taken from [27]. There are many interference fringes in Fig. 7.17a, which will result in a clear peak in a Fourier transform of the spectrum- an easy method of inferring the cell length for μm scale cells.

For ultra-thin cells fabricated in this work, the free spectral range (FSR) is on the order of hundreds of nm, so only a few fringes can be observed, modelled in Fig. 7.17b. However,

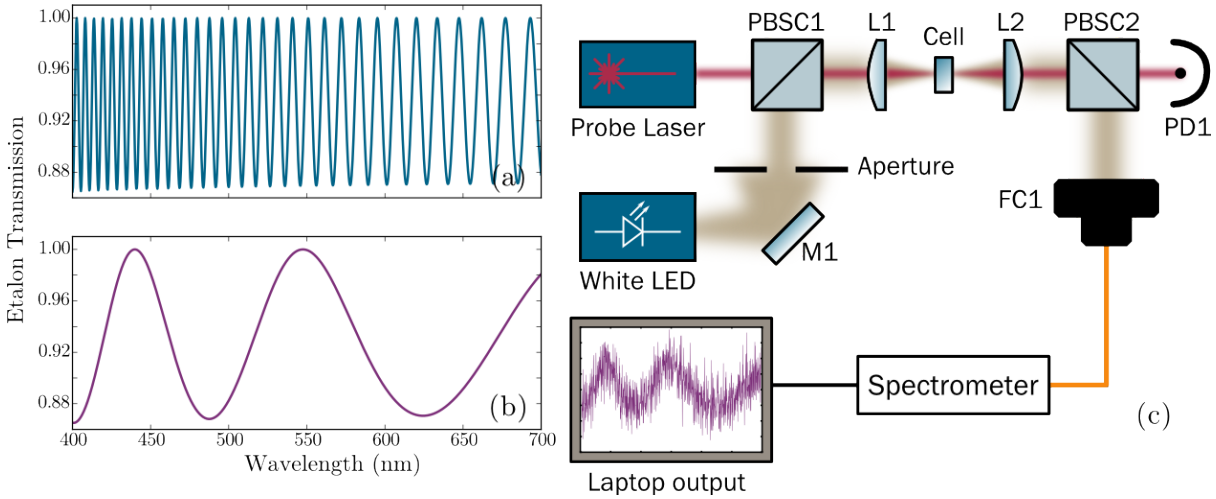

Figure 7.17: (a) Expected etalon for a 10 μm length cell (b) Expected etalon for an 0.5 μm length cell. (c) Experimental set-up used to measure cell length.

these can still be fitted to extract meaningful results. We fit the resulting fringe with a λ dependent Fabry-Perot etalon function:

$$\mathcal{T} = \frac{1}{1 + F\sin^2(2n(\lambda)kL)}, \tag{7.1}$$

where $F = 4R/(1-R)^2$ and R is the reflection coefficient of the fused silica. We then fit the spectrometer signals for the cavity length. A sample fit is shown in Fig. 7.18a, taken from the 0.75 μm region. The blue line shows the background signal, with no cell present. The green line is the transmitted signal through the cell science chamber. The red line is the fitted Fabry-Perot function. As a result, we can measure the position dependent optical path length across the entire cell, as shown in Fig. 7.18b. The fitted etalon lengths match well with thin film interference patterns observed inside the cell- the increased length at site numbers 4-6 correspond to the area of the science chamber near where the vapour channel connects to the cell science chamber. As can be seen from inspection of the middle chamber on Fig 7.14b, the length variation in this area does not appear symmetrical. This asymmetry is reflected in the fitted lengths inferred from the white light signals.

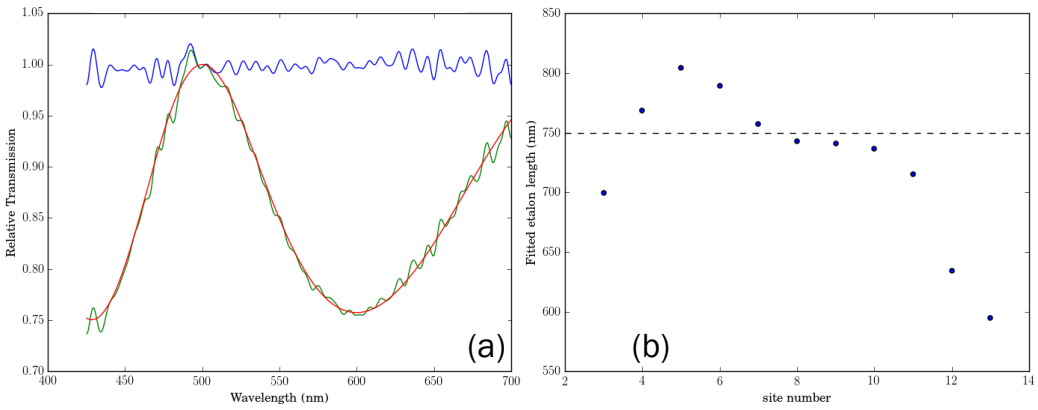

Figure 7.18: (a) Sample fitted white light etalon from central cell science chamber, expected $L = 750$nm. (b) Lengths inferred across centre of 750 nm science chamber. Data courtesy of Will Hamlyn.

Hence, we have demonstrated that the cell windows are certainly convex with respect to the top surface. This structure could be a result of changes in the cell windows during the high temperature heating phase of the optical contact bonding process. The poor heat conduction of fused silica results in a temperature gradient between the front and interior surfaces [23]. This gradient combined with the stress induced by the shape of the science chambers, small rectangular areas with strong bonded edges could have caused the cell windows to push outwards. Another possible cause is gases trapped inside the ultra-thin region expanding during heating, pushing the softened fused silica windows outwards.

The convex windows has only been observed in cells with the modified window structure (several small interconnected chambers instead of one large etched region). Hence, stresses induced by the cell window structure combined with temperature gradients within the glass are the most likely cause of this phenomenon.

With a successful measurement system for cell windows, we are now able to measure vapour susceptibilities and fit spectra from the ultra-thin region of the cell. We next look at the temperature dependent behaviour in the cell to confirm if dynamics in the cell evolve as expected.

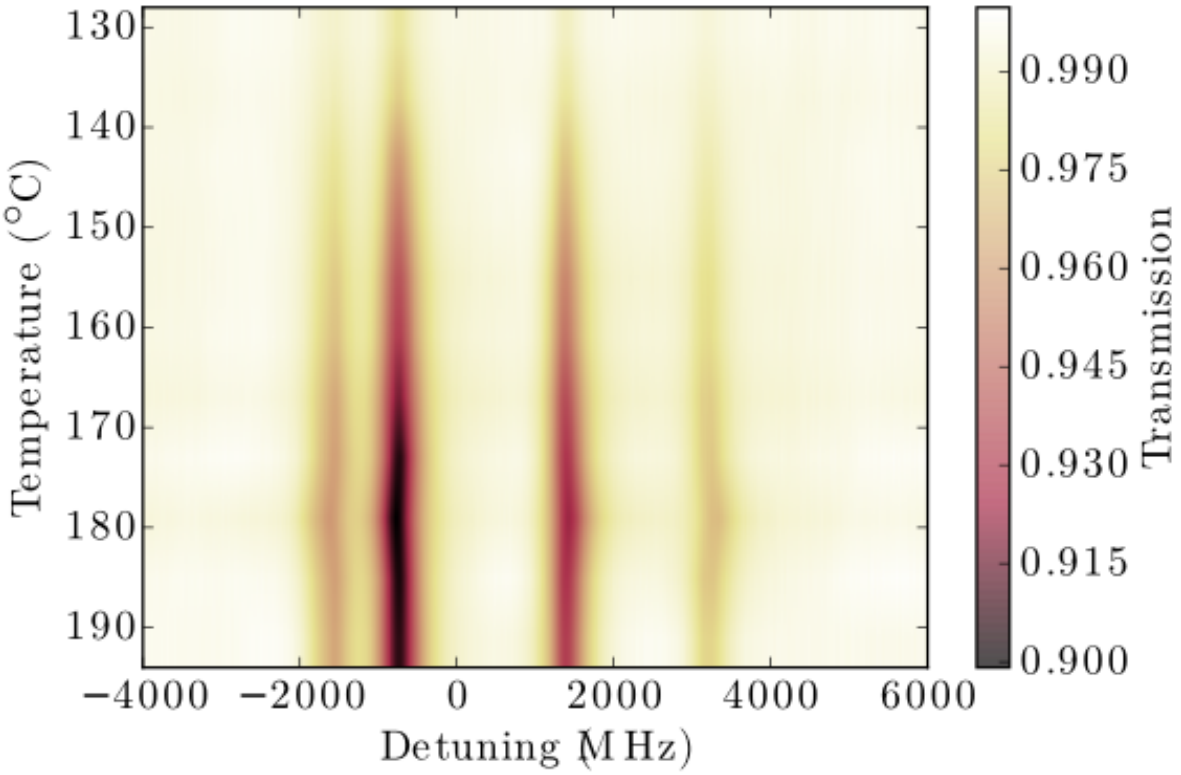

Figure 7.19: Temperature dependence of transmission spectra taken from the 750 nm length science chamber.

7.4.3 Temperature dependence

With accurate length measurements of the cell, we can fit spectra to confirm that dynamics in the cell evolve as expected. Measuring the evolution of the atomic spectra with temperature and fitting them will confirm if the atomic response is consistent with experiments performed in other cells.

The evolution of spectra taken in the 750 nm length science chamber is shown in Fig. 7.19. On a quick inspection, dynamics evolve as expected, with increasing absorption of the beam as the density of atoms increases. Fitting these spectra using the model outlined in chapter 3 yields some promising results, plotted in Fig. 7.20a. Fits are taken from a dataset where the temperature is kept constant, and the length of the cell is changed. Fit results return a somewhat consistent temperature, but one that is much lower than expected, and varies over 15°C. We can expect a disagreement of a few degrees, as reservoir temperature is measured externally. However, the departure from measured temperature

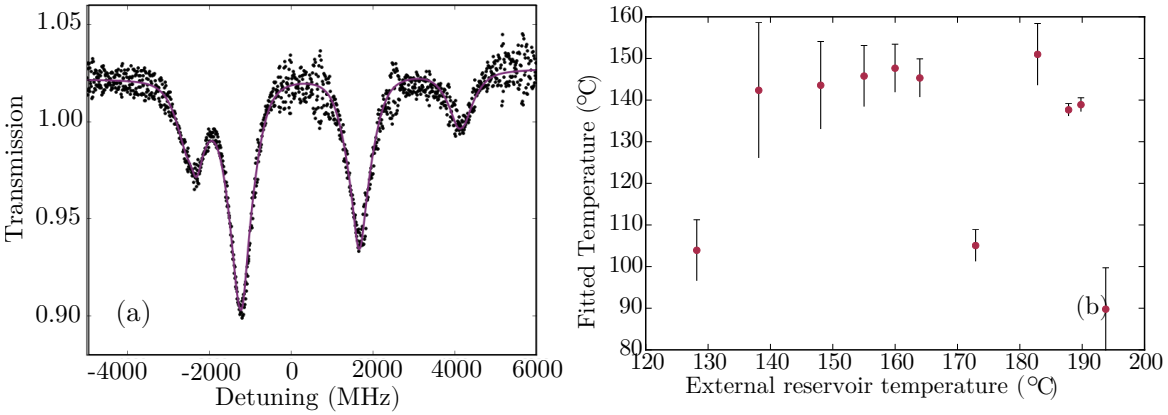

Figure 7.20: (a) Sample of fitted spectrum, with experimental data plotted as black point and the fit plotted as a purple line, taken for a cell length of 778 nm (b) Comparison of the fitted temperature versus the measured external temperature. The difference is far larger than expected.

exceeds 20 degrees, indicating that dynamics inside the cell are not evolving as expected.

To investigate further, the results from the dataset plotted in Fig. 7.19 were fitted for temperature. Using length measurement obtained in the previous subsection, these spectra were fitted for temperature T, taken from the fit accounting for kinetic and density induced broadening. The results are presented in Fig. 7.20 (b). It compares the fitted temperature, to the measured external reservoir temperature. Fitted T are consistently significantly lower than measured T.

This could be indicative of reduced diffusion of atoms inside the cell. It is well known in vacuum technology that atoms do not diffuse well around corners, as only specific atomic trajectories can move around them, with other trajectories reflecting off walls and returning to the reservoir. Atoms in the nanocell must diffuse around into an extremely narrow gap, which possibly limits the number of atoms entering the cell chamber.

Furthermore, we must consider how atoms travel between each science chamber. Diffusion of atoms between cell chambers could be reduced by the channels leading between each chamber. Only atoms travelling along extremely limited trajectories are able to move between cell chambers.

The solution to these problems could be an improved cell design, where the reservoir sits directly beneath the science chamber entrance, reducing the amount of corners atoms

must diffuse around. This could be achieved with the current design by shortening, or entirely removing the reservoir stem, instead distilling the Rb into the vapour channel leading between the reservoir and the science chamber. Alternatively, a reservoir channel could be cut into the baseplate below where the cell science chamber, again improving atomic diffusion. Both solutions would additionally make the cell more compact, making it easier to integrate into experiments and other applications.

7.5 Improvements for future designs

As discussed, changing the location of the reservoir would improve vapour pressures inside the cell, which currently appear to be subnormal. Furthermore, increasing the area and depth of the cell chambers could also increase diffusion of atoms inside the cell, resulting in more reliable vapour pressures.

Specific additions that are planned to be made to the cell are the inclusion of solid immersion lenses on the outer windows, allowing for extremely tight focussing of light inside the cell. With a sufficiently high numerical aperture lens, excitation volumes of less than λ^3 could be achieved because of the cells extremely short length. If we use the extremely sensitive off-axis scattered photon spectroscopy method outlined in chapter 5, this could lead to acquisition of spectra from single atoms inside the cell. This prospect is particularly enhanced by the fact that the lack of glues used in construction of the cell means that there is complete optical access from all sides of the cell, with no other materials aside from fused silica and the atoms inside the cell contributing to the signal.

Lenses embedded in the front cell window would need to match the material of the window itself, so focussing could be further improved by using a material with a higher refractive index, such as sapphire ($n = 1.8$) or diamond ($n = 2.4$). Both materials are suitable for optical contacting, providing they are sufficiently polished, but cannot be manipulated using glass-blowing techniques and hence other loading methods such as use of AMDs will need to be be considered. Both sapphire and diamond also have much higher chemical resistances and would mean the cell could be heated up to much higher temperatures.

7.6 Outlook

In this chapter we have discussed the successful fabrication of functional alkali-metal vapour cells that are still operational after 8 months of usage. The basic cell design can now be adapted to alter the interior of the cell, including small micron scale channels in the substrate in order to study atomic diffusion in extremely confined geometries, and to study the behaviour of atoms under extremely tight confinement in 2 dimensions, and for the development of an atomic wave-guide.

Other possibilities include developing an all sapphire cell by adapting the current cell fabrication methods. However, this requires an alternative sealing method. One possible method could be to construct a cell chamber with an exit channel which is temporarily mounted on a quartz or borosilicate base plate via an OCB that will not be made permanent. The base plate can then be connected to a standard loading manifold allowing Rb to be distilled into the cell. The cell could be sealed off using the bowing of the plates under vacuum. If the cell is designed with a sufficient area such that the bowing of the plate exceeds the depth of the cell, contact will be made between the two plates. This can then be made permanent by localised heating with a high powered laser [28].

Further possibilities include the addition of metallic structures inside the chamber. However, optical contact bonding may not be a suitable bonding method in this case, as the extreme temperatures required would destroy the metallic nanostructures.

Finally, a very easy alteration to the cell could be the addition of high numerical aperture lenses on the cell windows themselves, resulting in extreme focussing inside the cell. If diffraction limited spot sizes can be reached, with the current cell lengths achieved, the excitation volume would be much less than λ^3, allowing the study of extremely small excitation volumes and possible detection of single atoms in a thermal vapour cell.

In summary, the success of this cell fabrication project has opened up many new avenues of research. Future work in Durham on the fabrication of cells will concentrate on the inclusion of high NA lenses and increasing the atomic confinement.

Bibliography

[1] S. Ghosh, J. E. Sharping, D. G. Ouzounov, and A. L. Gaeta, Phys. Rev. Lett. **94**, 093902 (2005).

[2] S. Villalba, A. Laliotis, L. Lenci, D. Bloch, A. Lezama, and H. Failache, Phys. Rev. A **89**, 023422 (2014).

[3] L. Stren, M. Grajower, and U. Levy, Nat. Comm. **5** (2014).

[4] W. C. Griffith, S. Knappe, and J. Kitching, Opt. Express **18**, 27167 (2010).

[5] A. Horsley, G.-X. Du, and P. Treutlein, New J. Phys. **17**, 112002 (2015).

[6] J. Keaveney, A. Sargsyan, D. Sarkisyan, A. Papoyan, and C. S. Adams, J. Phys. B **47**, 075002 (2014).

[7] S. Knappe, V. Shah, P. D. D. Schwindt, L. Hollberg, J. Kitching, L.-A. Liew, and J. Moreland, Appl. Phys. Lett. **85** (2004).

[8] L. Weller, K. S. Kleinbach, M. A. Zentile, S. Knappe, I. G. Hughes, and C. S. Adams, Opt. Lett. **37**, 3405 (2012).

[9] L. Nieradko, C. Gorecki, A. Douahi, V. Giordano, J. C. Beugnot, J. Dziuban, and M. Moraja, J. Micro-Nanolith Mem. **7**, 033013 (2008).

[10] L.-A. Liew, S. Knappe, J. Moreland, H. Robinson, L. Hollberg, and J. Kitching, Appl. Phys. Lett. **84**, 2694 (2004).

[11] Y. Pétremand, C. Affolderbach, R. Straessle, M. Pellaton, D. Briand, G. Mileti, and N. F. de Rooij, J. Micromech. and Microeng. **22**, 025013 (2012).

[12] R. Deschner, H. Kubler, R. Low, H. Baur, N. Fruhauf, and T. Pfau, Appl. Phys. Lett. **105** (2014).

[13] R. Ghodssi and P. Lin, *MEMS Materials and Processes Handbook* (Springer US, New York, 2011).

[14] T. T. Veenstra, J. W. Berenschot, J. G. E. Gardeniers, R. G. P. Sanders, M. C. Elwenspoek, and A. van den Berg, J. Electrochem. Soc. **148**, G68 (2001), http://jes.ecsdl.org/content/148/2/G68.full.pdf+html.

[15] H. I. Smith, J. Acoust. Soc. Am **37** (1965).

[16] M. Shimbo, K. Furukawa, K. Fukuda, and K. Tanzawa, J. Appl. Phys. **60** (1986).

[17] X. X. Zhang and J. P. Raskin, J. Microelectromech. S. **14**, 368 (2005).

[18] A. Castex, M. Broekaart, F. Rieutord, K. Landry, and C. Lagahe-Blanchard, ECS Solid State Lett. **2**, P47 (2013).

[19] R. K. Rajput, *A Textbook of Manufacturing Technology: Manufacturing Processes* (Laxmi Publications, New Dehli, 2007).

[20] D. R. Scherer, D. B. Fenner, and J. M. Hensley, J. Vac. Sci. Technol. A **30**, 061602 (2012).

[21] J. A. Rushton, M. Aldous, and M. D. Himsworth, Rev. Sci. Instrum. **85**, 121501 (2014).

[22] Optical Materials **35**, 843 (2013).

[23] A. Roth, *Vacuum Sealing Techniques*, AVS Classics in Vacuum Science and Technology (Springer US, New York, 1994).

[24] J. J. Deluca, *Bonding of sapphire to sapphire by eutectic mixture of aluminum oxide and zirconium oxide* (1975).

[25] J. N. Reddy, *Theory and Analysis of Elastic Plates and Shells, Second Edition*, Series in Systems and Control (Taylor & Francis, 2006).

[26] M. A. Zentile, J. Keaveney, L. Weller, D. J. Whiting, C. S. Adams, and I. G. Hughes, Comp. Phys. Comm. **189** (2015).

[27] M. N. Polyanskiy, *Refractive index database* (2016), URL http://refractiveindex.info/.

[28] R. M. Carter, J. Chen, J. D. Shephard, R. R. Thomson, and D. P. Hand, Appl. Opt. **53**, 4233 (2014).

Chapter 8

Conclusions

Thermal vapour cells have much to offer to the field of atomic physics, allowing us to investigate many fundamental properties of atoms as well as being an excellent basis for new devices. This thesis has discussed how nanocells have contributed to this field, and discussed a methodology for creating them that can potentially be replicated by anyone interested in extending the study of nanocells even further.

The work has been split into three sections discussing various aspects of nanocells. The first part including chapters 2 and 3 built a theoretical framework for the systems discussed in this thesis. Chapter 2 takes the atomic coherence for an optical Bloch model of a 2 level atom to model the frequency dependent electric susceptibility that models the natural line-shape of an atom. The model is then included to involve further effects that alter the line-shape such as Doppler broadening from thermal motion of the atoms and self broadening from inter-atomic collisions. It then gathers all of these effects into a model for the frequency transmission of light through an atomic vapour.

Chapter 3 takes the model built in chapter 2 and expands it to include effects only observed in nanocells. The dominant effect on the line-shape is a suppression of the Doppler broadening called Dicke narrowing. Atoms with a high velocity in the direction of beam propagation only interact for a relatively short time and so their contribution to the final signal is greatly reduced, resulting in Lorentzian line-shapes. We discuss how Dicke narrowing is modelled using results from a Monte-Carlo simulation of atomic trajectories to justify its use. Another effect only observed in ultra-thin cells is the interaction of atoms with nearby surfaces. Atoms will always interact when they are

within a few hundred nm of a surface, but in longer cells the proportion of absorbing atoms experiencing this effect is negligible. When all atoms are within range of this a strong red shift and asymmetry of the line-shape is observed. Finally, the mixing of transmitted and reflected line-shapes is discussed. Again, this is an effect that is present in all atomic line-shapes, but is only observed in transmitted spectra that have a very small signal such as those form nanocells. All of these effects are added to the model of frequency dependent transmission built in chapter 2 resulting in a highly accurate model that is used to verify experimental results throughout the thesis.

Chapter 4 explores the application of the Hilbert transform to atomic spectra. The chapter proves that the Hilbert transform is directly equivalent to the Kramers-Kronig (KK) relations, which are used to relate the real and imaginary components of a function. The KK relations are used in atomic physics to infer the refractive index, derived from the real component of the electric susceptibility from a transmission spectrum, derived form the imaginary component. However, the KK relations are complex to implement, unlike the Hilbert transform which is implemented in many programming languages. It operates 10^4 times faster than the KK relations and can be used to quickly map out the refractive index and its derivatives.

The latter half of the chapter explores how it can be applied to physical systems. It is first used to map out the frequency dependent refractive and group refractive index response of Cs D1 spectra in the nanocell across a wide variety of temperatures. Results were quickly generated from old datasets and gave new insights into the medium, allowing us to pinpoint the ideal parameters to perform propagation experiments with. The Hilbert transform was then applied to other experimental systems including a mm length thermal vapour cell and an ultra-cold MOT, where rearranging the experiment to measure refractive index would be impractical. The refractive index inferred matched extremely well with theoretical expectations and demonstrates the applicability of the Hilbert transform across many areas of atomic physics.

Part 2 of the thesis discusses experiments performed in the nanocell. Chapter 5 examines the atom-surface (AS) interaction in further detail. Using the model developed in chapter 3, the form of the power law governing the AS interaction in the range of 40-100 nm is measured. We also measure the coefficient governing the strength of the AS interaction, although analysis of simulated annealing fitting results shows that fitting of spectra is not

an ideal method to measure the strength coefficient as the variation of the goodness of fit parameter of a wide range of values is too low. However, the analysis of the variation of goodness of fit of exponent results shows that fitting is an excellent method to determine the power law of the AS interaction.

A particular highlight in this chapter is the experimental methods. The use of single photon counting modules to detect off-axis scattered light generated by photons scattered after interaction with a laser beam scanning across the Rb D2 line results in a highly sensitive data acquisition method. We were able to acquire spectra where transmission would have been less then 0.1%, allowing us to take spectra from extremely thin cell regions (down to 40 nm) at reduced temperatures (down to 80°C). This resulted in spectra from a single beam where all hyperfine states can be resolved, owing to extreme Dicke narrowing of the spectral lines. Extensions of this experimental technique could include the study of bound states or to study absorption spectra from single atom sources.

We then study coherent dynamics in chapter 6. We study the time evolution of a vapour confined in a nanocell when excited by a high power pulse with a FWHM of 800 ps. The pulse drives population oscillations, called Rabi oscillations between a ground and excited state, whilst being simultaneously monitored on a separate probe state. Owing to the nanocell's reduced optical depth, we are able to drive and monitor Rabi oscillations in previously inaccessible high density regimes. The results did not agree with a optical Bloch simulation of the system, with rise times and peak response times that are consistently faster than expected. We conclude that a simple optical Bloch simulation is insufficient to model the dynamics occurring inside the cell.

An extended Maxwell-Bloch simulation was performed by Thomas Ogden that simulates not only the population dynamics but also propagation effects inside the cell. The theoretical results have an excellent agreement with the experimental results, and also strongly indicate the formation of simultons; simultaneously propagating optical solitons. However, the cell length used is too short to demonstrate full pulse splitting that would confirm the presence of optical simultons, and so future work in this area will focus on propagation of a pulse through a medium that is 10 μm thick.

The final part of this thesis, containing only chapter 7 discusses the fabrication of nanocells. We seek a method of fabricating nanocells that can be custom tailored for specific experiments. The chapter first explores methods of fabrication, discussing meth-

ods used in MEMS vacuum encapsulation that could be applied to nanocells. It discusses and tests multiple fabrication options, including the use of glues and alkali-metal dispensers that could be used to fabricate nanocells.

Next several prototypes are described, starting from an initial modular prototype comprised mainly of steel vacuum parts, before it is refined to a fused silica cell constructed using a combination of optical contact bonding and scientific glass-blowing techniques. The final prototype is extensively tested, the length, temperature dependence and interior surface roughness of the cell is closely inspected. We utilise fitting of spectra to confirm that the cell is functioning properly, returning spectra that match with theoretical expectations as we vary the temperature. We also demonstrate a method of measuring the cell length using an analysis of white light transmitted through the cell, analysing the resulting Fabry-Perot etalon detected by a spectrometer to infer lengths between 500-1000 nm.

The final cell produced was a strong success, with the cell remaining functional after 18 months of use. However, analysis of the evolution of spectra with temperature indicate that the cell design restricts the flow of atoms between the cell reservoir and science chamber, so future cells will need to be modified to allow the alkali-metal vapour to flow freely between cell chambers. Future cell designs will start to incorporate high numerical aperture lenses that will allow extreme focusing inside the cell, possibly leading to single-atom detection inside a thermal vapour cell, especially if used in conjunction with the sensitive data acquisition methods outlined in chapter 5. With the groundwork described in this chapter, cell fabrication and experimentation in Durham has a bright future, that will certainly lead to some fascinating experiments and exciting collaborations.

Part IV

Appendices

Appendix A

Measuring Cell Length

Cell length is measured via back reflections from the front and interior surface of the cell, illustrated in Fig. A.1. A beam incident on the cell at a slight angle will reflect from the front cell window, first interior surface, second interior surface and the back cell window. The two interior surfaces have such a small separation that the back reflections appear as one spot. Hence, 3 back-reflected spots are observed form the cell, labelled on the figure as R_1, R_2 and R_3, demonstrated in the right hand panel of Fig. A.1.

As reflection R_2 is a combination of the reflection from both surfaces it is a sum of the two beams. They will interfere constructively or destructively dependent on the separation of the two surfaces at the point of interrogation. This therefore results in spot R_2 having an intensity that is dependent on that plate separation. This can be used to infer a length by measuring the intensity of R_2 relative to spot R_1, which has a constant intensity. The relation between the two follows:

$$\frac{R_2}{R_1} = \frac{(1-R^2)(F\sin(\phi/2)^2)}{R(1+F\sin(\phi/2)^2)}, \tag{A.0.1}$$

where R is the reflectivity of the cell surfaces, defined as

$$R = \left(\frac{n-1}{n+1}\right)^2. \tag{A.0.2}$$

Parameter n is the refractive index of the cell window material. Constant $F = 4R/(1-R)^2$ is the finesse of the interior cavity. The most important parameter in Eq. A.0.1 is ϕ, describing the phase difference of the two interfering beams from the interior cavity of the cell:

$$\phi = \frac{4\pi\ell}{\lambda}, \tag{A.0.3}$$

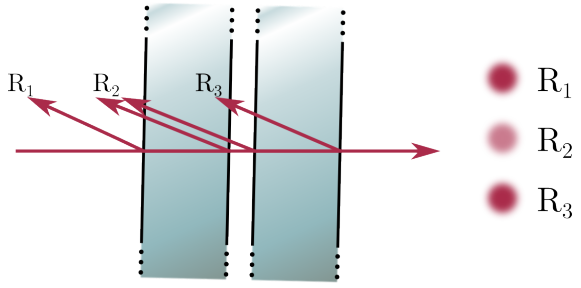

Figure A.1: Back reflection observed in the nanocell and the observed beam spots. Reflections from the front and back surfaces are well separated into spots R_1 and R_2, but the refleciton from both interior surfaces combine into spot R_3.

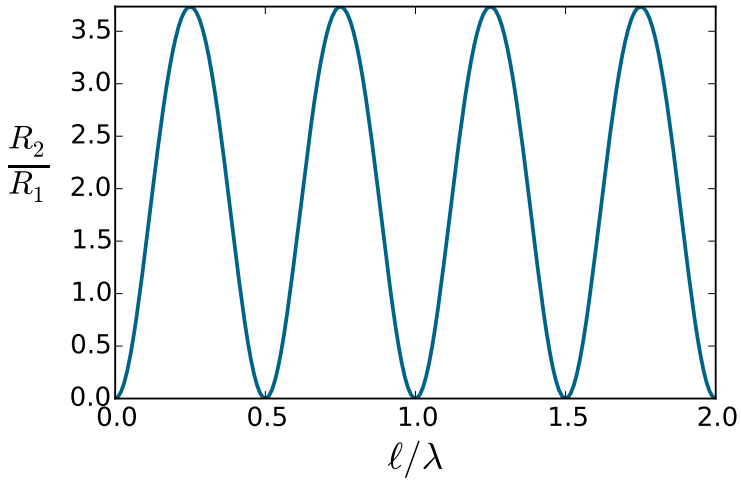

Figure A.2: Length dependence of intensity ratio of back reflection from the cell, plotted for quartz windows from Eq. A.0.1.

where ℓ is the length of the cell cavity and λ is the wavelength fo the interrogating beam. Fig. A.2 plots the length dependence of Eq. A.0.1 for a quartz cell window ($n = 1.45$) interrogated with a 780 nm laser. The maximum value of the ratio will vary depending on the refractive index of the cell windows. This method is routinely used to measure the length of nanocells. However, if the cell windows are not sufficiently thick, reflection R_1 can no longer be resolved from the other beam spots and alternate length measurement methods should be used, outlined in chapter 7.

Appendix B

Susceptibility relations

The time dependent response of the polarization of the medium excited by an electric field E at time t can be expressed as:

$$P(t) = \int_0^\infty R(\tau)E(t-\tau)d\tau, \tag{B.0.1}$$

Where $R(\tau)$ is the linear response function, describing the polarization response of the medium excited at time t after excitation at time $t-\tau$. The lower limit of integration is zero because the limits of causality apply; the system can have no response before an excitation is applied. Fourier transforming to find the frequency response yields:

$$\frac{1}{2\pi}\int_{-\infty}^{\infty} P(\omega)\mathrm{e}^{i\omega t}d\omega = \frac{1}{2\pi}\int_0^\infty\int_{-\infty}^{\infty} R(\tau)\mathrm{e}^{i\omega\tau}\mathrm{e}^{i\omega t}d\omega d\tau \tag{B.0.2}$$

Recalling from chapter 2 that the response of the medium to an electric field is given by $P(\omega) = \chi(\omega)E(\omega)$, an expression for $\chi(\omega)$ can be extracted:

$$\chi(\omega) = \int_0^\infty R(\tau)\mathrm{e}^{i\omega\tau}d\tau. \tag{B.0.3}$$

Since $R(\tau)$ is a real function, it can be seen from examination of B.0.3 that $\chi(-\omega) = \chi^*(\omega)$.